

University of Alberta

**Plume Dispersion Around a Building
from a Ground-level Source**

by



Fai Liu

A thesis submitted to the Faculty of Graduate Studies and Research in partial
fulfilment of the requirement for the degree of Master of Science

Department of Mechanical Engineering

Edmonton, Alberta

Fall, 1996



National Library
of Canada

Acquisitions and
Bibliographic Services Branch

395 Wellington Street
Ottawa, Ontario
K1A 0N4

Bibliothèque nationale
du Canada

Direction des acquisitions et
des services bibliographiques

395, rue Wellington
Ottawa (Ontario)
K1A 0N4

Your file *Votre référence*

Our file *Notre référence*

The author has granted an irrevocable non-exclusive licence allowing the National Library of Canada to reproduce, loan, distribute or sell copies of his/her thesis by any means and in any form or format, making this thesis available to interested persons.

L'auteur a accordé une licence irrévocable et non exclusive permettant à la Bibliothèque nationale du Canada de reproduire, prêter, distribuer ou vendre des copies de sa thèse de quelque manière et sous quelque forme que ce soit pour mettre des exemplaires de cette thèse à la disposition des personnes intéressées.

The author retains ownership of the copyright in his/her thesis. Neither the thesis nor substantial extracts from it may be printed or otherwise reproduced without his/her permission.

L'auteur conserve la propriété du droit d'auteur qui protège sa thèse. Ni la thèse ni des extraits substantiels de celle-ci ne doivent être imprimés ou autrement reproduits sans son autorisation.

ISBN 0-612-18290-8

Canada

University of Alberta

Library Release Form

Name of Author: *Fai LIU*

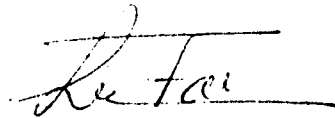
Title of Thesis: *Plume Dispersion Around a Building from a Ground-level Source*

Degree: *Master of Science*

Year this degree granted: *1996*

Permission is hereby granted to the University of Alberta Library to reproduce single copies of this thesis and to sell such copies for private, scholarly, or scientific research purposes only.

The author reserves all other publication and other rights in association with the copyright in the thesis, and except as hereinbefore provided, neither the thesis nor any substantial portion thereof may be printed or otherwise reproduced in any material form whatever without the author's prior written permission.



4567 Irmin Street

Burnaby, B.C., V5J 1Y1

Canada

Date: *May 2, 96*

University of Alberta

Faculty of Graduate Studies and Research

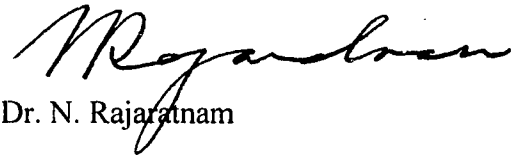
The undersigned certify that they have read, and recommended to the Faculty of Graduate Studies and Research for acceptance, a thesis entitled "*Plume Dispersion Around a Building from a Ground-level Source*" by **Fai Liu** in partial fulfilment of the requirement for the degree of **Master of Science**.



Dr. D.J. Wilson (Supervisor)



Dr. L.W. Kostiuk



Dr. N. Rajaratnam

Date: *April 25/96*

This work is dedicated to my wife and my daughter.

Abstract

The primary goal of the present study was to develop a model for plume dispersion on the upwind side and in the wake region of a building, and to compare it with experiments done in a water channel.

Several measurement techniques were used to investigate flow behaviour around two sizes of model buildings. A laser doppler velocimetry system was used to measure the flow characteristics, such as the mean flow velocity, turbulence intensity and Reynolds stress, with and without buildings present. The concentration measurements were done with laser fluorescence using dual light sheet and single laser beam linescan techniques and showed satisfactory agreement with model predictions.

The model incorporates the effects of the increase of the crosswind and vertical plume spreads due to the presence of a building. The crosswind and vertical spreads of a plume are assumed to be directly related to each other through a simple power function. The increase of the plume crosswind and vertical spreads produces the increased dilution of the plume in the vicinity of buildings. The new component of this single plume model is its ability to simulate the gradual and continuous increase in the plume crosswind spread upwind of a building.

Acknowledgements

Firstly I would like to thank my supervisor, Dr. D.J. Wilson for his guidance, insight and patience throughout the whole course of my study and the development of this thesis. His advices is greatly appreciated. Also I would like to thank Dr. L.W. Kostiuk for his very helpful suggestions on the preparation of the final version of this thesis. Financial support from Natural Sciences and Engineering Research Council, Alberta Occupational Health and Safety and the Canadian Gas Processors Association was also very appreciated.

My thanks are personally extended to Wayne Pittman whose help in the water channel laboratory was essential and brilliant. Thanks also go to Al Muir, Max Schubert, Albert Yuen and all the machine shop staffs for their excellent and expedient work. I am grateful to Trevor Hilderman for his assistance in collection of concentration measurements and editing of this thesis.

Finally, I wish to thank my wife for her constant help and love in many aspects during the study even though things took longer than expected, my parents and parents-in-law for their spiritual support and advice, and especially to my father-in-law for his great help during the early months following my baby girl's birth, my bay girl for bringing me joy and the new meaning of life, and all my friends, without their support and friendship I would have lost my sanity long time ago. Thanks guys!

Table of Contents

Chapter 1	Introduction	1
Chapter 2	Laboratory Simulation of Atmospheric Turbulence and Dispersion ..	5
2.1	Introduction	5
2.2	Water Channel	5
2.3	Development of the Required Boundary Layer	7
2.3.1	Design of the Roughness Base Plate	7
2.3.2	Generating the Required Boundary Layer	8
2.4	Velocity Measurement	10
2.4.1	Velocity and Turbulence Intensity Over the Rough Surface ..	14
2.4.2	Rough to Smooth Flow Transition on Building Base Plate ..	14
2.4.3	Model Buildings and Wind Direction Angles	15
2.4.4	Velocity and Turbulence in the Vicinity of a Building	15
2.5	Tracer Source	26
2.5.1	Ground Level Tracer Source	27
2.5.2	Behaviour of Disodium Fluorescein Tracer Dye	28
2.6	Linescan Concentration Measurements	29
2.6.1	Image Acquisition	30
2.6.2	Linescan Image Correction	31
2.6.3	Determination of Fluorescein Dye Mean Concentration	34
2.7	Full-Field Images Using PLIF	39
2.7.1	Image Collection	43
2.7.2	Image Corrections	44
Chapter 3	Plume Spread with Downwind Buildings	46
3.1	Introduction	46

3.2	Concentration Predictions Using Gaussian Plume Models	48
3.3	Extending the Gaussian Plume Model to the Current Studies	48
3.3.1	Developing the Plume Model Using Gaussian Plume Concept	49
3.3.2	Determining the Plume Spreads	53
3.3.3	Verifying the Gaussian Model Using Full-field Images	55
3.3.4	Normalizing the Plume Spread Difference ($\sigma_{y,w1} - \sigma_{y,w0}$)	56
3.3.5	Combining the Related Equations to Predict the Concentration Ratio	56
Chapter 4	Comparison of Plume Model to Experimental Data	72
4.1	Introduction	72
4.2	Plume Spread Correction	72
4.3	Determination of the Plume Maximum Concentration from Full-Field Images	73
4.4	Plumes at Yaw Angles of 0° and 90°	74
4.5	Plumes at Yaw Angles Between 0° and 90°	74
4.5.1	Using Projected Building Width to Calculate R	75
4.5.2	Linearly Interpolating R Using R_{90} and R_{θ}	75
4.6	Comparing the Predicted Concentrations to Linescan Measurements	75
4.7	Error in Interpreting the Measured Concentrations as Ground Level Concentrations	76
4.8	Empiricism in this Plume Model	77
4.9	Comparison to Other Models	78
4.9	Summary	80
Chapter 5	Summary and Conclusions	101
5.1	Summary	101
5.2	Conclusions	103

5.2	Recommendations for Future Studies	103
	References	109
Appendix A	Laser Light Attenuation Correction for Linescan	115
	I. Analysis	115
	II. Response of the Imaging Optics and Determination of $f(C_i)$, ϵ and β ,	119
	III. Numerical Correction for Dye Attenuation	121
	IV. Time-Dependent Dye Bleaching	122
Appendix B	Image Processing of Laser Sheet Lighting	136
	I. Generating Laser Sheets	136
	II. Viewing Plume Cross Sections	137
	III. Correcting the Raw Image	138
	a). Intensity and Concentration Conversion	138
	b). Intensity Correction	139
	c). Background Level Correction	141
	d). Corrections for Building Shadows and Light Sheet Irregularities	141

List of Figures

Figure 2.1:	Schematic diagram of the water channel	6
Figure 2.2:	New coordinate system definition	10
Figure 2.3:	Diagram of the test section and ground level source simulation	11
Figure 2.4:	Schematic diagram of the LDV system	12
Figure 2.5:	Evolution of the vertical velocity profiles in the boundary layer along stream ($x' = 1000, 2000, 2500, 3000\text{mm}$ downwind of the channel entrance)	16
Figure 2.6:	Evolution of the turbulence intensity profiles in the boundary layer along stream ($x' = 1000, 2000, 2500, 3000\text{mm}$ downwind of the channel entrance)	17
Figure 2.7:	Mean velocity, turbulence intensity, turbulence length scale and the Reynolds stress profiles for the fully developed channel flow at $x' = 3000\text{mm}$ downwind of the channel entrance	18
Figure 2.8:	Fitting measured velocity data using log-law for the fully developed channel flow at $x' = 3000\text{mm}$ downwind of the channel entrance	19
Figure 2.9:	Mean velocity profiles over the smooth plate and rough surface	20
Figure 2.10:	Semi-log plot of the mean velocity profiles over the smooth plate and	

rough surface	21
Figure 2.11: Mean velocity with and without building at $x' = 88$ mm upwind building <i>A</i> front face (building at $x = 170$ mm from the source location)	22
Figure 2.12: Turbulence intensity with and without building at $x' = 88$ mm upwind from building <i>A</i> front face (building at $x = 170$ mm from the source location)	23
Figure 2.13: Mean velocity upwind and downwind of building <i>A</i> (located at $x = 170$ mm from the source) front face for data measured at $x = -20, -30, 65$ and 415 mm downwind of the source (with the no building case as reference)	24
Figure 2.14: Turbulence intensity upwind and downwind of building <i>A</i> (located at $x = 170$ mm from the source) front face for data measured at $x = -20, -30, 65$ and 415 mm downwind of the source (with the no building case as reference)	25
Figure 2.15: Calibration of the rotameter used in the current experiment for tracer dye flow control	27
Figure 2.16: Schematic diagram of dye source	27
Figure 2.17: Schematic diagram of the single laser beam system	30
Figure 2.18: Schematic diagram of image acquisition and processing system	31
Figure 2.19: Non-linear response of the camera to light intensity input (proportional to inverse square of lens f -stop setting) when shutter speed = $1/250$ sec	

	and dye concentration $C = 6.25 \mu\text{mol/litre}$ were used	33
Figure 2.20:	Illustration of linescan intensity measurement for a calibration bottle	36
Figure 2.21:	Non-linear response of the image system at apertures set at $f_{\text{stop}} = 1.4$ and $f_{\text{stop}} = 5.6$ (camera shutter speed: 1/250 sec, and Kodak No.21 gelatin filter was used)	37
Figure 2.22:	Adjustment of the calibration curve according to laser light intensity day-to-day variations	38
Figure 2.23:	Attenuation correction test against the known concentration bottles	40
Figure 2.24:	Samples of corrected and uncorrected (linescan) plume concentration profiles with and without a building present (building <i>A</i> at yaw angle 90° and dimensions 100mm wide \times 50mm height \times 40mm long)	41
Figure 2.25:	Schematic diagram of visualizing the building in two planes	42
Figure 2.26:	Examples of selected full-field concentration images filtered with 9×9 spatial filter for buildings located at 270mm from source. Each dilution contour has a factor of 1.50 reduction (building <i>A</i> : 100mm wide \times 50mm height \times 40mm long; building <i>B</i> : 100mm wide \times 100mm height \times 40mm long)	45
Figure 3 1:	Schematic diagram showing the crosswind spread of a plume	51
Figure 3.2:	Comparison of using different building length scales on building <i>A</i> at	

	0° yaw angle (building dimensions: 100mm wide × 50mm height × 40mm long)	59
Figure 3.3:	Comparison of using different building length scales on building <i>B</i> at 90° yaw angle (building dimensions: 100mm wide × 50mm height × 40mm long)	60
Figure 3.4:	Plume concentration image and its crosswind spread obtained from experimental data	61
Figure 3.5:	Two selected concentration images from present experiment for buildings at 270 mm from source and 0° yaw angle (dimensions of buildings: <i>A</i> , 100mm wide × 50mm height × 40mm long; <i>B</i> , 100mm wide × 100mm height × 40mm long)	62
Figure 3.6:	Plume crosswind spreads, $\sigma_{y,wi}$ and $\alpha_{y,wo}$ for building <i>A</i> at $x = 170$ mm from source with yaw angle 0° and 30° (building <i>A</i> dimensions: 100mm wide × 50mm height × 40mm long)	63
Figure 3.7:	Plume crosswind spreads, $\sigma_{y,wi}$ and $\alpha_{y,wo}$ for building <i>A</i> at $x = 170$ mm from source with yaw angle 60° and 90° (building <i>A</i> dimensions: 100mm wide × 50mm height × 40mm long)	64
Figure 3.8:	Plume crosswind spreads, $\sigma_{y,wi}$ and $\alpha_{y,wo}$ for building <i>B</i> at $x = 270$ mm from source with yaw angle 0° and 30° (building <i>B</i> dimensions: 100mm wide × 100mm height × 40mm long)	65
Figure 3.9:	Plume crosswind spreads, $\sigma_{y,wi}$ and $\alpha_{y,wo}$ for building <i>B</i> at $x = 270$ mm from source with yaw angle 60° and 90° (building <i>B</i> dimensions: 100mm wide × 100mm height × 40mm long)	66

Figure 3.10:	Illustration showing the finding of $\sigma_{z,m}$ at specified x location downwind from source (x - z , vertical sheet and laser beam both at $x = 170$ mm)	67
Figure 3.11:	Illustration showing the finding of $\sigma_{z,m}$ obtained from both full-field and linescan measurement at specified $x = 230, 330, 430$ and 530 mm downwind from source	68
Figure 3.12:	Verification of Gaussian plume model using experimentally determined crosswind, vertical plume spreads and the windspeed at the laser sheet height	69
Figure 3.13:	Applying $\phi(x^*/R)$ function to building A at $0^\circ, 45^\circ$ and 90° yaw angle (building dimensions: 100 mm wide \times 50 mm height \times 40 mm long)	70
Figure 3.14:	Applying $\phi(x^*/R)$ function to building B at $0^\circ, 45^\circ$ and 90° yaw angle (building dimensions: 100 mm wide \times 100 mm height \times 40 mm long)	71
Figure 4.1:	Building projected width	74
Figure 4.2:	Trace of the plume local maximum concentration when no building is present	81
Figure 4.3:	Trace of the plume local maximum concentration for building A at $x = 170$ mm from the source with yaw angle at 0° and 30° dimensions of building A : 100 mm wide \times 50 mm height \times 40 mm long)	82
Figure 4.4:	Trace of the plume local maximum concentration for building A at $x =$	

	170mm from the source with yaw angle at 60° and 90° dimensions of building <i>A</i> : 100mm wide × 50mm height × 40mm long)	83
Figure 4.5:	Trace of the plume local maximum concentration for building <i>B</i> at <i>x</i> = 270mm from the source with yaw angle at 0° and 30° dimensions of building <i>B</i> : 100mm wide × 100mm height × 40mm long)	84
Figure 4.6:	Trace of the plume local maximum concentration for building <i>B</i> at <i>x</i> = 270mm from the source with yaw angle at 60° and 90° dimensions of building <i>B</i> : 100mm wide × 100mm height × 40mm long)	85
Figure 4.7:	Experimental and predicted concentration ratio (C_{wf}/C_{wo}) for short building located at 170mm from source and orientated at 0° and 90°	86
Figure 4.8:	Experimental and predicted concentration ratio (C_{wf}/C_{wo}) for short building located at 270mm from source and orientated at 0° and 90°	87
Figure 4.9:	Experimental and predicted concentration ratio (C_{wf}/C_{wo}) for short building located at 370mm from source and orientated at 0° and 90°	88
Figure 4.10:	Experimental and predicted concentration ratio (C_{wf}/C_{wo}) for tall building located at 170mm from source and orientated at 0° and 90°	89
Figure 4.11:	Experimental and predicted concentration ratio (C_{wf}/C_{wo}) for tall building located at 270mm from source and orientated at 0° and 90°	90
Figure 4.12:	Experimental and predicted concentration ratio (C_{wf}/C_{wo}) for tall building	

	located at 370mm from source and orientated at 0° and 90°	91
Figure 4.13:	Experimental and predicted concentration ratio (C_w/C_{w0}) for short building located at 170mm from source, orientated at 30° and 60° and R calculated using projected width	92
Figure 4.14:	Experimental and predicted concentration ratio (C_w/C_{w0}) for short building located at 270mm from source, orientated at 30° and 60° and R calculated using projected width	93
Figure 4.15:	Experimental and predicted concentration ratio (C_w/C_{w0}) for short building located at 370mm from source, orientated at 30° and 60° and R calculated using projected width	94
Figure 4.16:	Experimental and predicted concentration ratio (C_w/C_{w0}) for tall building located at 170mm from source, orientated at 30° and 60° and R calculated using projected width	95
Figure 4.17:	Experimental and predicted concentration ratio (C_w/C_{w0}) for tall building located at 270mm from source, orientated at 30° and 60° and R calculated using projected width	96
Figure 4.18:	Experimental and predicted concentration ratio (C_w/C_{w0}) for tall building located at 370mm from source, orientated at 30° and 60° and R calculated using projected width	97
Figure 4.19:	Experimental and predicted concentration ratio (C_w/C_{w0}) when using different building length scale (R) for short building at 270mm from source	98

Figure 4.20: Effects on predicted concentration ratio (C_w/C_w) when using different building length scale (R) for tall building 270mm from source 99

Figure 4.21: Comparison of data from linescan, theory and full-field image at the same x location (building at 270mm from source, laser beam at 60mm downwind of the building) 100

Figure 5.1: Plume concentration contour from full-field image and concentration profiles from linescan data for building A at yaw angle 0° and 30° (100mm wide \times 50mm height \times 40mm long). (a) and (b) building location at $x = 270$ mm from source; (c) and (d) laser position at $x = 330$ mm, $z = 5$ mm 105

Figure 5.2: Plume concentration contour from full-field image and concentration profiles from linescan data for building A at yaw angle 60° and 90° (100mm wide \times 50mm height \times 40mm long). (a) and (b) building location at $x = 270$ mm from source; (c) and (d) laser position at $x = 330$ mm, $z = 5$ mm 106

Figure 5.3: Plume concentration contour from full-field image and concentration profiles from linescan data for building B at yaw angle 0° and 60° (100mm wide \times 100mm height \times 40mm long). (a) and (b) building location at $x = 270$ mm from source; (c) and (d) laser position at $x = 330$ mm, $z = 5$ mm 107

Figure 5.4: Plume concentration contour from full-field image and concentration profiles from linescan data for building B at yaw angle 60° and 60° (100mm wide \times 100mm height \times 40mm long). (a) and (b) building location at $x = 270$ mm from source; (c) and (d) laser position at $x = 330$ mm, $z = 5$ mm 108

Figure A-1:	Determination of extinction coefficient ϵ with varying concentration when $f_{stop} = 1.4$, shutter speed = 1/250 sec and test concentration at $C = 6.25, 4.38, 3.13$ and $2.19 \mu\text{mol/litre}$	125
Figure A-2:	Determination of extinction coefficient ϵ with varying concentration when $f_{stop} = 1.4$, shutter speed = 1/250 sec and test concentration at $C = 1.56, 1.09, 0.78$ and $0.55 \mu\text{mol/litre}$	126
Figure A-3:	Determination of extinction coefficient ϵ with varying concentration when $f_{stop} = 1.4$, shutter speed = 1/250 sec and test concentration at $C = 0.39, 0.27, 0.19$ and $0.14 \mu\text{mol/litre}$	127
Figure A-4:	Determination of extinction coefficient ϵ with varying concentration when $f_{stop} = 5.6$, shutter speed = 1/250 sec and test concentration at $C = 35.0, 25.0, 17.5$ and $12.5 \mu\text{mol/litre}$	128
Figure A-5:	Determination of extinction coefficient ϵ with varying concentration when $f_{stop} = 5.6$, shutter speed = 1/250 sec and test concentration at $C = 8.75, 6.25, 4.38$ and $3.13 \mu\text{mol/litre}$	129
Figure A-6:	Determination of extinction coefficient ϵ with varying concentration when $f_{stop} = 5.6$, shutter speed = 1/250 sec and test concentration at $C = 2.19, 1.56, 1.09$ and $0.78 \mu\text{mol/litre}$	130
Figure A-7:	Image system response to dye solutions at camera f_{stop} set at 1.4 or 5.6 when other camera settings were: shutter speed = 1/250 sec, camera gain = 6, camera white balance = 3200 and filter used = Kodak Wratten No.21 gelatin filter	131
Figure A-8:	Pixel-by-pixel dark response of the image system along a single line (100	

Figure A-8:	Pixel-by-pixel dark response of the image system along a single line (100 frame average)	132
Figure A-9:	Illustration of measured light intensity before and after attenuation correction	133
Figure A-10:	Laser light bleaching test on fluorescent dye solution with concentration of 5.0 $\mu\text{mol/litre}$	134
Figure A-11:	Illustration of dye particle path across the laser sheet	135
Figure B-1:	Laser and splitting optics (used in PLIF)	143
Figure B-2:	Laser beam expanding optics and assembly and sheet optics used to produce a light sheet	143
Figure B-3:	Schematic diagram of dual laser sheet concentration calibration ..	144
Figure B-4:	Calibration curve for the dual laser light sheet with the camera settings as: $f_{stop} = 2$, speed = 1/60 sec and laser power = 3.0 W	145
Figure B-5:	Effect of using different size lowpass filter on a selected image ...	146
Figure B-6:	Examples of selected images corrected by using 9 \times 9 lowpass filter (Building location: $x = 270\text{mm}$ from the source. Building size: building A 100mm wide \times 100mm height \times 40mm long; building B:100mm wide \times 100mm height \times 40mm long)	147

List of Tables

Table 4.1	Error from Interpreting Measured Concentration at $z = 5\text{mm}$ as Ground Level Concentration	77
Table 4.2	Comparing the Predicted Concentration Ratio (C_w/C_{w0}) at the Building Rear Face for Building <i>A</i> at Yaw angle $\theta = 0^\circ$	78
Table 4.3	Comparing the Predicted Concentration Ratio (C_w/C_{w0}) at the Building Rear Face for Building <i>B</i> at Yaw angle $\theta = 0^\circ$	78
Table 4.4	Comparing the Predicted Concentration Ratio (C_w/C_{w0}) at the Building Rear Face for Building <i>A</i> at Yaw angle $\theta = 90^\circ$	79
Table 4.5	Comparing the Predicted Concentration Ratio (C_w/C_{w0}) at the Building Rear Face for Building <i>B</i> at Yaw angle $\theta = 90^\circ$	79

Symbols and Nomenclature

A	model building with dimensions of 100mm wide×50mm high×40mm long
A_l	an empirical constant used to correct the laser sheet edge effect, see Equation (C.7)
A_l	cross section area of the laser beam
A_p	building streamwise projected area
a	empirical constant used to relate the plume vertical spread with and without a building present, see Equation (3.8)
B	model building with dimensions of 100mm wide×100mm high×40mm long
b	an empirical constant used to relate the plume velocity to plume spreads with and without a building present, see Equation (3.12)
C	plume concentration ($\mu\text{mol/litre}$)
$C_{cor,i}$	corrected concentration of i^{th} pixel on a plume video image
C_i	i^{th} pixel concentration ($\mu\text{mol/litre}$)
C_0	plume ground-level concentration ($\mu\text{mol/litre}$)
C_{ref}	concentration at a reference location of laser sheets ($\mu\text{mol/litre}$)
C_s	source concentration ($\mu\text{mol/litre}$)
C_{sheet}	sheet concentration ($\mu\text{mol/litre}$)
C_w	plume concentration with building present ($\mu\text{mol/litre}$)
C_{wo}	plume concentration without building present ($\mu\text{mol/litre}$)
C_{0mm}	plume concentration at 0mm above ground ($\mu\text{mol/litre}$)
C_{5mm}	plume concentration at 5mm above ground ($\mu\text{mol/litre}$)
D	building depth (mm)
d_0	log-law displacement thickness (mm)
D_s	separation distance between the nearest neighbouring roughness elements (mm)
E_{photon}	energy of a photon (J/photon)

$f()$	function of
f_{stop}	camera aperture setting
g	inverse function of f
F_Q	quantum yield fraction of fluorescent dye (4×10^{-6} , Ippen <i>et al</i> (1971))
H	model building height (mm)
h	roughness element height (mm)
h_s	source height from ground (mm)
I	pixel light intensity (digital counts)
I	index number for an array of pixels
ΔI	finite difference between two adjacent pixels (digital counts)
$I_{\text{cam},0}$	camera measured original laser excitation intensity (digital counts)
$I_{\text{cam},\text{cen}}$	Camera measured fluorescent intensity at the centre of a calibration bottle
$I_{\text{cam},i}$	camera measured i^{th} pixel florescent intensity (digital counts)
I_f	local fluorescence (digital counts)
$I_{\text{in},0}$	original laser excitation intensity
$I_{\text{in},j}$	excitation laser intensity at j^{th} pixel
$I_{\text{in},\text{ref}}$	laser excitation intensity from laser sheets at a reference location
$I_{j,\text{cor}}$	j^{th} corrected pixel intensity from a video full-field image (digital counts)
$I_{j,\text{out}}$	j^{th} pixel intensity form a video full-field image (digital counts)
$I_{j,\text{sheet}}$	j^{th} pixel intensity from a laser sheet video image (digital counts)
I_{ref}	measured fluorescent light intensity measured at a reference location of laser sheets (digital counts)
$I_{\text{ref},\text{sheet}}$	measured fluorescent light intensity measured at a reference location from a sheet video image (digital counts)
i_u	mean flow turbulence intensity
j	index number for an array of pixels
k	empirical constant used in Gifford (1960) model and $0.5 < k < 2.0$
L	larger dimension of a building front face (mm)
LDV	Laser Doppler Velocimetry
ℓ	crosswind diameter of a roughness element (mm)

N_{av}	Avogadro number (6.023×10^{23} molecules/mole)
P	laser power output from the Laser Doppler Velocimeter (mW)
PLIF	Planar Laser Induced Fluorescence
Q	mass flow rate of the source (g/s)
R	building length scale (mm), defined as $R = L^{1/3} S^{2/3}$ where L is the larger of H or W , and S is the smaller of the two
R_{90}	building length scale at yaw angle 90°
R_0	building length scale at yaw angle 0°
S	smaller dimension of a building front face (mm)
t	measured elapsed time (second)
t_{absorb}	fluorescent dye bleaching time constant (second), see Equation (A.20)
U	flow mean velocity (cm/s)
U_1	flow mean velocity (cm/s) at along-stream location x_1 , see Equation (3.10)
U_2	flow mean velocity (cm/s) at along-stream location x_2 , see Equation (3.10)
U_c	flow convective velocity (cm/s)
U_w	flow mean velocity with a building present (cm/s)
U_{ww}	flow mean velocity without a building present (cm/s)
u^*	turbulence velocity (cm/s)
W	model building width (mm)
x	streamwise coordinate starting at the source location, defined in Figure 2.2
x'	streamwise coordinate starting at the channel test section entrance, defined in Figure 2.2
x''	streamwise coordinate starting at the building front face, defined in Figure 2.2
Δy	finite difference distance between two adjacent pixels in crosswind direction (mm)
y	crosswind coordinate starting at the source location, defined in Figure 2.2
y_c	plume centre of first moment of concentration in crosswind direction, see Equation (3.15)
y'	crosswind coordinate starting at the channel test section entrance, defined in Figure 2.2

y'	crosswind coordinate starting at the building front face, defined in Figure 2.2
Z_o	roughness length from an analytical solution (mm), see Equation (2.2)
$Z_{o,exp}$	roughness length obtained from experiment (mm)
z	vertical coordinate starting at the source location, defined in Figure 2.2
z'	vertical coordinate starting at the channel test section entrance, defined in Figure 2.2
z^+	vertical coordinate starting at the building front face, defined in Figure 2.2

Greek Symbols

α	empirical constant to account for the camera non-linearity, see Equation (A.11)
β_i	clear water response of the video image system at i^{th} pixel on a video image
θ	building yaw angle ($^\circ$)
κ	von Karman's constant (0.4)
λ	roughness element area concentration factor, see Equation (2.1)
ϵ	laser extinction coefficient [$\text{mm} \cdot (\text{mol}/\text{litre})^{-1}$]
σ	molecular cross section of dye particles (cm^2), see Equation (A.20)
σ_y	plume crosswind spread (mm)
σ_y'	adjusted plume crosswind spread downwind a building using by other models (mm)
$\sigma_{y,wi}$	plume crosswind spread with a building present (mm)
$\sigma_{y,wo}$	plume crosswind spread without a building present (mm), see Equation (3.17)
$\sigma_{y,wo,\theta}$	plume crosswind spread at $x = 0\text{mm}$ without a building present (mm), see Equation (3.17)
σ_z	plume vertical spread (mm)
σ_z'	adjusted plume vertical spread downwind a building using by other models

(mm)

- $\sigma_{z,w}$ plume vertical spread with a building present (mm)
- $\sigma_{z,w,0}$ plume vertical spread without a building present (mm), see Equation (3.20)
- $\sigma_{z,w,0}$ plume vertical spread at $x = 0$ m without a building present (mm), see Equation (3.20)
- π constant with a value of 3.141592654
- τ experimentally obtained fluorescent dye bleaching constant (second), see Equation (A.22)
- Φ photon flux of the laser beam (photons/mm²/s)
- ϕ function relates the plume crosswind spread with and without a building present, see Equation (3.22)

Chapter 1

Introduction and Literature Review

1.1 Review of Models

The first estimate of building effects on plume dispersion was made by Gifford (1960) who proposed a model that increased plume dilution downwind of a building by adding an additional vertical and crosswind plume spread to the standard Gaussian model for predicting the centerline ground level concentration. Gifford (1960) suggested that this added plume spread should be directly proportional to the building projected frontal area. Since then, several variations of this model have been published. Turner (1969) and Baker (1982) proposed virtual source models; Ferea and Cagnettis (1980) and Huber and Snyder (1976,1982) used different values for the vertical and crosswind components of the added sprcaus. None of these models accounted for the gradual change of the plume spread that begins several building heights upstream. Instead, the building was assumed to produce an abrupt increase in plume spread (and decrease in concentration) at its downwind wall. The present study is the first one to quantitatively study this phenomenon and develop a model which incorporates and predicts the plume dilutions upwind of a building.

Other than the Gaussian models to deal with the building effluent on plume dispersion, turbulence diffusion and self-preserving wake theory have also been used to cope with the effects of buildings. Hunt (1971*b*) developed a model for the laminar velocity wake behind a two-dimensional obstacle in a laminar boundary layer. Based on Hunt's (1971*b*) theory, Counihan, Hunt and Jackson (1974) proposed their model which was able to deal with the velocity wakes behind two-dimensional surface mounted obstacles in turbulent a boundary layer.

Starting from the diffusion equation, Hunt, Puttock and Snyder (1979) derived equations

for predicting plume concentrations around a three-dimensional hill in stratified and neutral flows. Combining constant eddy diffusivity with the advective diffusion equation, Puttock and Hunt (1979) proposed an eddy diffusivity model for predicting plume concentrations from a source near an obstacle. Diffusion models have more complicated formulations for plume concentration and have not showed great advantages over the widely accepted Gaussian plume models.

The building wake recirculation region is also of great interest for many practical applications such as the design of the building ventilation intakes. Vincent (1977), (1978) proposed a residence time model to characterize wake diffusion by the time constant decay rate of the spatially averaged wake concentration. Robins and Fackrell (1980) related Vincent's residence time model to estimate the average concentration by modelling the recirculation zone surface area. Wilson and Britter (1982), suggested a design equation that treats the concentration in wake recirculation as a constant for wake cavity concentration dominated by flow recirculation and self-entrainment. Wilson and Britter's proposal is supported by many other studies such as Drivas and Shair (1974), Halitsky (1977), Robins and Castro (1977) and Thompson (1993).

One recent investigation of building influence on plume dispersion was conducted by Genikhovich and Snyder (1994). They proposed a new mathematical model that incorporates a non-Gaussian concept into a currently used Gaussian model by superposing the circulating and non-circulating flow fields around a building through a probability function. This new model was tested against tracer gas data measured fifteen building heights downwind from the building and field measurements from Bowers and Anderson (1981), Ogawa and *et al* (1983), Berlyand and *et al* (1987b) and Genikhovich and *et al* (1987). This new Genikhovich and Snyder model showed better performance both in the near and far wake region than the older models. However, the new model usually over-predicted ground level concentrations without a building present.

At present, the modified Gaussian plume model, proposed by Huber and Snyder (1982) from their wind tunnel studies, is used by the U.S. Environmental Protection Agency to predict the plume concentrations within the near wake recirculation region, and on building roofs and walls. But this model has deficiencies caused by discontinuities in plume spread based on the abrupt transition between the recirculation, near wake and the far wake regions, and on the ratio of stack or source height to the building height.

1.2 Review of Experimental Techniques

Different techniques had been used to investigate the plume dispersion process under the influence of an obstacle. Tracer gases in wind tunnel simulations have been used by several investigators; helium and propane mixtures by Robins and Castro (1977), helium by Wilson and Netterville (1978) and Li and Meroney (1983), sulphur hexafluoride by Ogawa and Oikawa (1982), air-methane mixtures by Huber and Snyder (1982) and ethane by Huber (1989,1991).

Optical means of continuously recording the plume images illuminated by various types of light sources have also been used; Poreh and Cermak (1991) used infra red light on a carbon dioxide gas plume, Lee *et al* (1991) used banks of fluorescent lamps to illuminate vaporized paraffin oil smoke, Huber *et al* (1991) used strong floodlights on an oil-fog smoke, and Martinuzzi and Tropea (1993) used a laser to illuminate fluorescent dye.

1.3 Overview of this Study

The present study was undertaken to develop a plume model for plume impingement on a building from a ground level source. The goal was to make accurate estimation of the ratio of plume concentration with and without a building present for a wide range of wind direction angles for different building sizes. A Gaussian plume model was used as the stepping-stone for deriving the theoretical model used in this thesis. Both theoretical and experimental means were used to achieve the goal of developing a simple model

which accounts for building effects for a plume from a ground level source.

To correctly simulate neutral atmospheric flow in the water channel, a new rough surface was designed and constructed. Flow characteristics such as mean velocity, turbulence intensity, integral length scale and Reynolds stress were measured using Laser Doppler Velocimetry. Planar Laser Induced Fluorescence was used for full-field plume visualization and image collection. From these full-field images, plume mean concentrations, vertical and crosswind spread were calculated. In conjunction a single beam linescan method was used to illuminate the plume at different along-stream and vertical positions for cross plume concentration measurements.

The experimental results obtained by using both dual laser sheet and linescan methods to determine the plume spreads and the concentration ratio between with and without a building present will be presented. By comparing the theoretical prediction of the plume concentration to the experimental data, the Gaussian plume model developed in this thesis will show good agreement with measurements.

Chapter 2

Laboratory Simulation of Atmospheric Turbulence and Dispersion

2.1 Introduction

Experimental measurements were used to determine the influence of buildings on the concentration distribution of a plume released upstream at ground level. Buildings with different dimensions, placed at varying locations downwind from the source and at different yaw angles to flow, were investigated.

- Laser Doppler Velocimetry (LDV) was used to investigate the velocity and turbulence characteristics of the boundary layer of the channel flow with and without a building in place.
- Full-field flow visualization for flow around the model buildings was performed by illuminating fluorescein dye tracer solution released from a ground level source using the Planar Laser Induced Fluorescence (PLIF) technique.
- Linescan concentration measurements were made by shining a single laser light beam through the plume to produce laser induced fluorescence in the tracer dye solution.

Each of these techniques provided information needed to develop a modified Gaussian plume model that includes the upwind and downwind effects of buildings.

2.2 Water Channel

The current study was conducted in the atmospheric simulation water channel of the Mechanical Engineering Department at the University of Alberta. The test section of the water channel was 5000mm long × 680mm wide × 476mm deep and consisted of three sides of clear glass with an open top surface. A schematic diagram of the channel is

shown in Figure 2.1. The two stainless steel tanks at each end of the test section together hold about 5000 litres of water. Two 5 h.p. water pumps were used to circulate the required flow from tank to tank through a 152mm I.D. return pipe situated underneath the test section. The water flow rate at the test section was monitored with a manometer on an orifice mounted inside the return pipe. The 350mm water depth at the test section used for the current studies was controlled by adjusting the angle of the weir gate located at the downstream end of the test section.

Before entering the test section, water flowed through two flow straighteners shown in Figure 2.1 to remove swirl in the flow. The two screens placed across the supply tank were used to damp out turbulence. The flow straightener at the beginning of the test section had dimensions of 680mm wide \times 476mm high \times 100mm thick and was constructed using stainless steel strips.

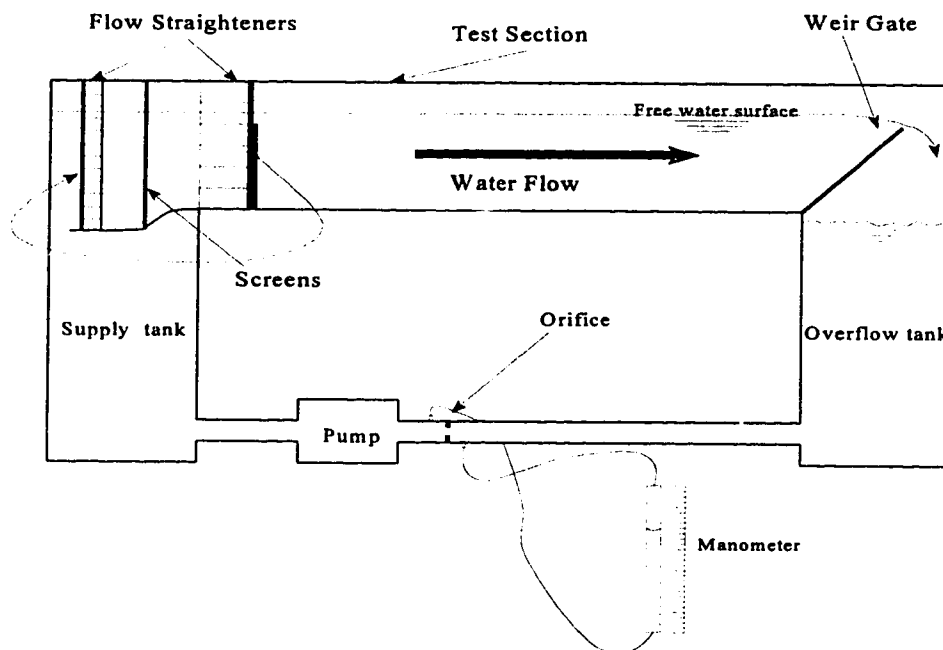


Figure 2.1 Schematic diagram of the water channel

2.3 Development of the Required Boundary Layer

Correct simulation of the mean velocity, turbulence intensity and scale in the turbulent boundary layer are the essential requirements for atmospheric simulation.

2.3.1 Design of the Roughness Base Plate

In order to produce the correct boundary layer simulation, roughness base plates were constructed to cover the bottom of the test section. With an arbitrarily chosen scale factor of 500:1 and a full scale roughness length Z_o in the range 0.5 ~ 1.0m, the simulated Z_o in the water channel should be in the range of 1 ~ 2mm.

Raupach *et al* (1980) suggested that the laboratory Z_o is a function of the chosen height (h), breadth (D_s), separation distance (ℓ) and area concentration factor (λ) of the roughness elements. The factor λ is the ratio between the frontal area of a roughness element and its surrounding plan view floor area. Under the assumption that the flow is fully developed, Raupach *et al* proposed an analytical equation to relate Z_o , ℓ and λ :

$$\frac{Z_o}{h} = \exp[-\kappa f(\lambda)] \quad (2.1)$$

where: $\kappa = 0.4$, von Karman's constant, and $f(\lambda) =$ function of λ .

Equation (2.1) was further simplified by Raupach *et al* (1980) in the region where $10^{-3} < \lambda < 1.2 \times 10^{-1}$ to,

$$\frac{Z_o}{h} \cong \lambda \quad (2.2)$$

where, from geometrical considerations the area concentration factor, λ , of the roughness elements is:

$$\lambda = \frac{h D_s}{\ell^2} \quad (2.3)$$

where,

λ = roughness area concentration;

h = height of one roughness element (mm);

D_s = crosswind width (diameter) of the roughness element (mm);

ℓ = separation distance from the nearest neighbouring roughness element (mm).

This relation implicitly assumes that the flow separates from the leading edges of the roughness elements so that their length in the flow direction is not relevant.

The desired full scale roughness was $Z_o \cong 0.7\text{m}$, or $Z_o \cong 1.40\text{ mm}$ in 500:1 scale. This corresponds to a built up urban area or industrial plant site. Based on the calculations using Equations (2.2) and (2.3), h , D_s and ℓ were chosen as 12.0mm, 1.6mm and 13.0mm respectively. To create this surface roughness a set of interlocking polycarbonate base plates were fabricated, each with dimensions of 800mm long \times 680mm wide \times 15mm thick. An array of holes with $D_s = 1.6\text{mm}$ and $\ell = 13.0\text{mm}$ was drilled in the plate. Then, the roughness elements, about 20,000 nylon pins, were press fit one by one into the drilled holes on the base plates using specially made tools.

2.3.2 Generating the Required Boundary Layer

If allowed to develop naturally, flow entering the water channel test section would eventually form a fully developed boundary layer with a logarithmic mean velocity profile extending up to the free surface. But, the 5000mm long test section of the water channel is not sufficient for such a flow to develop naturally. Therefore, the length required to create a fully developed boundary layer had to be reduced by artificial means. Several different methods were tried to develop the optimal flow required for the current studies. They were:

1. Several layers of wire screen were laminated to produce more blockage at the bottom than at the top. It was found that the screen was not open enough at the medium height region to further accelerate the flow in the upper portion of the boundary layer. Both vertical and horizontal velocity profiles had unacceptable irregularities in mean and turbulence profiles.
2. Rubber and foam plugs were inserted into selected channels in the 100mm thick flow straightener placed at the inlet of the test section so that the water flow entering the test section encountered more resistance near the bottom. However, the same problems occurred as mentioned in trial 1.
3. A triangular flow straightener was made to have a height of 508mm and flow channels 120mm long at its bottom, with their length decreasing to zero at the top. This time, the results were much more encouraging even though the triangular flow straightener was still not good enough to produce the required velocity profiles. More blockage at bottom region of the water flow was needed.
4. The newly made triangular flow straightener was tilted about 5° towards the oncoming flow. The vertical profile obtained at the channel centerline at 1300mm downwind of the channel inlet was satisfactory, but the horizontal/cross stream velocity profile measured at the same x' location (see Figure 2.2 for definition of the coordinate systems) was not uniform.
5. A flat screen, which had the same dimensions as the water channel cross-section, with arrays of $18\text{mm} \times 18\text{mm}$ diamond shaped holes, was put into the channel vertically 100mm downstream of the new flow straightener. The flat screen did help to smooth out the irregularities in the horizontal velocity profile, but also reduced the turbulence in the flow too much.

6. The flat blockage screen with diamond-shaped holes used in trial 5 was modified to produce variable blockage. Cutouts were used to create decreasing blockage with height. After many trials, the final combination of modified flat screen and the trip wall, necessary to generate the expected boundary layer flow in the test section was found, see Figure 2.3. The modified flat screen, attached to the downstream side of the flow straightener, was 340mm high and 674 mm wide with higher blockage at the bottom, less blockage at the medium height region and no blockage at the top. The trip wall, which was 40mm high and placed 300mm downwind of the modified screen, created the flow separation, momentum deficit and turbulence necessary for developing the log-mean boundary layer

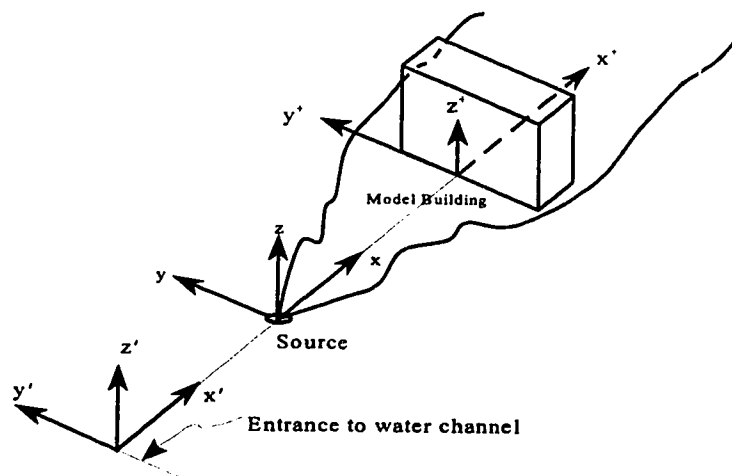
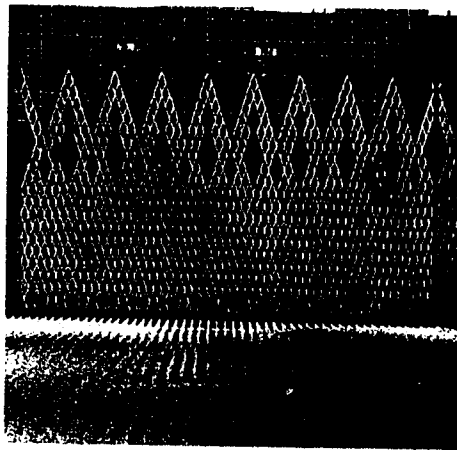


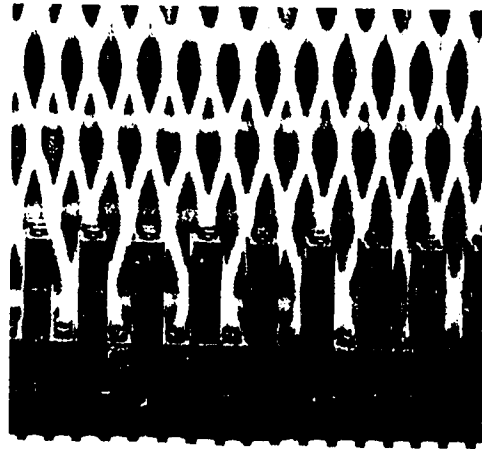
Figure 2.2 New coordinate system definition

2.4 Velocity Measurement

Determining the atmospheric wind that had been accurately simulated required measurements of mean flow velocity, turbulence and Reynolds stress profiles at various locations in the test section in the cross stream, vertical and along stream directions. It is also important to know how the mean velocity and the turbulence fields are disturbed by



Modified flat screen (front view)



Trip wall (front view)

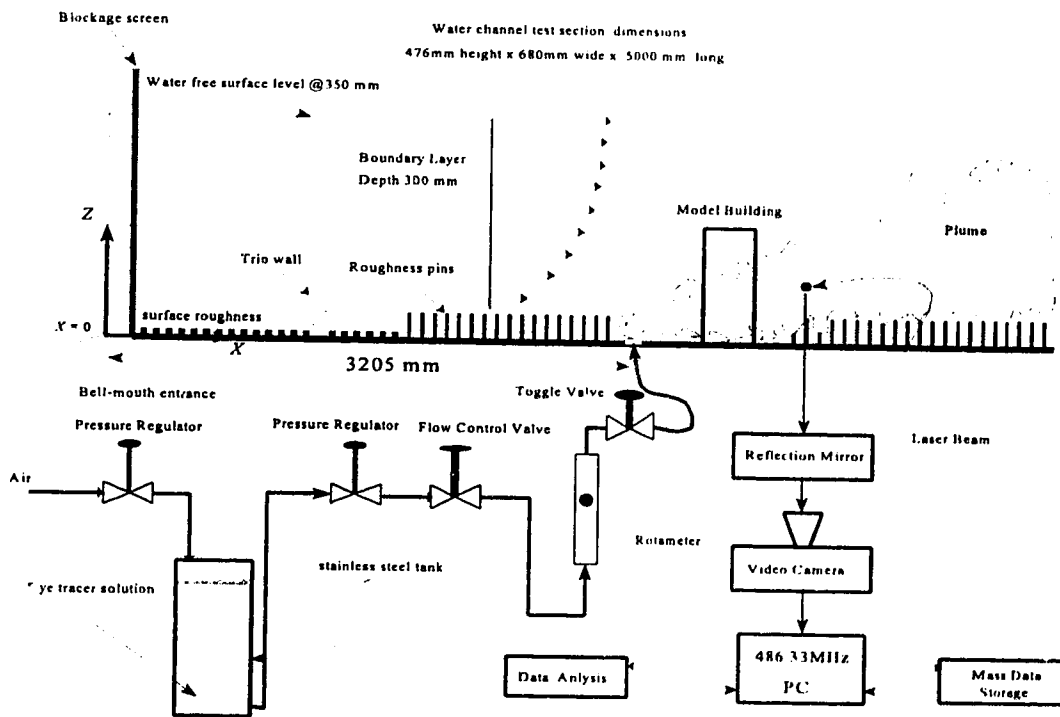


Figure 2.3 Diagram of the test section and ground-level source simulation

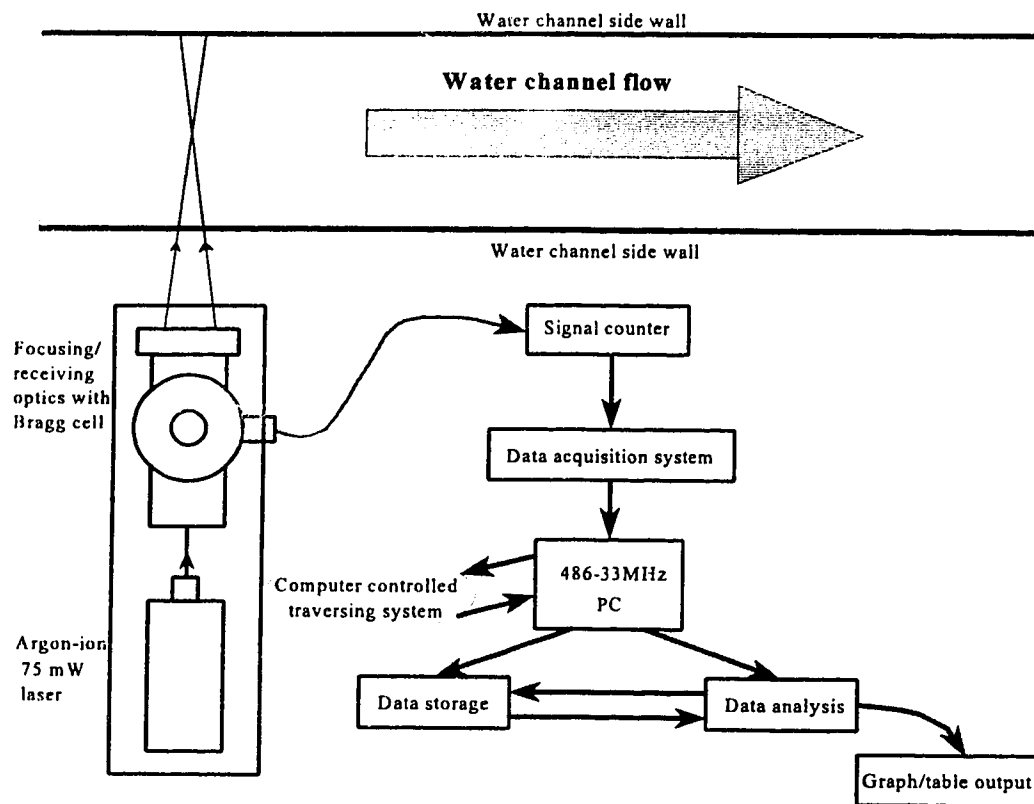


Figure 2.4 Schematic diagram for the LDV system

the presence of an obstacle to understand the plume dispersion process. LDV was used to measure the necessary flow characteristics.

The LDV system used was an Ion Laser Technologies (ILT) air cooled 300 mW argon-ion continuous wave laser. For the experiments conducted in the water channel, the laser was run in a single wavelength mode to generate 514.5 nm wavelength laser light. At this single wavelength, the rated power of the laser was reduced to 100 mW and further regulated down to 75 mW to increase the laser tube life.

The LDV system, shown in Figure 2.4, was mounted on a computer-controlled two-axis traversing system (cross-stream and vertical). The focusing/receiving optics were manufactured by Thermo Systems Inc. (TSI) and consisted of:

- beam splitter — separates the single laser beam emerging from the laser generator into two parallel and equal intensity beams;
- Bragg cell — shifts the frequency of one of the beams which enables the measurement of the negative (reversed flow) velocity. The TSI Bragg cell shifted the beam frequency up 20 KHz;
 - Beam expander — separates the two split laser beams further and makes each of them thicker to cover more of the focusing lens area, to produce a smaller measuring volume when the two beams intersect;
 - Focusing lens — focuses the expanded beams to an intersection point using spherical lenses. A 571mm focal length lens was able to cover the entire width of the channel cross section. A 351mm focal length lens had better spatial resolution because its wider half angle α produced a smaller measuring volume;
 - Receiving optics — focuses the scattered light back from the measuring volume onto the photomultiplier;
 - Photomultiplier — converts the light intensity into voltages and sends the electrical signals to a TSI 1980B signal processor. The information from the signal processor was then stored in a 486/33MHz PC for later analysis.

For the LDV to work properly, the flow must be seeded. To seed the flow, about 20mL of 3.0g/L titanium oxide (TiO_2) water mixture was poured in the water channel. This quantity of seeding solution was sufficient for about ten days. The data rate was approximately 350 randomly spaced points per second. The velocity data collected in the water channel used either 60 second or 500 second averages depending on what kind of the flow characteristics was required. A 60 second average was used for longitudinal

mean velocity data and a 500 second average was used if the x -component of turbulence intensity, length scale or Reynolds stress were needed. The software used to collect and analyse the raw data was written by Zelt (1991) and is described in detail in his Ph.D. thesis.

2.4.1 Velocity and Turbulence Intensity Over the Rough Surface

The velocity and turbulence intensity profiles evolve with distance from the entrance of the test section. After the flow reached $x' = 2500\text{mm}$ downwind of the test section inlet it became fully developed as Figures 2.6 and 2.7 show. All the model buildings, source and experimental data were collected in the region from $x' = 3000\text{mm}$ to $x' = 3600\text{mm}$ downwind of the test section entrance. The x -component of mean velocity, turbulence intensity, turbulence length scale and the Reynolds stress profiles in the fully developed flow at the location $x' = 3000\text{mm}$ are shown in Figure 2.8.

Using the mean velocity data measured from the fully developed flow on a rough surface, it was found that $Z_{o,exp} = 1.6\text{mm}$ by applying the log-law to the mean velocity profile in Figure 2.9. At a scale of 500:1, this corresponds to an urban environment with $Z_o \approx 0.8\text{m}$. This was quite close to the design value of $Z_o \approx 0.7\text{m}$ for which the roughness pins were specified. Also, u^* , the turbulent velocity (1.96 cm/s) from log-law is in good agreement with the value from measurement (2.06 cm/s), see Figures 2.8 and 2.9.

2.4.2 Rough to Smooth Flow Transition on the Building Base Plate

In order to mount the model buildings at various locations downstream of the ground level source, one roughness plate was replaced by a smooth plate as shown in the Figure 2.3. Measurement were made to determine how the flow responded to the sudden change of the roughness. From the velocity measurement results in the Figures 2.9 and 2.10, only the semi-log plot revealed that the bottom part of the boundary layer accelerated (as expected) as the surface roughness changed from rough to smooth.

Although the acceleration was confined to the bottom 15mm of the 350mm thick boundary layer, it had some effect on the spreading of the plume from the ground level source. The flow acceleration over the smooth plate caused an increase in flow mean convective velocity from $U_c = 70\text{mm/s}$ to $U_c = 95\text{mm/s}$ at $z = 5\text{mm}$ where the full-field dual laser light sheet profiles were taken.

Without a building present, at a plume height of $z \approx \sigma_z$, the mean velocity increased from $U_c = 85\text{mm/s}$ at $x = 60\text{mm}$ to $U = 140\text{mm/s}$ at $x = 350\text{mm}$ as the plume travelled downwind. With no rough to smooth transition this velocity change would have been from $U_c = 21\text{mm/s}$ at $x = 60\text{mm}$ to $U_c = 128\text{mm/s}$ at $x = 350\text{mm}$. This change due to the rough to smooth surface roughness transition was neglected in the theoretical model for Gaussian dispersion.

2.4.3 Model Buildings and Wind Direction Angles

Two model buildings, with aspect ratios of 1 to 0.5 to 0.4 and 1.0 to 1.0 to 0.4 (width to height to length) and made of clear plastic with dimensions 100mm wide \times 50mm height \times 40mm long for building *A* and 100mm wide \times 100mm height \times 40mm long for building *B*, were used in the current study.

The buildings were mounted at three locations, $x = 170, 270$ and 370mm downwind of the source and also rotated through wind angles of $0^\circ, 5^\circ, 10^\circ, 20^\circ, 30^\circ, 45^\circ, 60^\circ, 90^\circ$ to study the influence of wind direction on plume dispersion.

2.4.4 Velocity and Turbulence in the Vicinity of a Building

It is helpful in understanding plume dispersion behaviour if the mean velocity and turbulence characteristics in the building vicinity are known. Some measurements were

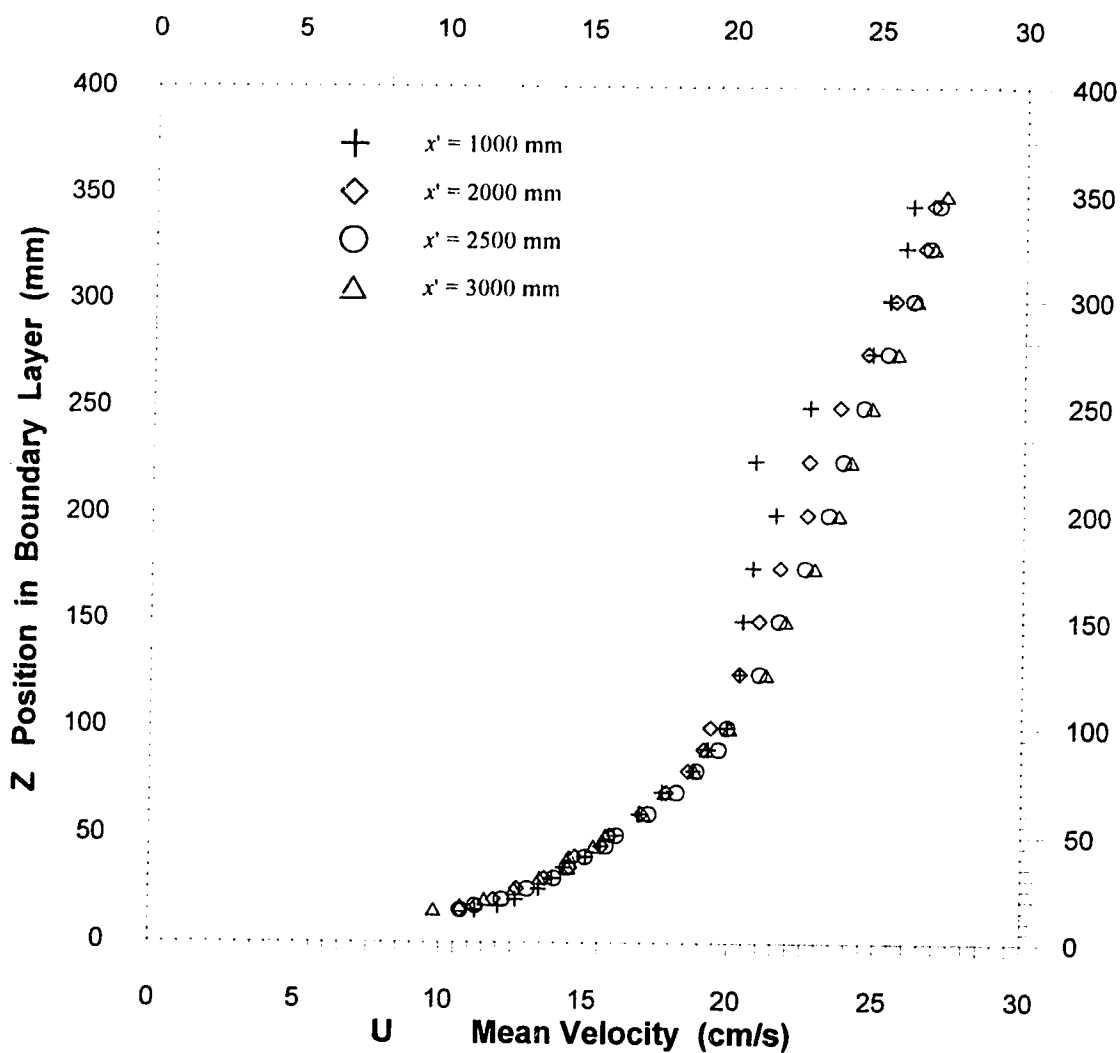


Figure 2.5 Evolution of the vertical velocity profiles in the boundary layer along stream (at $x' = 1000, 2000, 2500, 3000$ mm downwind of the channel entrance)

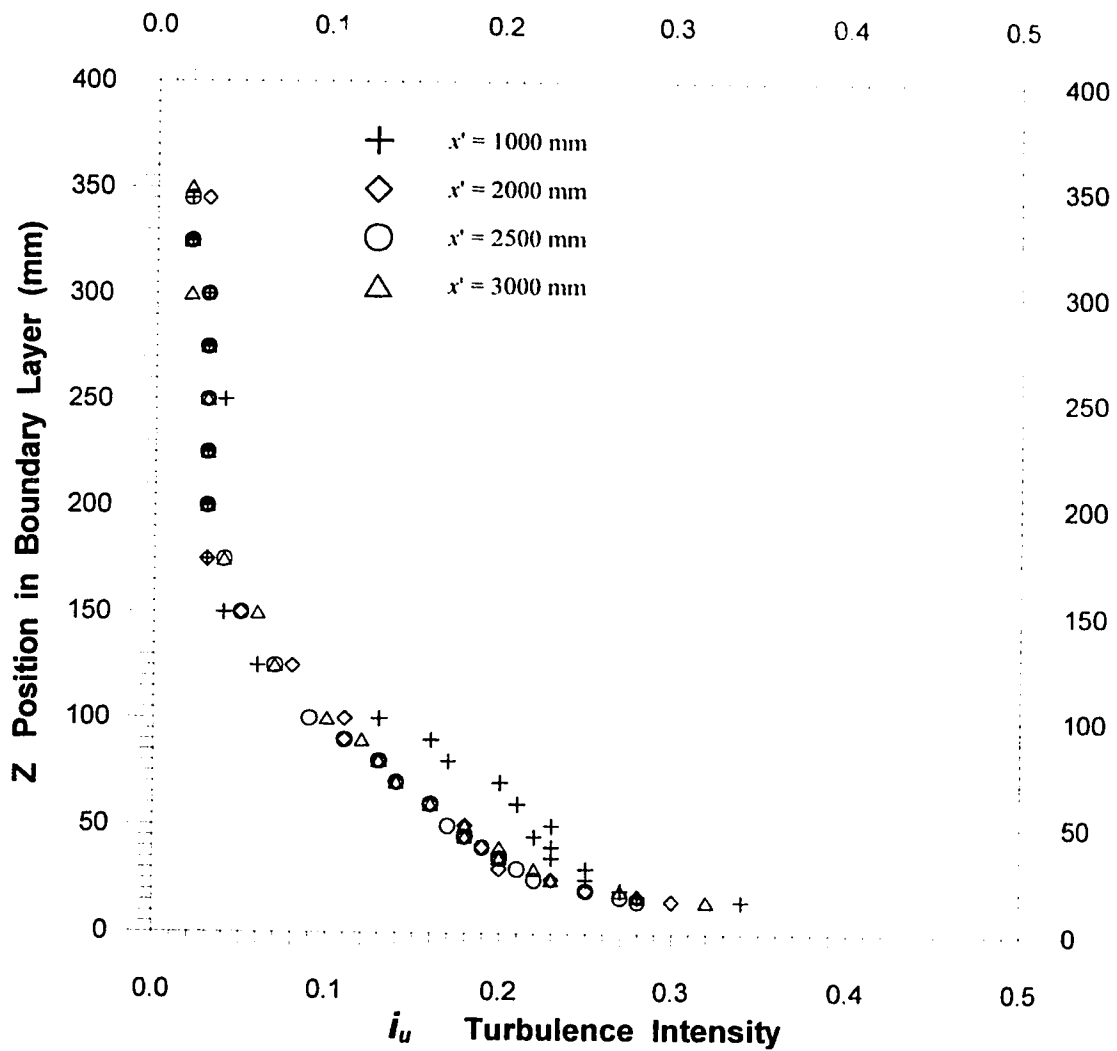


Figure 2.6 Evolution of the turbulence intensity in the boundary layer along stream (at $x' = 1000, 2000, 2500, 3000$ mm downwind of the channel entrance)

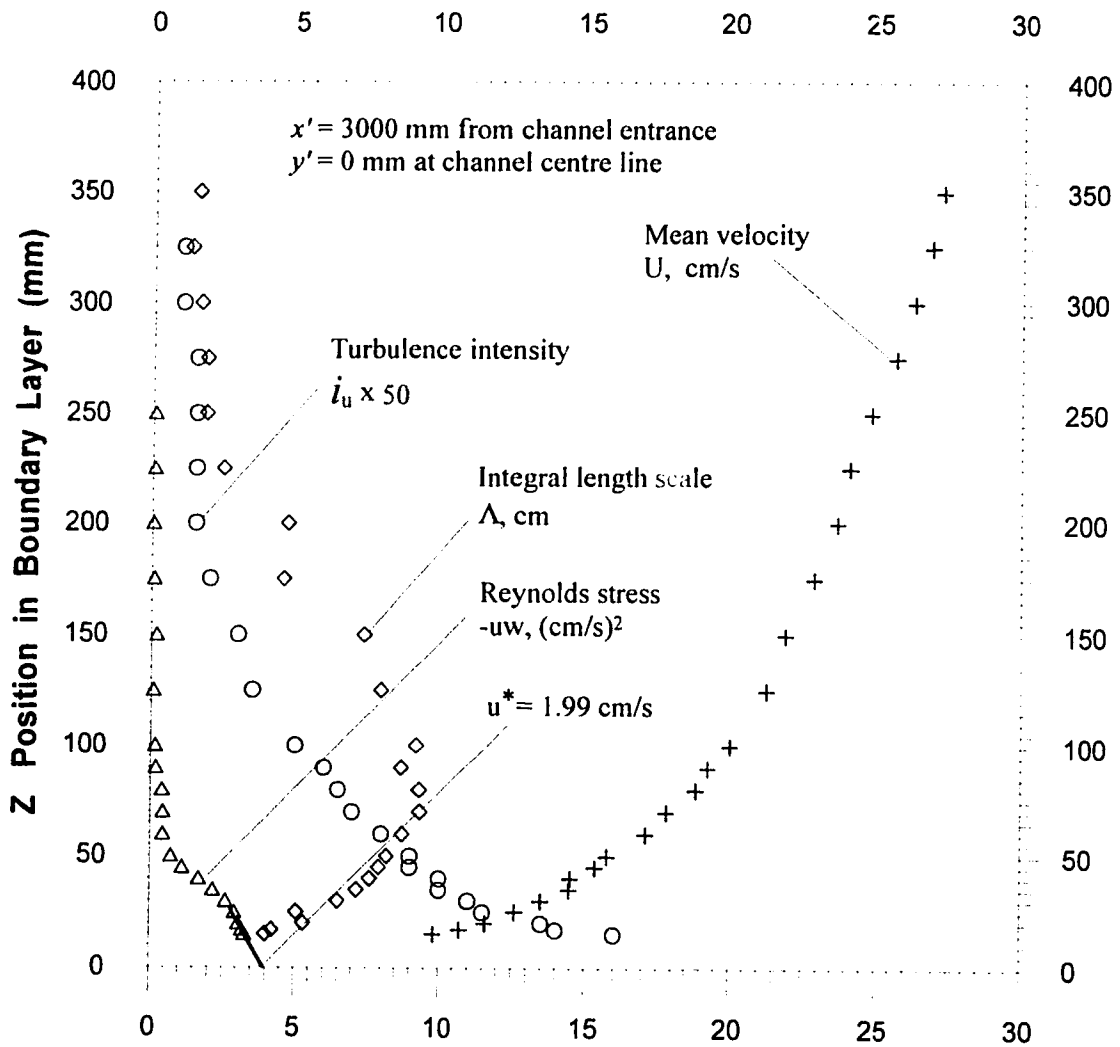


Figure 2.7 Mean velocity U , turbulence intensity i_u , turbulence length scale Λ and Reynolds stress $-uw$ from the fully developed channel flow at $x' = 3000$ mm downwind of the channel entrance

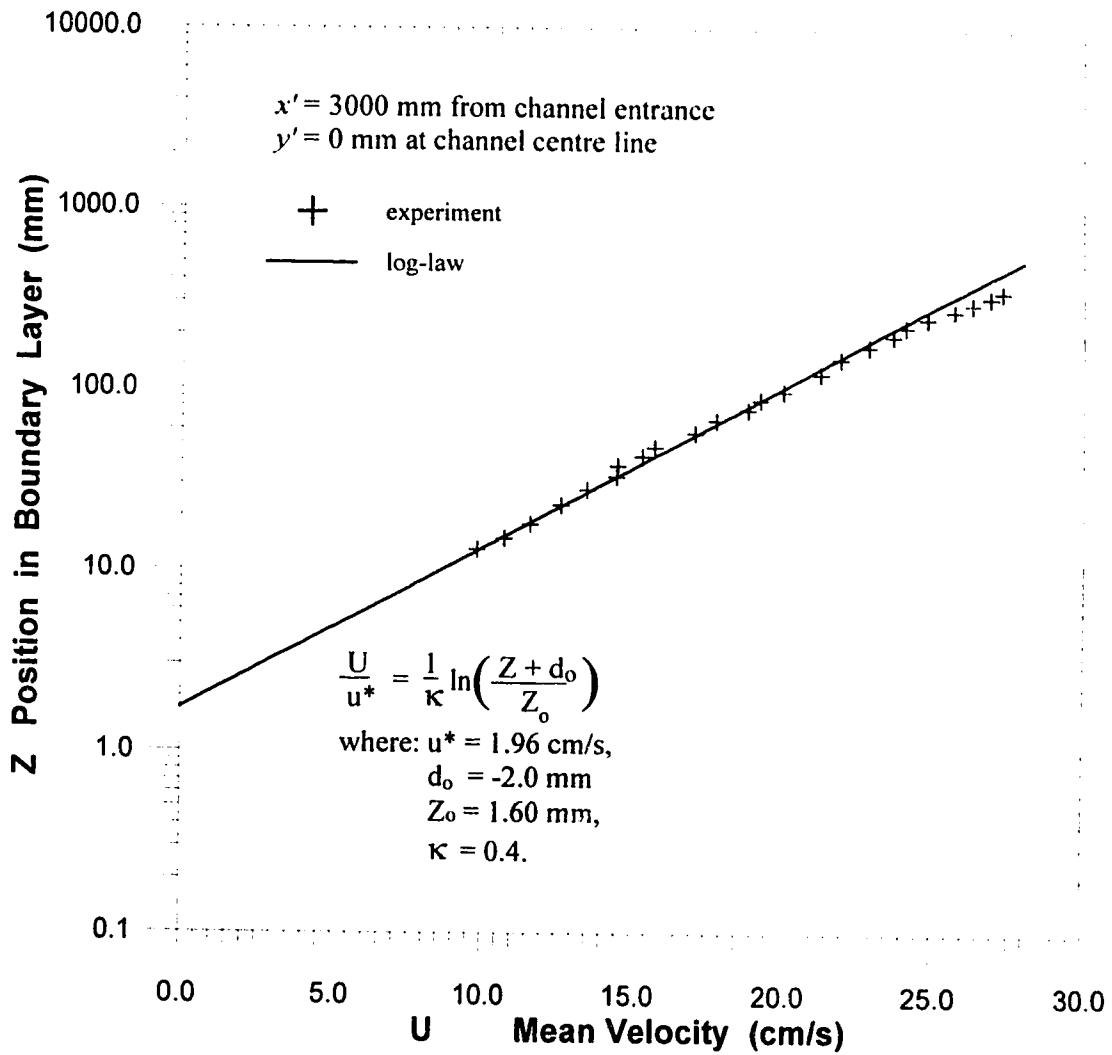


Figure 2.8 Fitting measured velocity data using log-law for the fully developed channel flow at $x' = 3000$ mm downwind of the channel entrance

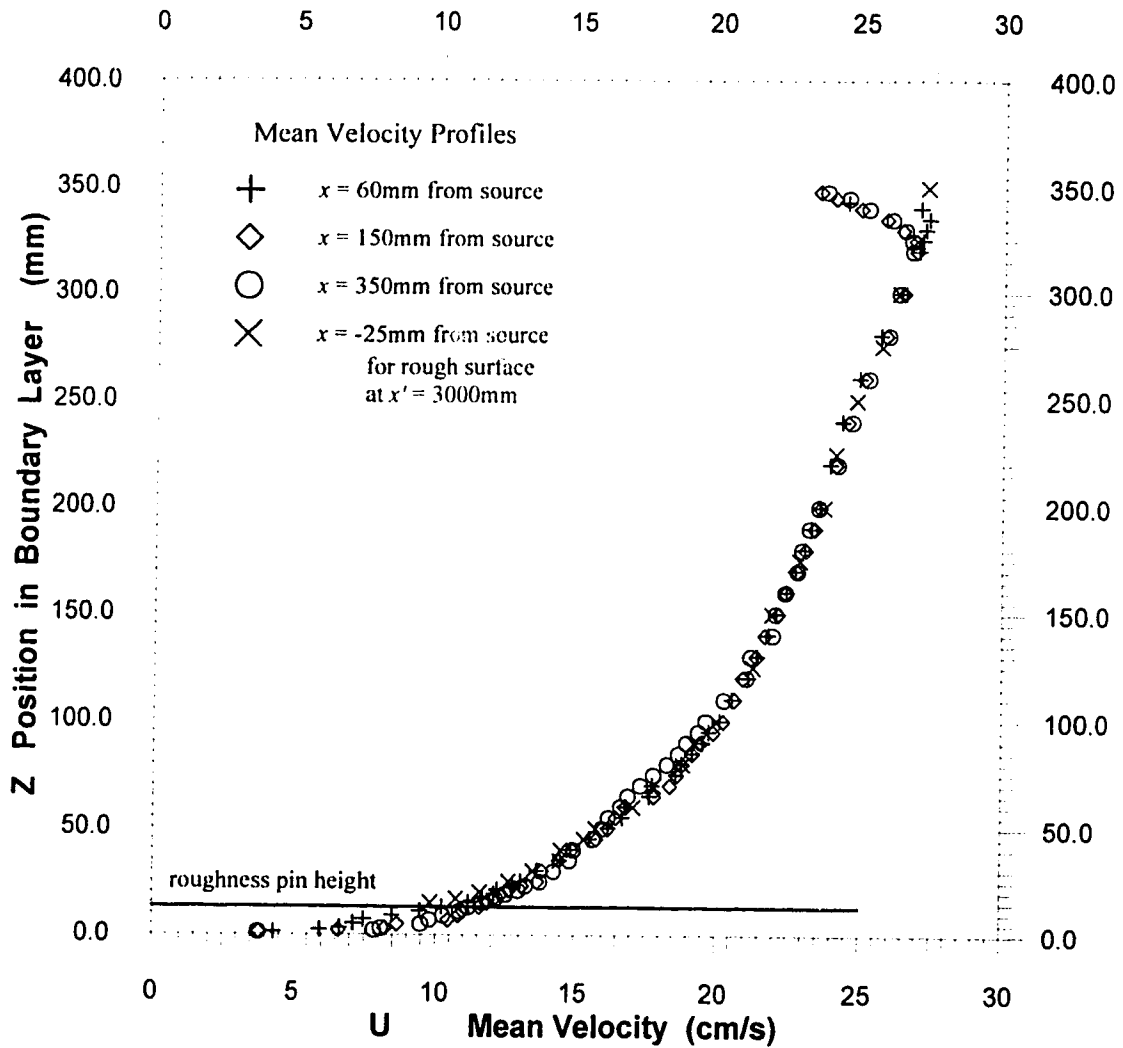


Figure 2.9 Mean velocity profiles over the smooth plate and rough surface

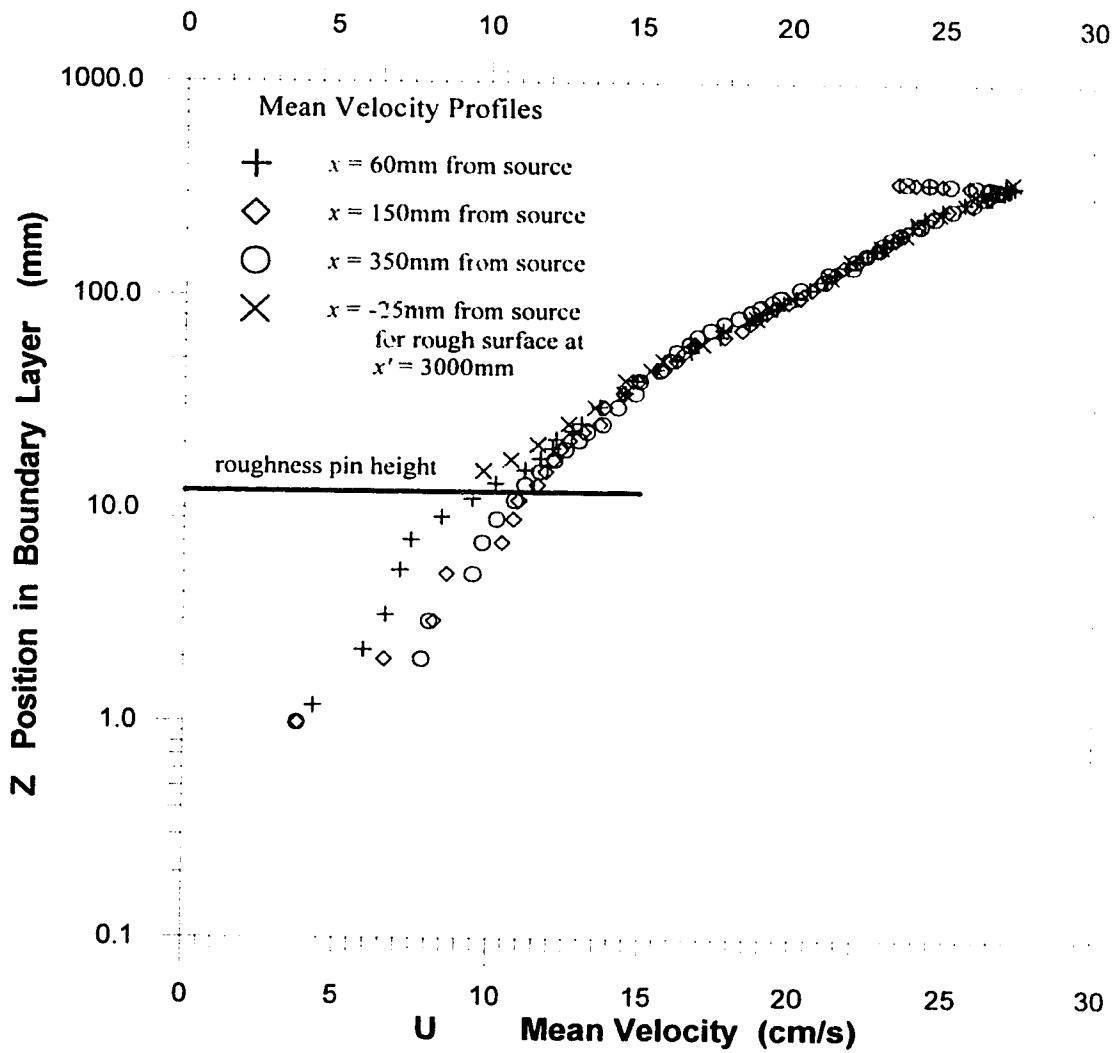


Figure 2.10 Semi-log plot of mean velocity profiles on the smooth plate and rough surface

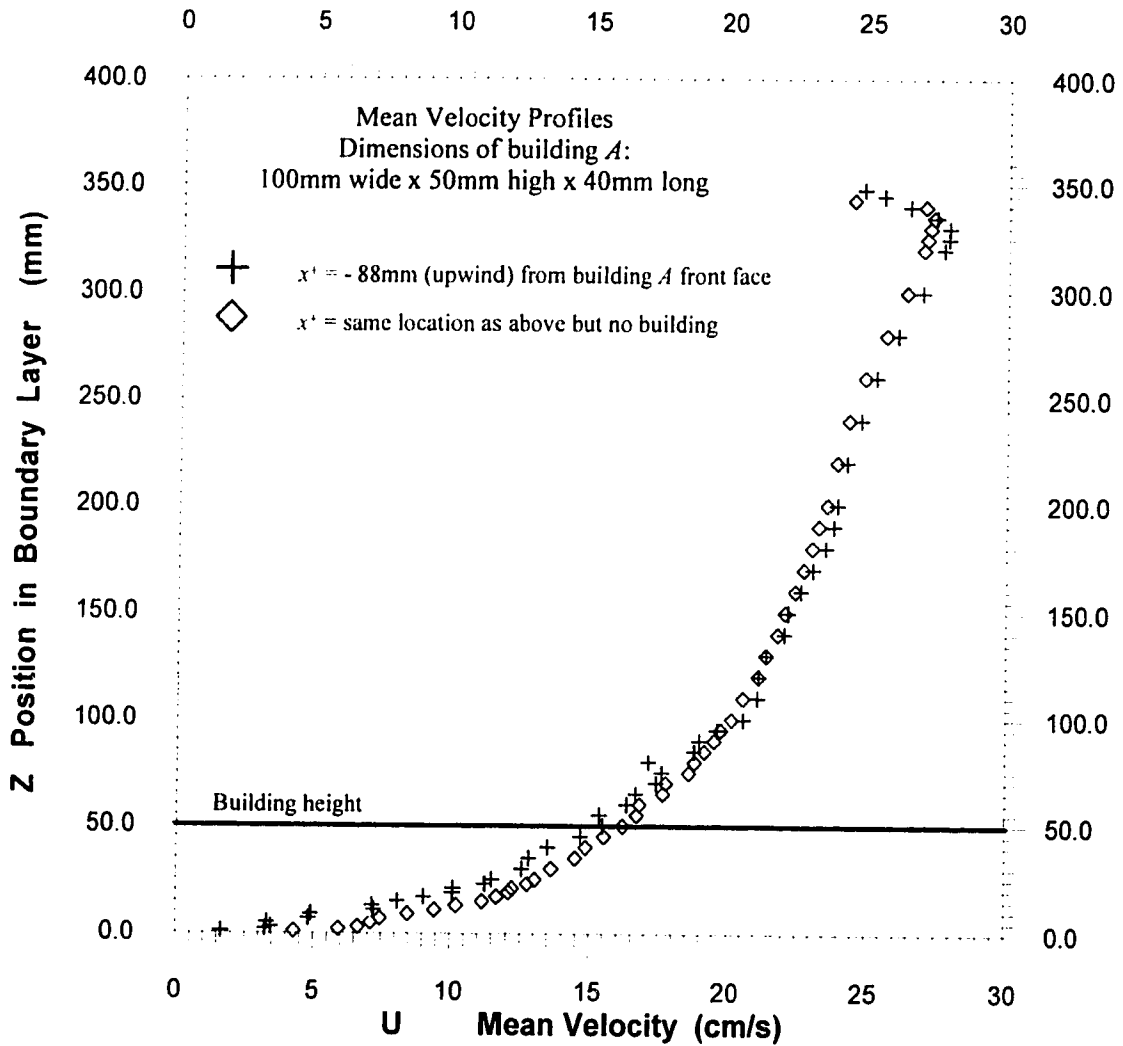


Figure 2.11 Mean velocity profile with and without building at $x^* = 88$ mm upwind from building *A* front face (building at $x = 170$ mm from the source location)

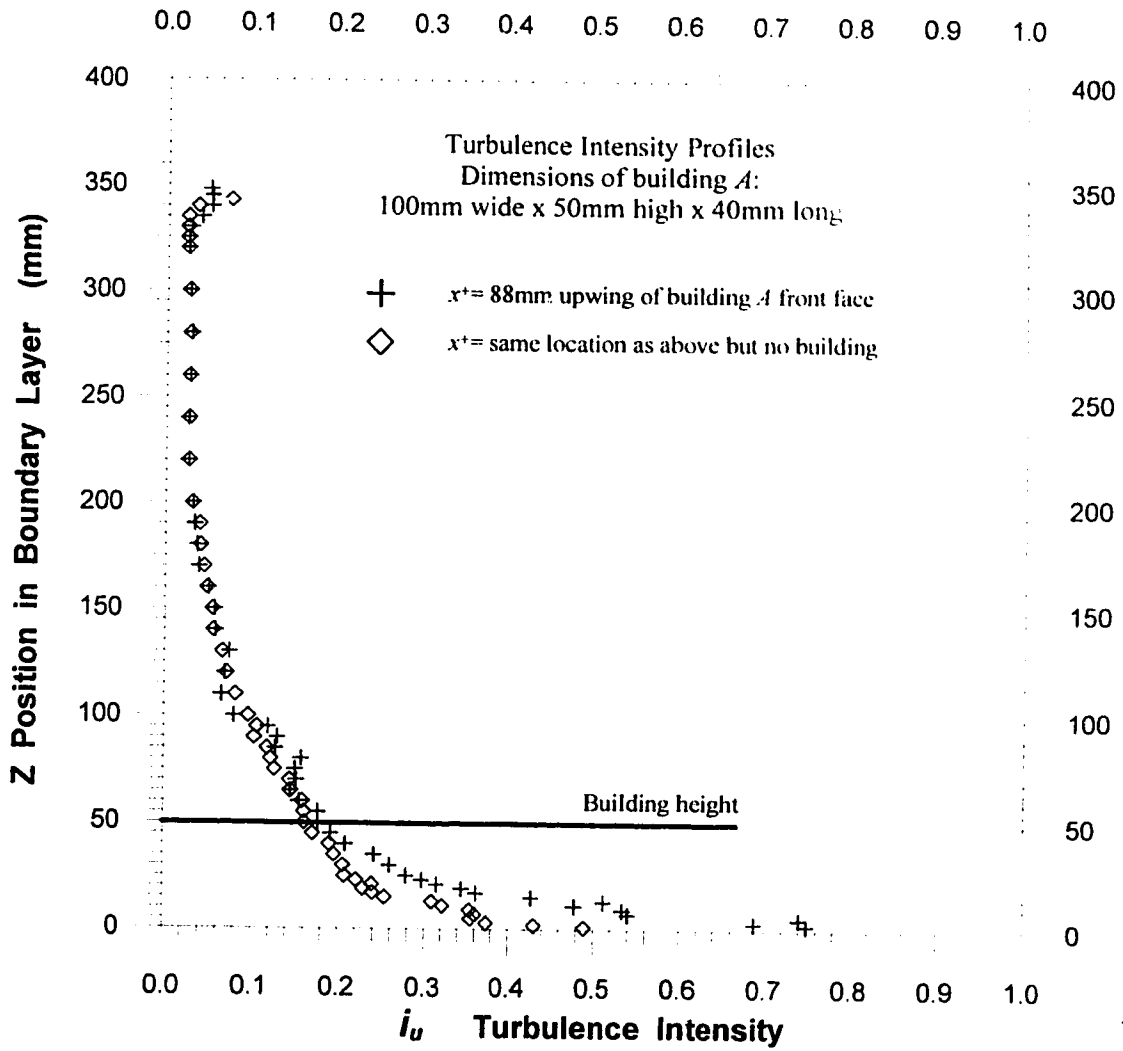


Figure 2.12 Turbulence intensity profile with and without building at $x' = 88$ mm upwind from building *A* front face (building at $x = 170$ mm from the source location)

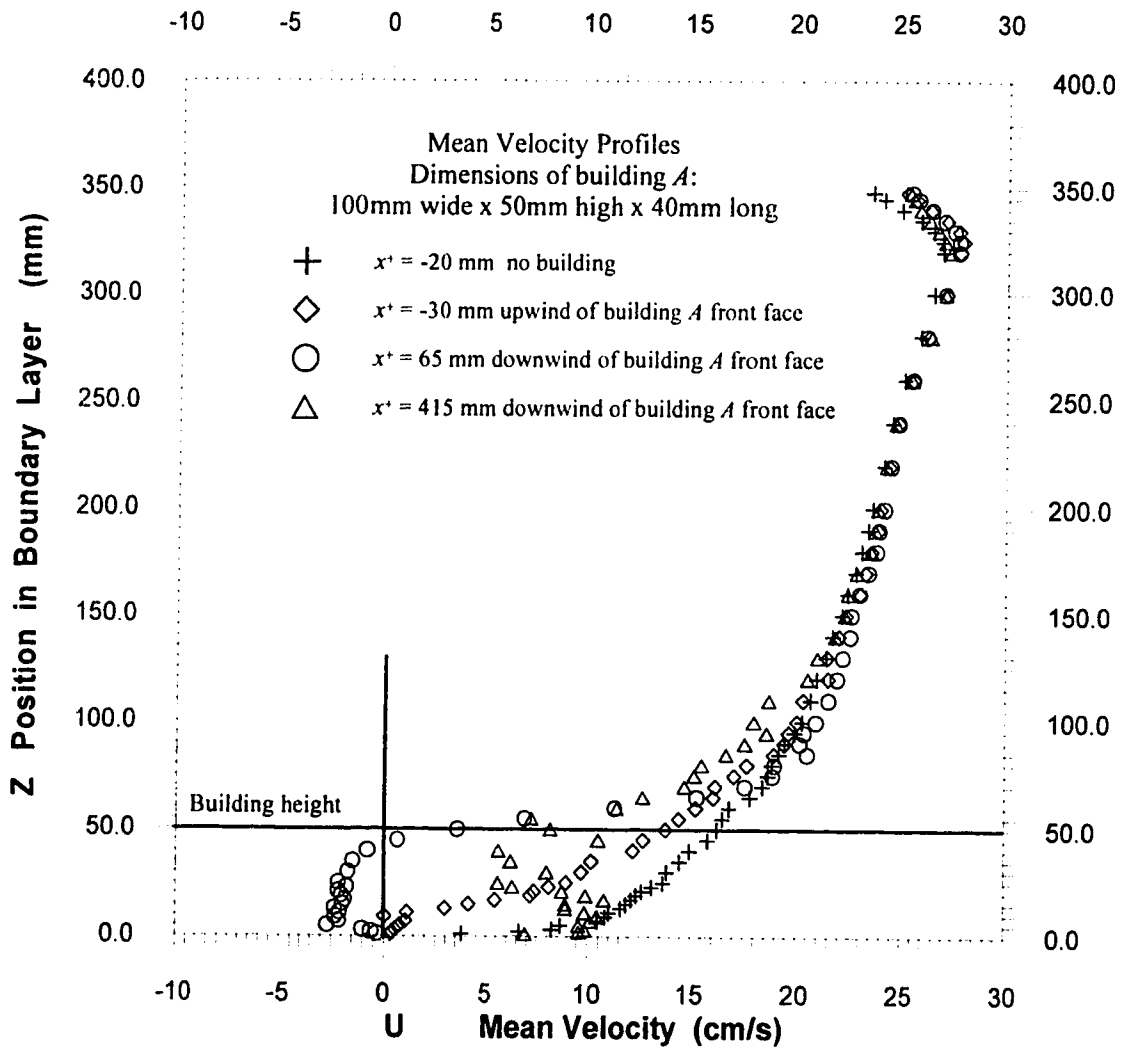


Figure 2.13 Mean velocity upwind and downwind of building *A* (located at $x = 170$ mm from the source) front face for data measured at $x^+ = -20, -30, 65$ and 415 mm (with the no building profile as reference)

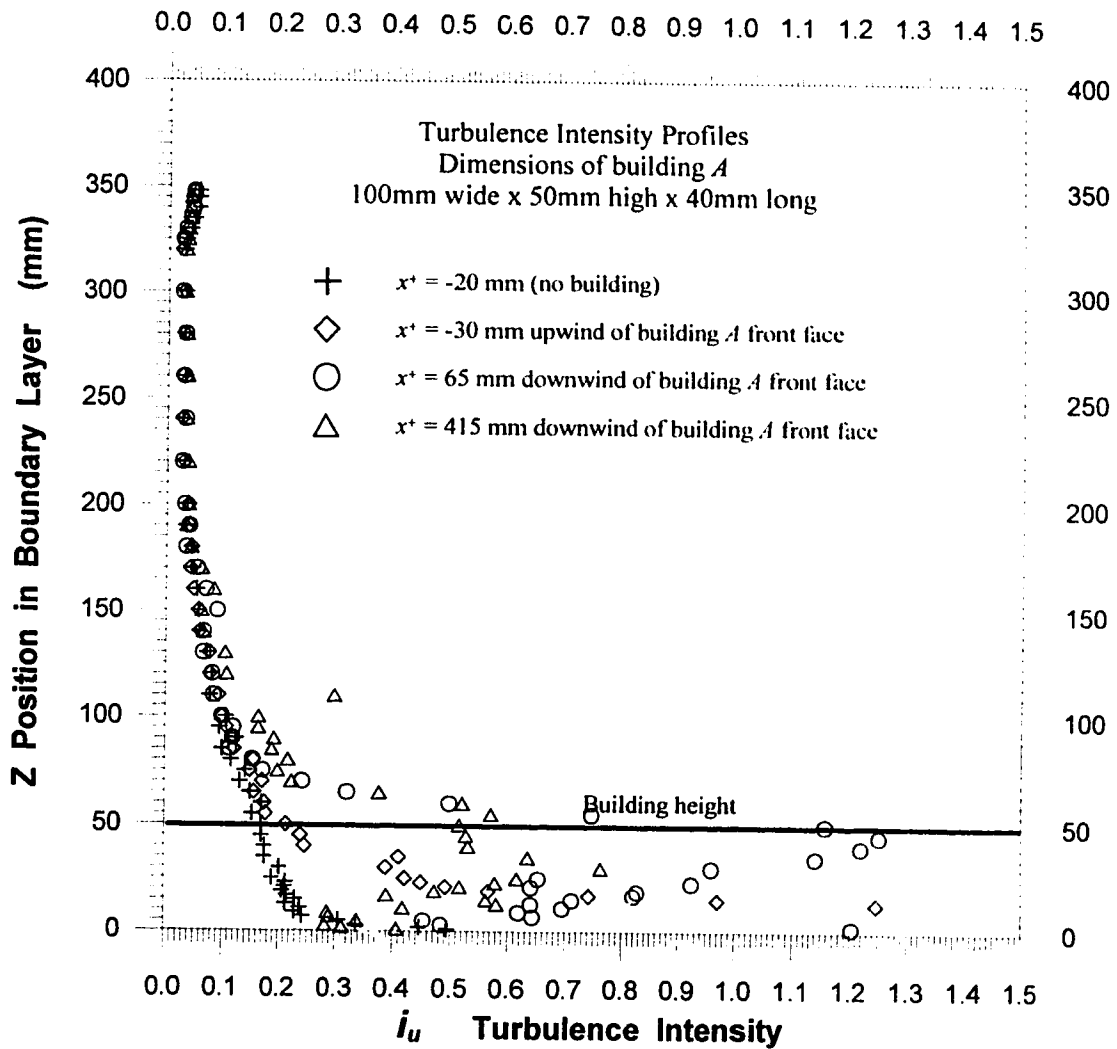


Figure 2.14 Turbulence intensity upwind and downwind of building *A* (located at $x = 170$ mm from the source) front face for data measured at $x^* = -20, -30, 65$ and 415 mm (with the no building profile as reference)

carried out in the wake of building *A*. Figures 2.11 and 2.12 shows that the building upwind mean velocity and turbulence intensity did not change significantly in the flow approaching the building. Here, the effect of the building is to cause the upwind streamlines (and the ground-level plume) to diverge, see Figure 2.26.

Figures 2.13 and 2.14 show the recirculation flow in the near wake region of the building, and the slow flow out to eight building heights downwind.

2.5 Tracer Source

Disodium fluorescein is a good tracer to reveal the turbulent dispersion of a plume because it has a completely independent process of absorption and emission of light, a wide measurable concentration range and the dye absolute concentration is easy to determine (Walker ,1987).

Disodium fluorescein tracer, commercially called Uranine, with a molecular weight of 276.28g/mol was first dissolved in distilled water to form a highly concentrated solution in a two litre flask . Then the concentrated solution was then further diluted in a 20 litre container using ordinary tap water and transferred to the 80 litre pressure vessel shown in Figure 2.3. The vessel was pressurized by compressed air which was regulated to 70 kPa. The tracer solution then passed through a needle valve for fine control of the flow rate and a toggle shut-off valve.

A rotameter with a range from 0.0 to 13.0 cm³/s was calibrated by measuring the volume flow in 60 second intervals for various nominal rotameter readings and the results, as shown in the Figure 2.15, showed good agreement with the claimed response by the manufacturer. At the injection flow rate of 1.2cm³/s used in the current experiment, the rotameter was accurate within 5%.

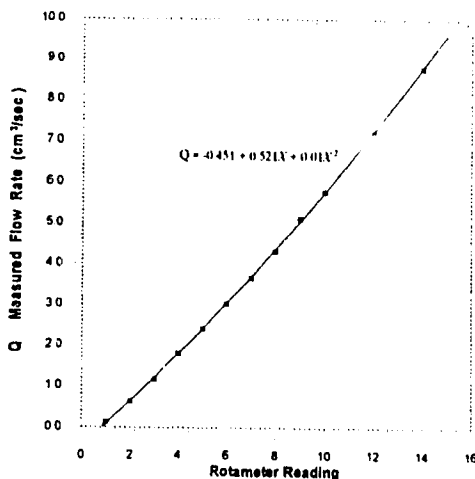


Figure 2.15 Calibration of the rotameter used in the current experiment for tracer dye flow control

2.5.1 Ground Level Tracer Source

A 10mm diameter circular area source shown in Figure 2.16 was used to release the concentrated dye solution into the boundary layer. The fluorescein dye tracer solution emerged from this flush circular hole after passing through a plastic foam pad to distribute the flow uniformly over the source area. At the source vertical velocity of 15mm/s used in this study, vertical momentum was negligible compared to the momentum produced by the flow over the top of the roughness elements at a velocity of 100mm/s.

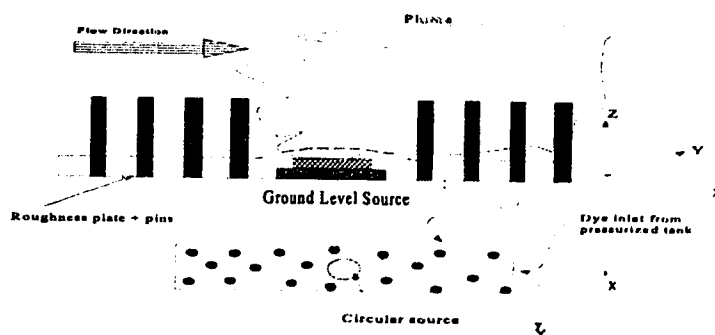


Figure 2.16 Schematic diagram of dye source

2.5.2 Behaviour of Disodium Fluorescein Tracer Dye

The fluorescent dye molecules have a broad absorption and fluorescence emission spectra, and the emitted light wavelength is always longer than the absorbed light wavelength (Walker, 1987). When excited by the argon-ion laser with a wavelength of 514.5nm, disodium fluorescein emits visible light at wavelengths ranging from 530nm to 580nm, with the peak value at 550nm. The difference in the light wavelength between the laser and the dye fluorescence allowed the laser light to be removed (leaving the dye fluorescence) by using a Kodak Wratten No.21 gelatin filter on the video camera.

As described by Walker (1987), the intensity of the emitted light from fluorescein dye is affected by:

- dye concentration;
- excitation light intensity;
- dye solution pH;
- dye temperature.

Lingqvist (1960) and Walker (1987) showed that the emission intensity of disodium fluorescein dye decreases if the dye pH value falls below 8.0. It was found by measurement that the pH value of water in the channel was slightly above 8.0, so no pH balancing buffer solution was required.

According to Walker (1987), with dye pH value ≥ 9.0 , the intensity variation of dye fluorescence is no more than 0.3% per degree Kelvin. To minimize this temperature effect, the dye solution in the injection tank and the water in the channel were allowed several hours to reach room temperature after they were refilled. Hot water was added when filling the water channel to ensure dye and the channel water had about the same temperature. Water temperature during each run of experiments was found very steady and only increased about 1.0K for two hours continuous running of the channel. Since the channel needed draining and refilling after about 50 minutes of run time to remove the

background concentration buildup, temperature effects are negligible.

Under normal conditions in the laboratory, the emitted light intensity of the fluorescein dye is the function of input laser light intensity and the concentration of the fluorescein dye solution.

2.6 Linescan Concentration Measurements

Some concentration measurements were made using the linescan method, with the plume illuminated by a single laser beam generated by the LDV laser. In order to use the LDV laser to produce a single laser beam for linescan measurement, two mirrors shown in Figure 2.17 were used to by-pass the LDV focusing/receiving optics. The beam was about 1mm in diameter in the water, the same as the distance between two pixels on the digital video image.

Because the maximum spatial resolution of the image system was also about 1mm, there was no need to make corrections for the Gaussian intensity distribution across the laser beam. However, the light attenuation along the beam path was not negligible, especially where the plume concentration was high. The light attenuation corrections are discussed later and also in more detail in Appendix A. Attenuation corrections were applied to each collected linescan image before converting the intensity data into concentration and time averaging the concentration values.

An image processing system was used to collect the data from each run of experiment (see Figure 2.18). The frame grabber, which digitized the signals from the video camera, played a key role in the image processing system. The process was divided into three steps:

- collection of digitized images;
- correction for background, laser beam attenuation and system non-linearity;
- determination of plume mean concentration.

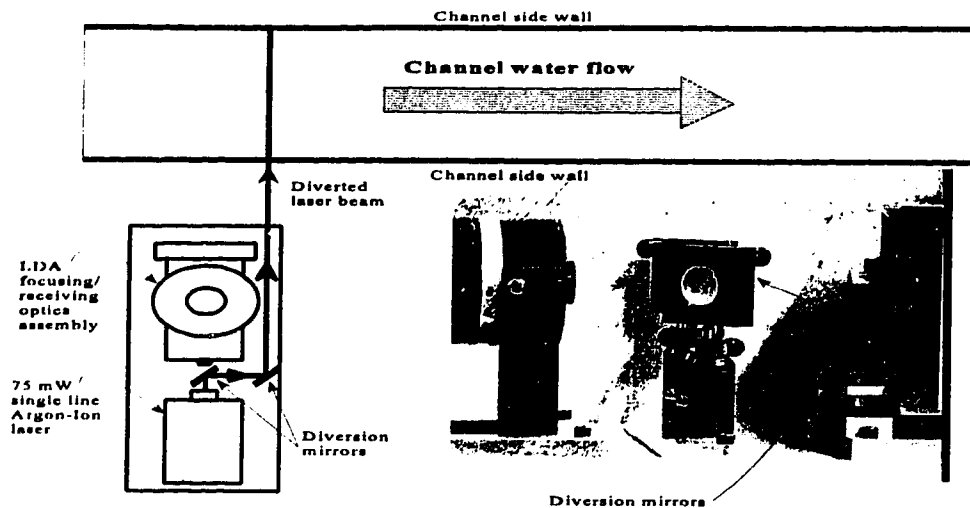


Figure 2.17 Schematic diagram of the single laser system

2.6.1 Image Acquisition

The raw data containing instantaneous intensity information were recorded directly to a computer hard disk using a binary format for each run of 300 seconds at a speed of 15 frames per second. The colour video camera and the frame grabber in the 486-33 MHz PC were used together to convert and digitize video signals into RGB (red, green, blue) signals. The camera used was a SONY DXC-151 S-VHS/RGB colour video camera. It has a built in interline transfer CCD (Charge Coupled Device) with 768 horizontal \times 493 vertical picture element resolution and an electronic shutter range from $1/30^{\text{th}}$ of a second to $1/10,000^{\text{th}}$ of a second. A shutter speed at $1/250^{\text{th}}$ of a second was used when collecting linescan data because at this shutter speed a particle in the bulk fluid moved only one pixel's distance (less than 1mm) in the streamwise direction, matching with the spatial resolution of the image system.

The frame grabber, a Data Translation model DT2871, was used to digitize and translate the standard RGB television signals into HSI (hue, saturation and intensity) signals. HSI mode was chosen because light intensity is directly related to dye concentration. Intensity

information in each pixel was stored as an 8 bit integer, so only 256 intensity levels could be recorded for each pixel.

Even though each digitized output image from the frame grabber has a resolution of 512×512 pixels, the video signals used only 480 of the horizontal lines which left the last 32 lines unused. The maximum value from the nine video lines in the neighbourhood of the illuminated line (i.e. 9×512 pixels), was chosen to account for the laser and camera misalignment and stored for later analysis.

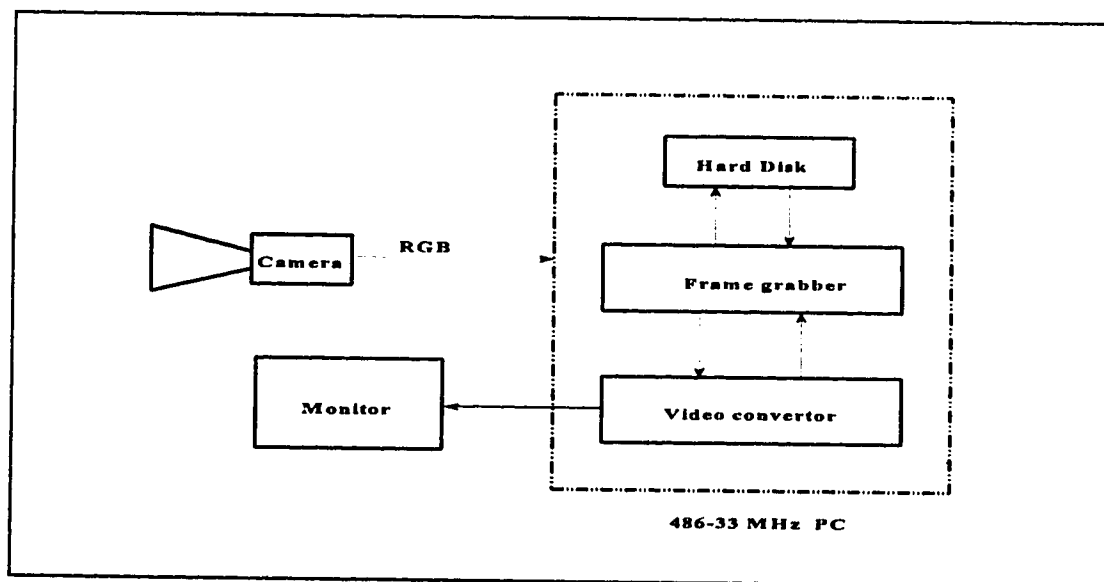


Figure 2.18 Schematic diagram of image acquisition and processing system

2.6.2 Linescan Image Correction

The correction and analysis of images was done separately from the image acquisition process. The first step in the process was to correct for light attenuation effects along the beam path. This light attenuation can be neglected only when the dye concentration is very low, see details in Appendix A. Assuming that there is no radial expansion of the laser beam in the water channel, the laser beam attenuation along the beam path is solely due to dye absorption and governed by Lambert-Beer Law (see Brungart, Petric and *et al*,

1991). This assumes that attenuation is linearly proportional to the local dye concentration C with a constant of proportionality ϵ (defined as the laser extinction coefficient with units of $[\text{mm} \cdot (\text{mol}/\text{litre})]^{-1}$),

$$\frac{dI_{in}}{I_{in}} = -\epsilon C dy \quad (2.4)$$

where dI_{in} is the loss of light intensity due to absorption over the beam length dy with

the local dye concentration C . The fluorescent light output is related to the input laser intensity through a calibration function f as:

$$I_{out} = I_{in} f(C) \quad (2.5)$$

However, in the experiments it was found that the camera actually responded to input light intensity in a non-linear fashion, not the desired linear response shown in Figure 2.19. Therefore, an empirical exponent α was imposed to account for this camera non-linearity and the modified Equation (2.5) is,

$$I_{cam,i} = (I_{in,i})^\alpha f(C) \quad (2.6)$$

where α was found by correlating attenuated images at varying intensities to be,

$$\alpha = \left(1 - \frac{I_{cam,i}}{255.0} \right) \quad (2.7)$$

A discrete pixel-by-pixel form of Equation (2.5) derived from Equations (2.7) and (2.5) is shown in Appendix A to be,

$$f(C_i) = \frac{I_{cam,i} - \beta_i}{I_{in,0} \prod_{j=0}^{i-1} (1 - \epsilon \alpha C_j \Delta y)} \quad (2.8)$$

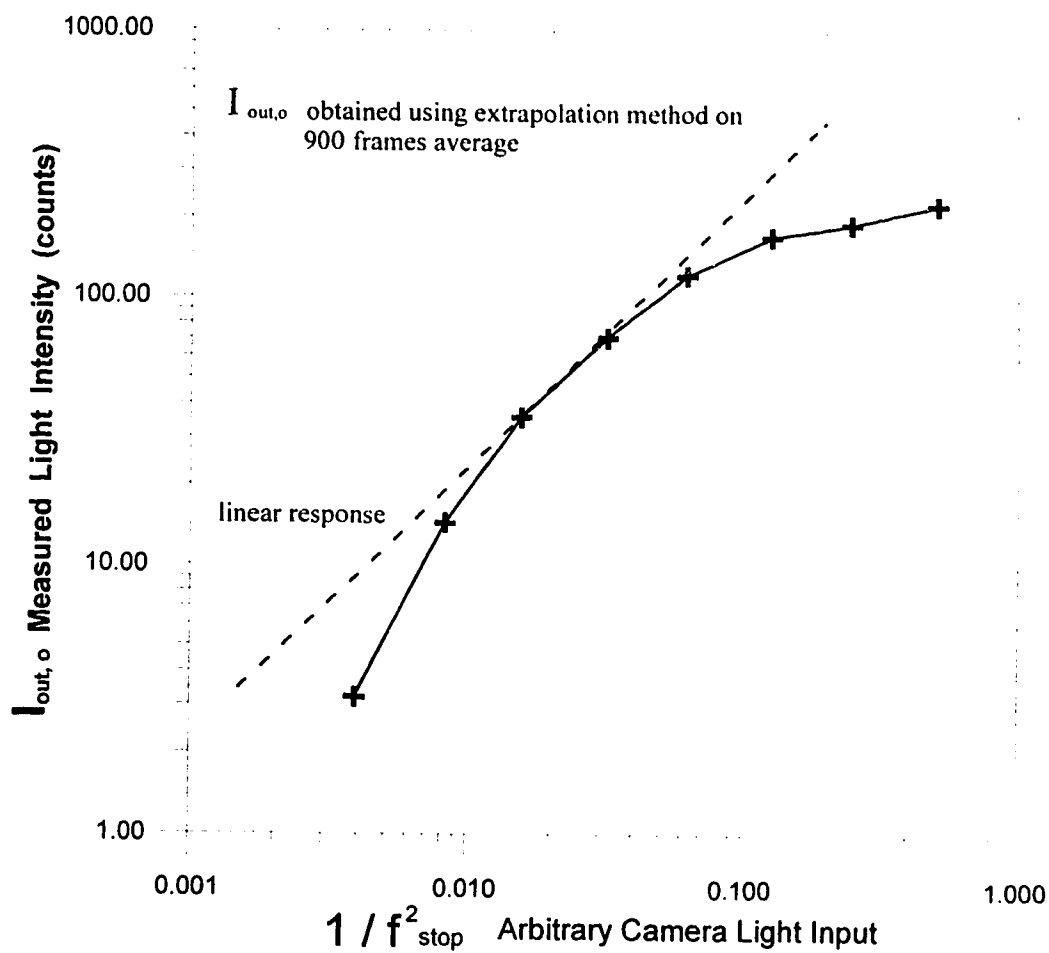


Figure 2.19 Non-linear response of the camera to light intensity input (proportional to inverse square of lens f -stop setting) when shutter speed = 1/250 sec and dye concentration $C = 6.25 \mu\text{mol/litre}$ were used

where:

- $I_{cum, i}$ = i^{th} measured pixel intensity (digital counts);
- β_i = clear water pixel response of the image system (digital counts);
- ϵ = fluorescent dye absorption extinction coefficient ($[\text{mm} \cdot (\text{mol}/\text{litre})]^{-1}$);
- α = empirical exponent defined as in Equation (2.7);
- Δy = the beam path length of one pixel in the Linescan image (mm);
- C_i = dye concentration at i^{th} pixel location (mol/litre).

The second step in the correction process was to remove the background dye concentration. Because the dye released into the channel was recirculated, the background dye concentration increased with time. An average background concentration value for each pixel was obtained by taking the mean of the concentration from 50 frames collected at the beginning and the end of each experimental run. The time average of background concentrations for each pixel from the 50 frames collected at the beginning or end of a run was obtained by averaging the sum of the instantaneous concentration of each pixel from each frame over the total frames collected and applying the attenuation correction to each pixel in each collected frame separately. The average background concentration for each pixel was subtracted from each of plume concentration profiles. The background dye fluorescent intensity in the channel varied from 0 to 20 digital counts (out of a range of 0-255 for intensity) depending on the dye background concentration level.

2.6.3 Determination of Fluorescein Dye Mean Concentration

Two sets of known concentration calibration bottles were prepared by successively diluting the previous bottle solution by a factor of two. The initial (the highest) concentration solution was made by weighing an appropriate amount of fluorescein dye powder (with molecular weight of 376.28g/mole) and dissolving it in distilled water. The first set of 12 bottles with dye concentrations were prepared to cover the range from 100.0 $\mu\text{mol}/\text{litre}$ down to 0.05 $\mu\text{mol}/\text{litre}$. The second set calibration bottles consisted of 10 bottles with concentrations ranging from 70.0 $\mu\text{mol}/\text{litre}$ to 0.14 $\mu\text{mol}/\text{litre}$. To avoid

saturation of the video camera, two camera aperture settings, $f_{\text{stop}} = 1.4$ and $f_{\text{stop}} = 5.6$, were used.

A 60 second time average intensity was used for linescan bottle calibrations. Assuming there was no light attenuation when the excitation laser beam first encountered the dye solution, the measured intensity on a line through bottle was extrapolated to the edge of a bottle by fitting the measured intensity data through the modified Lambert-Beer Law, as shown in Figure 2.20. See Appendix A for details. Using the extrapolation method calibration curves were obtained and plotted in Figure 2.21. Then, these calibration curves were used to generate the conversion function $f(C)$ in Equation (2.6) to convert the corrected fluorescence intensity data into corresponding concentration values. The equations used to fit the non-linear calibration curves for different camera aperture settings were:

when $f_{\text{stop}} = 1.4$,

$$C = 0.940 \exp(0.0095 I) - 0.894 \quad (2.8)$$

and when $f_{\text{stop}} = 5.6$,

$$C = 44.38 \exp(0.0163 I) - 43.86 \quad (2.9)$$

With units of I in digital counts and C in $\mu\text{mol/litre}$. For each image (approximately 15 images per second for 300 seconds, a total of 4,500) these intensity conversion equations were applied to successive pixels along the beam path to convert the attenuation-corrected intensity data to concentration.

To deal with the day-to-day variation of the laser initial intensity (i.e. $I_{m,0}$), a calibration bottle was used at the beginning of each set of data collection runs to define the $I_{m,0}$ with the curves in Figure 2.21 as the standard response of the imaging system. Assuming the change in the calibration curve (shown as dotted or dashed lines in Figure 2.22) was due solely to the variation of the laser output power, the calibration curve was shifted along

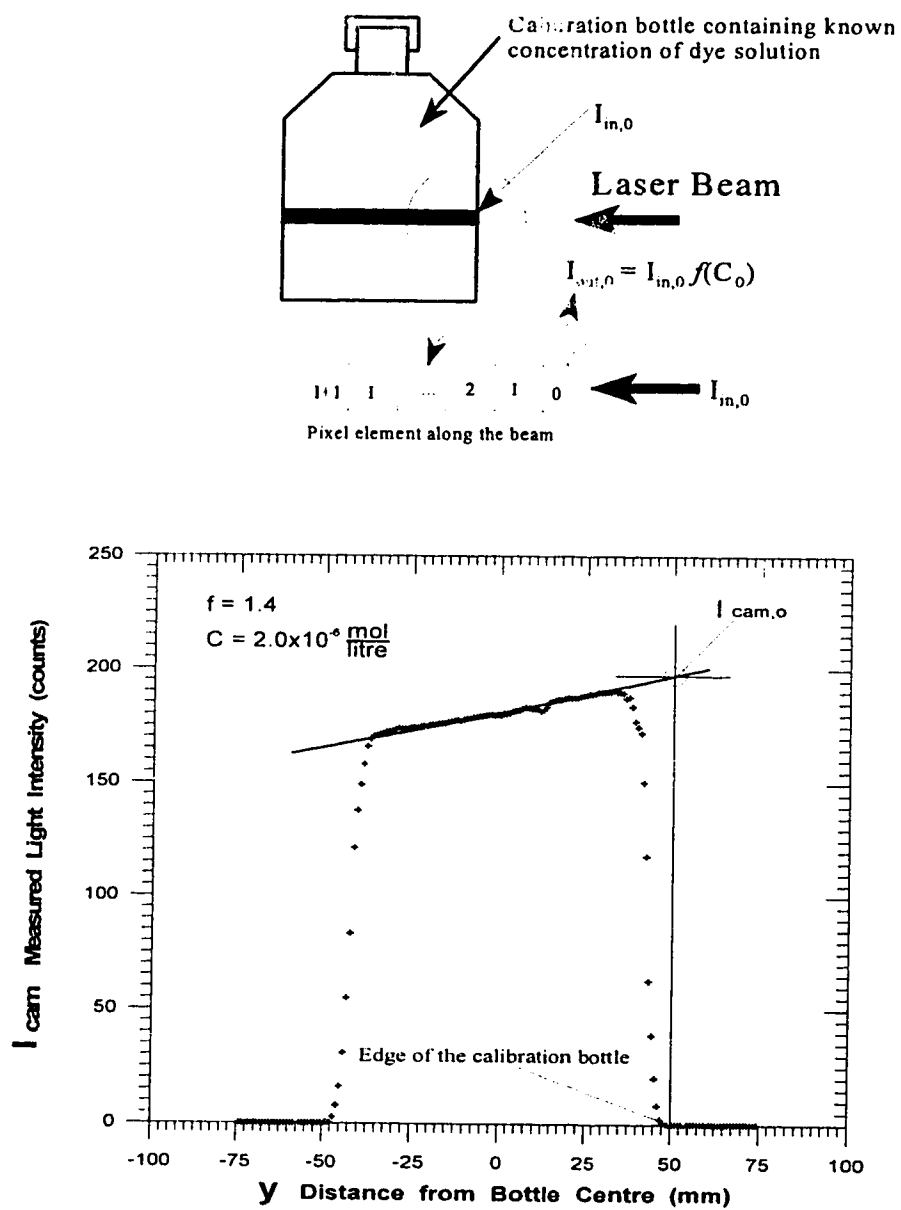


Figure 2.20 Illustration of linescan intensity measurement for a calibration bottle

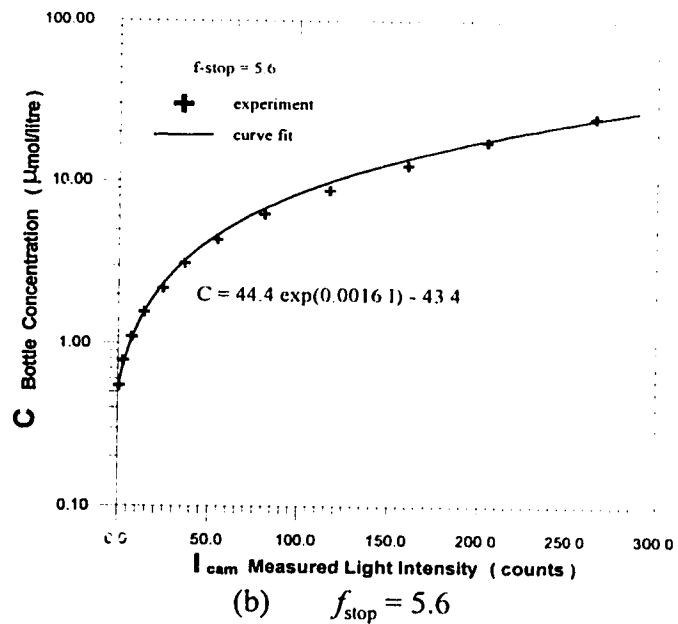
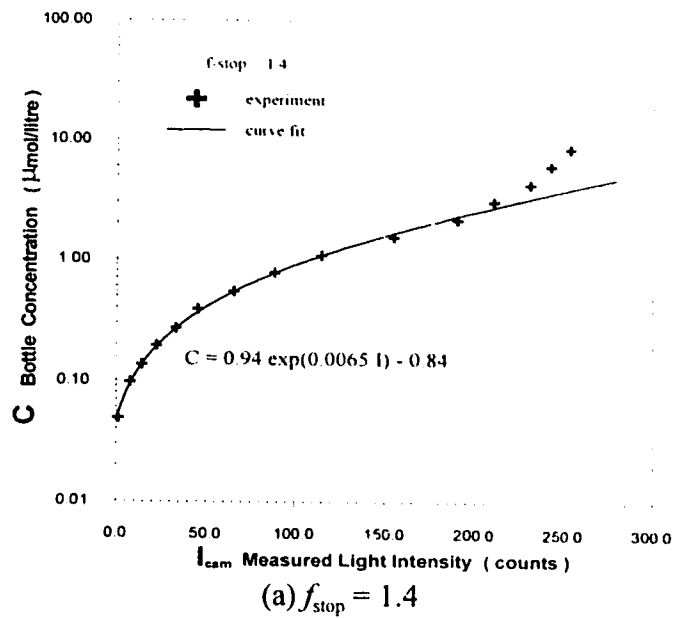


Figure 2.21 Non-linear response of the image system at apertures set at $f_{\text{stop}} = 1.4$ and $f_{\text{stop}} = 5.6$ (camera shutter speed: $1/250$ sec, and Kodak No.21 gelatin filter were used)

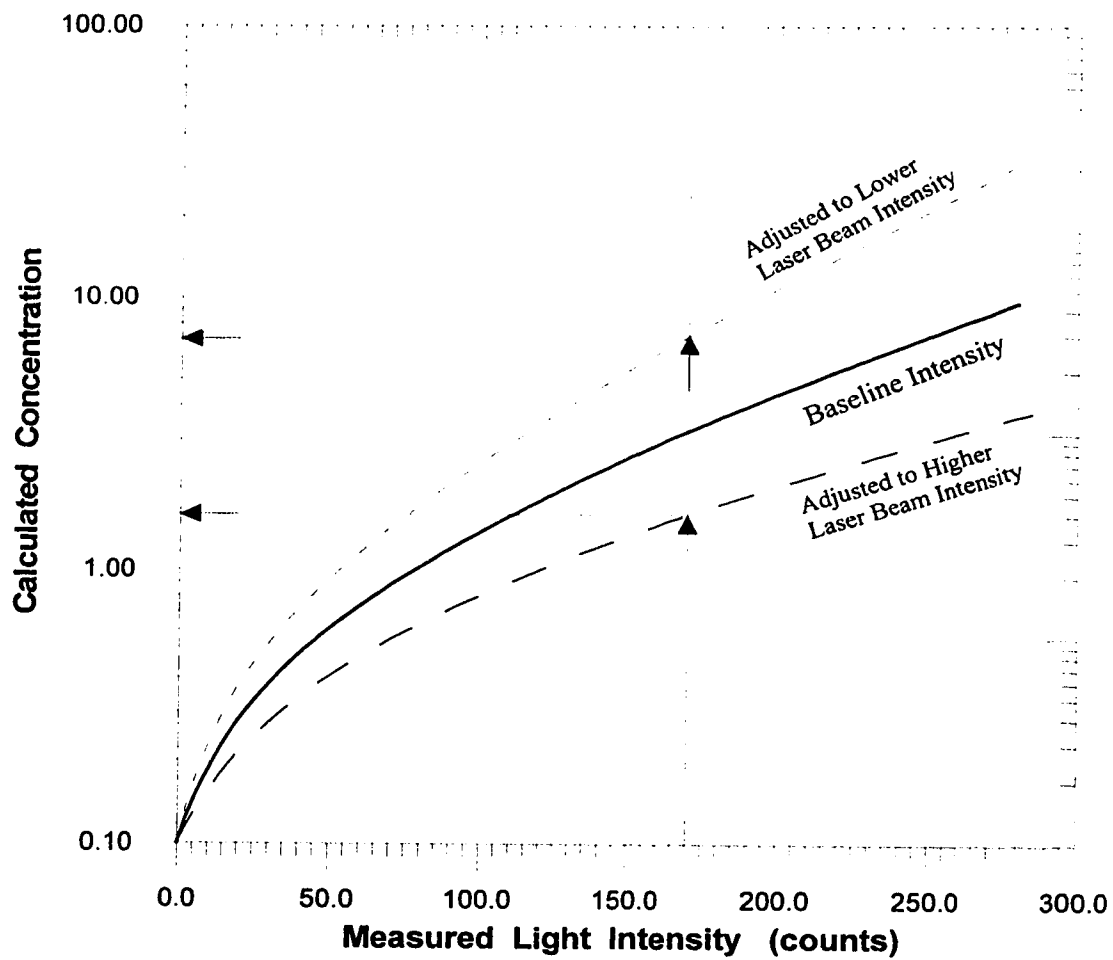


Figure 2.22 Adjustment of the calibration curve according to laser light intensity to day-to-day variations

the intensity axis, using the ratio of the initial bottle intensities.

This ratio was taken as the ratio between the value predicted from the standard calibration curve and newly measured value taken with a known concentration bottle at the time of data collection runs. If this intensity ratio was greater than 1.0, the initial laser intensity at the time of testing was greater than the standard value so the calibration curve was shifted forward shown as the dashed line in Figure 2.22. The calibration curve was shifted backward as the dotted line shown in Figure 2.22 if the intensity ratio was less than 1.0. Therefore, the constants in Equations (2.8) and (2.9) changed slightly from day to day based on the initial laser intensity calibration. Samples of the corrected and uncorrected concentration profiles using known concentration bottles and experimental runs are shown in Figures 2.23 and 2.24.

2.7 Full-Field Images Using PLIF

Full-field light sheet images were used to visualize the dispersion of neutrally buoyant material in the near and far wake region of a building, and to measure plume cross stream and vertical concentrations and spreads.

The water channel was illuminated by dual laser light sheets as shown in Figure 2.25. The laser used was a Coherent Innova 70, 4W argon-ion continuous wave laser that produced multi-wavelength laser light ranging from 488nm to 514.5nm (blue-green). Two laser sheets approximately 2mm thick were generated from the single laser beam. The details are discussed in Appendix B. Because the bottom of the water channel was covered by the surface roughness plate, the only way to view the test section was from top of the channel. A mirror, with dimensions of 500mm wide \times 1000mm long angled at 45° towards the video camera was used to view the test section. To decrease the water surface reflection caused by the surface waves, a piece of Styrofoam was floated on the water

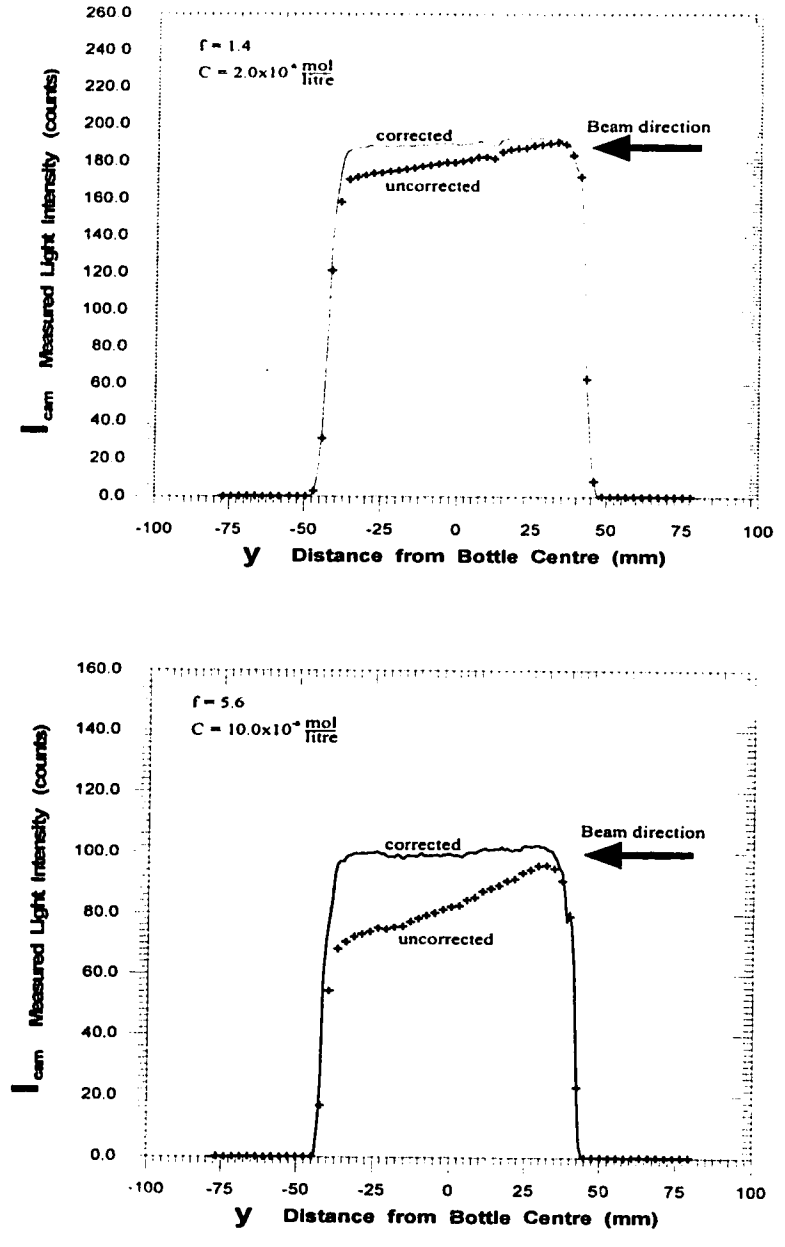
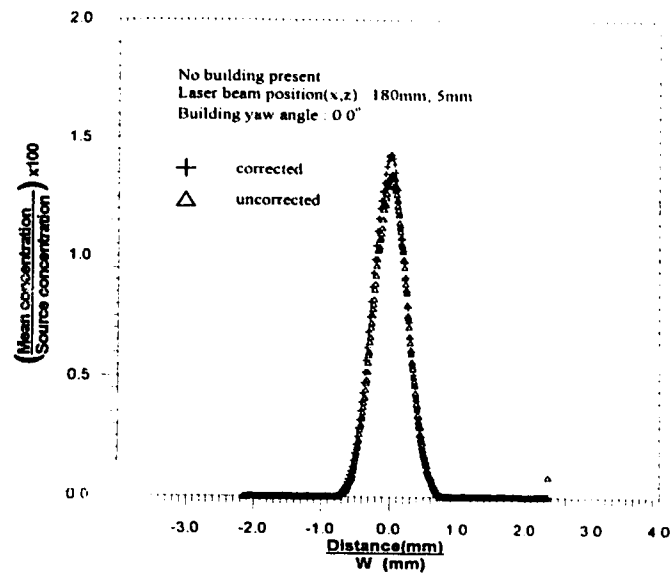
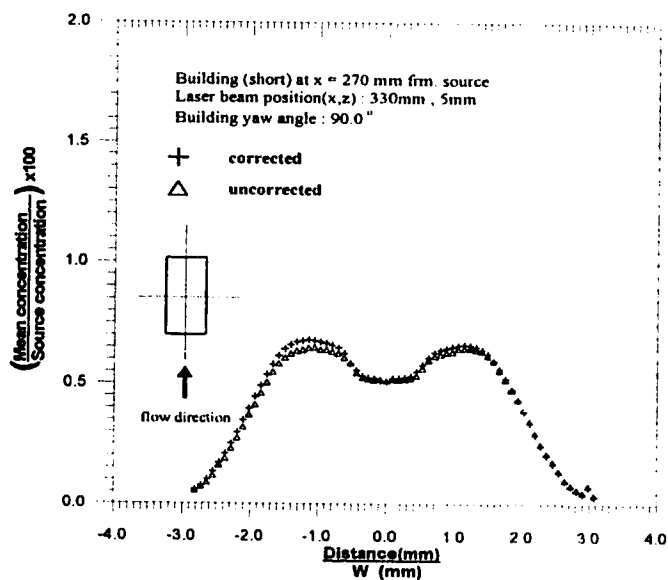


Figure 2.23 Attenuation correction test against the known concentration bottles

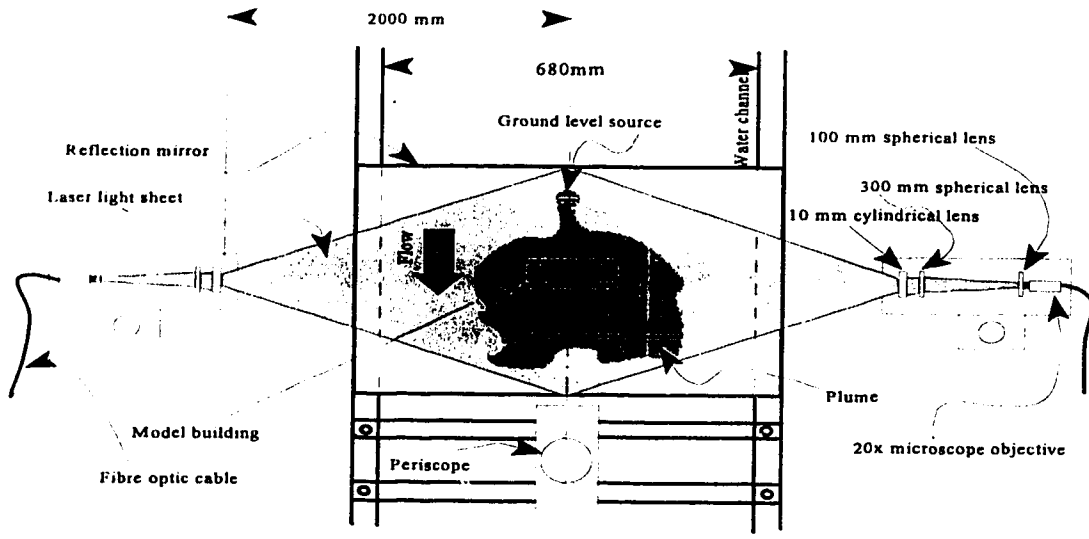


(a) Plume only

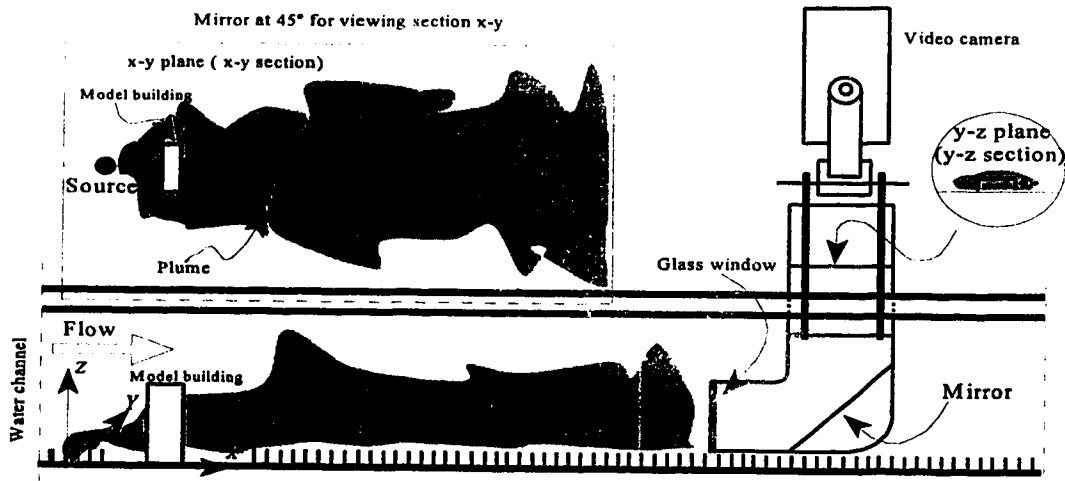


(b) Building A with yaw angle 90°

Figure 2.24 Samples of corrected and uncorrected (linescan) plume concentration profiles with and without a building present (building A at yaw angle 90° and dimensions: 100mm wide \times 50mm high \times 40mm long)



(a) Viewing the horizontal/x-y plane



(b) Viewing the vertical/y-z plane

Figure 2.25 Schematic diagram of visualizing the building in two planes

surface upstream to act as a wave suppressor. The laser sheet usually passed through the water channel horizontally, but could also be turned vertically so both the x-y and y-z plane could be illuminated. Even though there was no need to correct the light sheet attenuations on the full-field images obtained by using PLIF method (Campbell, 1991), other corrections had to be made for the background concentration, the building shadows, and the light sheet edge effects. The background concentration was caused by a buildup of the fluorescent dye concentration in the water channel. The shadows from the building edges were caused by the different refraction indices of the channel water and the plexiglass used to construct the model buildings. The intensity across the laser light sheets was a Gaussian distribution, so at the edges of the light sheets the light was dimmer. Air bubbles and other small particles in the water scattered the laser light. To cope with these problems, a 9×9 spatial averaging filter was found to be the best to smooth the irregularities in the collected full-field images, see Appendix B for details of the spatial filtering.

2.7.1 Image Collection

The same image system (Figure 2.18) used for the linescan was used to collect the full-field images. The steps used were:

- Calibrating laser output using a known concentration bottle.
- Taking 50 frames as the background intensity before each run of experiment.
- Turning on the ground-level source.
- Collecting plume images for 300 seconds at the rate of 8 frames per second.
- Turning off the ground-level source.
- Taking 50 frames at the end of each run.
- Adding small amount of concentrated dye solution to the channel for obtaining a sheet image (a 50 frame average image) which was used as the intensity map to correct the background and plume images.

2.7.2 Image Corrections

The steps used in this correction process were:

- Filtering the time averaged sheet image using the 9×9 lowpass digital filter and at the same time applying an empirical constant to correct the light sheet edge effects. The filtered sheet image was then normalized by the intensity (10×10 pixel average) measured at the same location where the single-bottle initial calibration was carried out.
- Filtering the two background images and the plume images using the 9×9 lowpass filter and also correcting for laser sheet edge effects.
- Normalizing the filtered background and plume images using the corrected sheet image.
- Converting the corrected background and plume intensity images into concentrations.
- Subtracting the average background concentration image, obtained by averaging the two background concentrations (at the beginning and end of each run), from the plume concentration image.

See Appendix B for details on the full-field image collection, corrections and derivation of correction equations. Some example of the corrected full-field concentration images are shown in Figure 2.26.

Chapter 3

Plume Spread with Downwind Buildings

3.1 Introduction

Dispersion near a building is greatly influenced by the flow field. This is determined by the shape and orientation of the buildings and the upstream condition. Due to the greater crosswind and vertical spreading of a plume behind a building, the standard Gaussian plume model makes serious errors in predicting concentrations.

The first simple theoretical model dealing with plume dispersion under the influence of a building was proposed by Gifford (1960). Gifford allowed for greater initial plume dilution at buildings by adding a term proportional the building projected area A_p to the Gaussian dispersion model for the plume centre line ground level concentration downstream of the building,

$$C_o = \frac{Q}{(\pi \sigma_y \sigma_z + kA_p) U_c} \quad (3.1)$$

In Equation (3.1) the constant k is an empirical number estimated to be in the range $0.5 < k < 2.0$.

Turner (1969) and Barker's (1982) virtual source models match the plume from a virtual upstream source with the experimental observations of the greater dilution in the near wake region. In these virtual source models, the plume crosswind and vertical spread at the rear face of a building are specified as fraction of the building height and width by choosing the virtual source position. In Turner's model, the crosswind and vertical spreads are defined as $\sigma'_y = W/3$, and $\sigma'_z = H/2.15$. In Barkers model, $\sigma'_y = W/4.3$ and $\sigma'_z = H/3.0$.

The Ferra and Cagnetti (1980) model was developed by applying the concept introduced by Halitsky (1977) of using the dimensions of an equivalent flat plate to a building. Some quantities which were linearly proportional to the plate size were added to the plume crosswind and vertical spreads downwind of a building to produce higher wake dispersion.

$$\begin{aligned}\sigma'_y &= \sigma_y + \frac{W}{2.507} \\ \sigma'_z &= \sigma_z + \frac{H}{2.507}\end{aligned}\quad (3.2)$$

where W and H are the building upwind face width and height.

The Huber and Snyder (1982) model, based on their wind tunnel studies, is more complicated than other models. It is divided into near-wake, far-wake and recirculation regions. In the near-wake region, defined as $3H \leq x \leq 10H$, where x is measured from the building rear face and H is the building height, the plume crosswind and vertical spread are specified as:

$$\begin{aligned}\sigma'_y &= 0.7H + \frac{(x - 3H)}{15} \\ \sigma'_z &= 0.7H + \frac{(x - 3H)}{15}\end{aligned}\quad (3.3)$$

The far-wake region is defined as $x > 10H$. The virtual model is chosen so that the plume spreads match with the values predicted from the near-wake model at $x = 10H$. But, if the plume spreads predicted by the model are less than the undisturbed flow, then the virtual source model should be used. If the source height is above H (the building height), only the vertical spread is enhanced and the crosswind spread is not affected. Note that the Huber and Snyder (1982) model assumes a constant concentration in recirculating region downwind of a building, where $x < 3H$, and this constant concentration could be estimated using the Equation (3.3) by setting $x = 3H$.

All of these models are basically the same in their treatment of the building influence by adding larger initial plume spreads related to building size to the standard Gaussian model. In this thesis, the objective is to develop a model that can be used to predict the plume concentration either upwind or downwind of a building using a concept similar to the above models.

3.2 Concentration Predictions Using Gaussian Plume Models

Since the plume spreads modelled in this thesis use the Gaussian plume concept, it is necessary to briefly describe its formulation

If the mass release rate Q of the source is varying slowly with time or is a steady release, along-wind diffusion can be neglected, and the plume concentration with wind speed U_c is given by the reflected Gaussian profile (Csanady, 1973),

$$C = \frac{Q}{(2\pi)U_c\sigma_y\sigma_z} \exp\left(\frac{-y^2}{2\sigma_y^2}\right) \left[\exp\left(\frac{-(z-h_s)^2}{2\sigma_z^2}\right) + \exp\left(\frac{-(z+h_s)^2}{2\sigma_z^2}\right) \right] \quad (3.4)$$

This implies homogeneous turbulence, and neglects the change in vertical eddy diffusivity with height above the ground. So the ground level concentration of the plume can be found by setting $z = 0$ in Equation (3.4),

$$C_0 = \frac{Q}{\pi\sigma_y\sigma_zU_c} \exp\left(\frac{-y^2}{2\sigma_y^2}\right) \exp\left(\frac{-h_s^2}{2\sigma_z^2}\right) \quad (3.5)$$

where the downwind distance x enters Equation (3.5) through the variation of σ_y and σ_z .

3.3 Extending the Gaussian Plume Model to the Current Studies

The main interest in the current study is to develop a simple model which can be used to

predict the concentration of a neutrally buoyant plume released from a ground level point source upstream of buildings. Experimental methods such as laser linescan and PLIF were used to investigate plume dispersion either in the near wake region or upwind of buildings. The flow in the vicinity of buildings is greatly disturbed and its pattern becomes very complicated and extremely hard to trace due to the interactions among different flow regions and vortices. Therefore, to simplify this complicated problem, the following assumptions were made in the proposed model:

- the mean flow is neutrally stratified stable flow;
- the contaminant released, for the present study, is neutrally buoyant, highly concentrated fluorescein dye solution;
- the source is considered as a point source and its flow rate is steady;
- the along-wind plume spread σ_x is small comparing with the along-wind distance travelled by a fluid parcel in the same time interval, Δt .

3.3.1 Developing the Plume Model Using Gaussian Plume Concept

The Gaussian plume is used as the stepping-stone towards the complex problem of plume dispersion and dilution around buildings. The additional plume dispersion due to the presence of a building is assumed to be caused solely by the change of plume crosswind and vertical spreads, σ_y and σ_z , and neglects changes in convective windspeed U_c . The plume maximum concentration, even under the influence of buildings, retains the similar form of the Equation (3.5), with $h_s = 0$ and $y = y_c$,

$$C_0 = \frac{Q}{\pi U_c \sigma_y \sigma_z} \quad (3.6)$$

The maximum mean concentration ratio of the plume at ground level with and without a building will be:

$$\frac{C_{wi}}{C_{wo}} = \frac{\left(\frac{Q}{\pi U_{wi} \sigma_{y,wi} \sigma_{z,wi}} \right)}{\left(\frac{Q}{\pi U_{wo} \sigma_{y,wo} \sigma_{z,wo}} \right)} \quad (3.7)$$

$$= \left(\frac{U_{wo}}{U_{wi}} \right) \left(\frac{\sigma_{y,wo}}{\sigma_{y,wi}} \right) \left(\frac{\sigma_{z,wo}}{\sigma_{z,wi}} \right)$$

if a plume develops without a building, its vertical spread will be proportional to its crosswind spread, so it might be reasonable to assume:

$$\frac{\sigma_{z,wo}}{\sigma_{z,wi}} = \left(\frac{\sigma_{y,wo}}{\sigma_{y,wi}} \right)^a \quad (3.8)$$

Equation (3.7) will become:

$$\frac{C_{wi}}{C_{wo}} = \left(\frac{U_{wo}}{U_{wi}} \right) \left(\frac{\sigma_{y,wo}}{\sigma_{y,wi}} \right) \left(\frac{\sigma_{y,wo}}{\sigma_{y,wi}} \right)^a \quad (3.9)$$

$$= \left(\frac{U_{wo}}{U_{wi}} \right) \left(\frac{\sigma_{y,wo}}{\sigma_{y,wi}} \right)^{(1+a)}$$

As Figure 3.1 shows, for a diverging plume, the principle of conservation of mass leads to:

$$\sigma_{y_1} U_1 \sigma_{z_1} = \sigma_{y_2} U_2 \sigma_{z_2} \quad (3.10)$$

and Equation (3.10) can be rewritten as:

$$\frac{U_2}{U_1} = \left(\frac{\sigma_{y_1}}{\sigma_{y_2}} \right) \left(\frac{\sigma_{z_1}}{\sigma_{z_2}} \right) \quad (3.11)$$

Equation (3.11) indicates that the change in velocity U as the plume approaches a building is linked to changes in plume spreads σ_y and σ_z , since both the plume spread and velocity are the result of diverging streamlines due to deceleration of the flow. To express the ratio of velocities in Equation (3.11) in terms of plume dimensions, assume an empirical relation of the form,

$$\frac{U_{wo}}{U_{wi}} = \left[\left(\frac{\sigma_{y,wi}}{\sigma_{y,wo}} \right) \left(\frac{\sigma_{z,wi}}{\sigma_{z,wo}} \right) \right]^b \quad (3.12)$$

where the exponent b is an empirical constant. Note that Equation (3.9) relates the velocities of two different plumes at the same x location, but Equation (3.10) links the velocities of a single plume at two different x locations. Equation (3.11) is an empirical

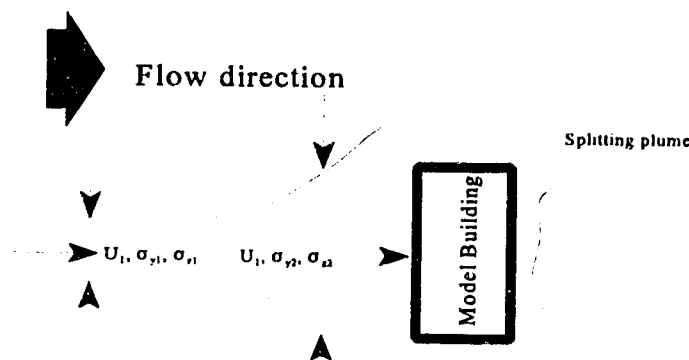


Figure 3.1 Schematic diagram showing the crosswind spread of a plume

rather than an exact relation of plume velocities with and without a building present.

Applying Equation (3.8) to Equation (3.12),

$$\begin{aligned} \frac{U_{wo}}{U_{wi}} &= \left[\left(\frac{\sigma_{y,wi}}{\sigma_{y,wo}} \right) \left(\frac{\sigma_{y,wi}}{\sigma_{y,wo}} \right)^a \right]^b \\ &= \left(\frac{\sigma_{y,wi}}{\sigma_{y,wo}} \right)^{b(1+a)} \end{aligned} \quad (3.13)$$

Finally, combining Equation (3.9) and (3.13),

$$\frac{C_{wi}}{C_{wo}} = \left(\frac{\sigma_{y,wi}}{\sigma_{y,wo}} \right)^{(1+a)(1-b)} \quad (3.14)$$

In the case when value of $b = 1.0$, the increase of the plume spreads, σ_y and σ_z , caused by the diverging streamlines is exactly balanced by the decrease of the plume velocity U_c as the flow decelerates while approaching the building. This limiting case produces no change in plume concentration resulting from introducing a building into a plume.

In order to use the Equation (3.14) to predict the effect of a building, the ratio of $(\sigma_{y,wi}/\sigma_{y,wo})$ must be determined using experimental data. To determine the empirical function, a new coordinate system is defined as shown in the Figure 2.2.

To take the building effects into account for the disturbed flow around buildings, a length scale R proposed by Wilson (1979) which $R = L^{1/3}S^{2/3}$ where L and S are defined as the largest and smallest dimensions of upwind building face, is used to normalize all distances and plume spreads. Other length scales were also tested, such as $R = L^{1/4}S^{3/4}$ and $R = L^{1/2}S^{1/2}$. Based on the experimental data obtained in the present experiment they are shown in Figure 3.2 and 3.3 where we see that the choice of exponents for L and S makes little difference for the present case. The building length scale defined by Wilson (1979) was chosen because it was developed over larger range of building dimensions.

3.3.2 Determining the Plume Spreads

As mentioned above, the ratio of $\sigma_{y,wo}/\sigma_{y,w}$ is determined using experimental data. The plume concentration across the stream was used to determine the plume centre (y_c) from its first moment.

$$y_c = \frac{\int_{-\infty}^{+\infty} y C(y) dy}{\int_{-\infty}^{+\infty} C(y) dy} \quad (3.15)$$

If the centre of the plume at a specified x location is known, its crosswind spread σ_y is the second spatial moment of the plume cross stream concentration.

$$\sigma_y^2 = \frac{\int_{-\infty}^{+\infty} (y - y_c)^2 C(y) dy}{\int_{-\infty}^{+\infty} C(y) dy} \quad (3.16)$$

Using Equations (3.15) and (3.16), the plume crosswind spread can be found at any streamwise location.

I. Finding $\sigma_{y,wo}$

$\sigma_{y,wo}$ is determined first because it is easier to find and express as a function of the along-wind distance (x) from the source. Making use of the Equations (3.15) and (3.16), $\sigma_{y,wo}$ was calculated from concentration images such as one shown in the Figure 3.4(a), and fitted using a power function,

$$\sigma_{y,wo}^2 = \sigma_{y,wo,0}^2 + 2.06 x^{1.07} \quad (3.17)$$

with $\sigma_{y,wo,0} = 4.47$ mm and x in mm. As shown in the Figure 3.4(b), Equation (3.17) fits the experimental data quite well. From Equation (3.17), $\sigma_{y,wo} \propto x^{0.54}$, the exponent 0.54 is a bit smaller than expected value which is about 0.55 (Griffiths, 1991). This might be

caused by the narrow width of the water channel that has effects on the turbulence scale at the test section. This fitted function is used in all the calculations in this thesis to find the ratio $\sigma_{y,ww}/\sigma_{y,wi}$.

II. Finding $\sigma_{y,wi}$

There is no simple way to fit $\sigma_{y,wi}$ through a simple function like the one used for $\sigma_{y,wo}$. The building has profound effects on the plume as it approaches the building. Two selected concentration images are shown in Figure 3.5. The experimental data from each individual concentration image were retrieved and used to determine $\sigma_{y,wi}$ in the cross-wind (y) direction at specified streamwise, x locations using Equations (3.15) and (3.16). Selected examples of plume crosswind spread with a building present when comparing with no building present are shown in Figures 3.6, 3.7, 3.8 and 3.9.

III. Finding $\sigma_{z,wo}$

When determining the plume vertical spread, $\sigma_{z,wo}$, data gathered at only four x locations were available for examination. Direct calculations were made with Equations (3.15) and (3.16) on plume concentration images obtained by turning the dual laser sheet in its vertical position. The image from one of the four locations is shown in Figure 3.10(a).

An independent calculation of $\sigma_{z,wo}$ was made by fitting a Gaussian profile to vertical profiles of concentration on the plume centerline ($y = 0$) using both linescan data and values from full-field images. Equation (3.4) for a ground level source with the sheet at height z ($z = 5\text{mm}$) was used,

$$C = \frac{Q}{\pi \sigma_y \sigma_z U_c} \exp\left(\frac{-z^2}{2 \sigma_z^2}\right) \quad (3.18)$$

Since at a specified x location, U_c , σ_y , σ_z are constants, then the Equation (3.18) can be further simplified,

$$C = C_0 \exp\left(-\frac{z^2}{2\sigma_z^2}\right) \quad (3.19)$$

From the experimental data using both full-field images and linescan profiles, Figures 3.10(b), 3.10(c), and 3.11, show that the plume vertical spread $\sigma_{z,w}$ can be fitted using a power function,

$$\sigma_{z,w}^2 = \sigma_{z,o}^2 + 1.25 x^{1.05} \quad (3.20)$$

with $\sigma_{z,o} = 5.0$ and x in mm.

3.3.3 Verifying the Gaussian Model Using Full-field Images

Applying the experimentally determined functions of $\sigma_{y,w}$ and $\sigma_{z,w}$ from Equations (3.17) and (3.20) respectively to the Gaussian model for centerline ground-level concentration of a ground-level source plume to compare with the concentration at the centerline from a plume image shown in Figure 3.12,

$$\begin{aligned} C_0 &= \frac{Q}{\pi U_c \sigma_y \sigma_z} \\ &= \frac{Q}{\pi U_c \left(\sigma_{y,w,o,0}^2 + 2.06 x^{1.07}\right)^{\frac{1}{2}} \left(\sigma_{z,w,o,0}^2 + 1.25 x^{1.05}\right)^{\frac{1}{2}}} \end{aligned} \quad (3.21)$$

with $\sigma_{y,w,o,0} = 5.0$, $\sigma_{z,w,o,0} = 4.47$ and U_c is a constant which was calculated at $z = 5$ mm the laser sheet height. The theoretical prediction and the experimental measurement showed a good agreement (shown in Figure 3.12). The small amount of concentration offset from the predicted values possibly was caused by the concentration calibration offset from calibration curves (see Figures 2.21, 2.22 and B-4).

3.3.4 Normalizing the Plume Spread Difference ($\sigma_{y,wi} - \sigma_{y,wo}$)

The experimental data suggested that there might be a function which could be used to describe the plume crosswind spread with the presence of buildings. After plotting up the data in several normalized forms, the function ϕ which was most successful in correlating the change in σ_y with a building presence was:

$$\phi\left(\frac{x'}{R}\right) = \left(\frac{\sigma_{y,wi} - \sigma_{y,wo}}{R}\right) \left(\frac{(\sigma_{y,wo})_{at x'=0}}{R}\right)^{0.5} \quad (3.22)$$

with function $\phi(x'/R)$ in Equation (3.22) represented empirically as a gradual increase approaching the building front face, followed by a constant added plume width downwind from the building front face, see Figures 3.13 and 3.14. The approximate straight line behaviour of the function $\phi(x'/R)$ upwind of building on the semi-log plots of Figures 3.2 and 3.3 suggests an exponential function. The fitted functions shown are:

downwind of the building front face,

$$\phi\left(\frac{x'}{R}\right) = 0.45 \quad \text{for } \frac{x'}{R} > 0 \quad (3.23)$$

upwind of the building front face,

$$\phi\left(\frac{x'}{R}\right) = 0.45 \exp\left(\frac{1}{0.8} \frac{x'}{R}\right) \quad \text{for } \frac{x'}{R} < 0 \quad (3.24)$$

3.3.5 Combining the Related Equations to Predict the Concentration Ratio

After making assumptions on plume crosswind and vertical spreads and their relations and developing an equation for the normalized plume crosswind spreads for the plume in the case when building is present and absent, all the related equations can be combined to derive the final explicit form for the concentration ratio stated as Equation (3.14). By

factoring out $\sigma_{y,wo}/R$ from Equation (3.22),

$$\phi\left(\frac{x^*}{R}\right) = \left(\frac{\sigma_{y,wo}}{R}\right) \left(\frac{\sigma_{y,wi}}{\sigma_{y,wo}} - 1\right) \left(\frac{(\sigma_{y,wo})_{at x^*=0}}{R}\right)^{0.5} \quad (3.25)$$

so, solving for the plume spread ratio $\sigma_{y,wi}/\sigma_{y,wo}$,

$$\frac{\sigma_{y,wi}}{\sigma_{y,wo}} = \phi\left(\frac{x^*}{R}\right) \left(\frac{R}{\sigma_{y,wo}}\right) \left(\frac{R}{(\sigma_{y,wo})_{at x^*=0}}\right)^{0.5} + 1 \quad (3.26)$$

and, the Equation (3.26) can be alternatively expressed as,

$$\frac{\sigma_{y,wo}}{\sigma_{y,wi}} = \frac{1}{1.0 + \phi\left(\frac{x^*}{R}\right) \left(\frac{R}{\sigma_{y,wo}}\right) \left(\frac{R}{(\sigma_{y,wo})_{at x^*=0}}\right)^{0.5}} \quad (3.27)$$

Finally, combining Equations (3.14) and (3.27),

$$\frac{C_{wi}}{C_{wo}} = \left[\frac{1}{1 + \phi\left(\frac{x^*}{R}\right) \left(\frac{R}{\sigma_{y,wo}}\right) \left(\frac{R}{(\sigma_{y,wo})_{at x^*=0}}\right)^{0.5}} \right]^{(1+a)(1-b)} \quad (3.28)$$

where ϕ is the empirical function defined as in the Equations (3.23) and (3.24). It was also found, based on the experiments, that Equation (3.28) best fit the experimental data with $(1+a)(1-b) = 1.5$. This will be shown in the next chapter.

Using this simple formula to predict the plume concentration when a building is present only requires the plume crosswind spread when there is no building. The building effects enter Equation (3.28) through the building length scale R , where

$$R = L \frac{1}{3} S \frac{2}{3} \quad (3.29)$$

with L equal to the larger of height H or width W , and S is equal to the smaller of the two. Equation (3.28) will be used to calculate the predicted plume concentration, and the predicted concentration values at the same x locations will be compared with the experimental data collected for the present studies in later chapters.

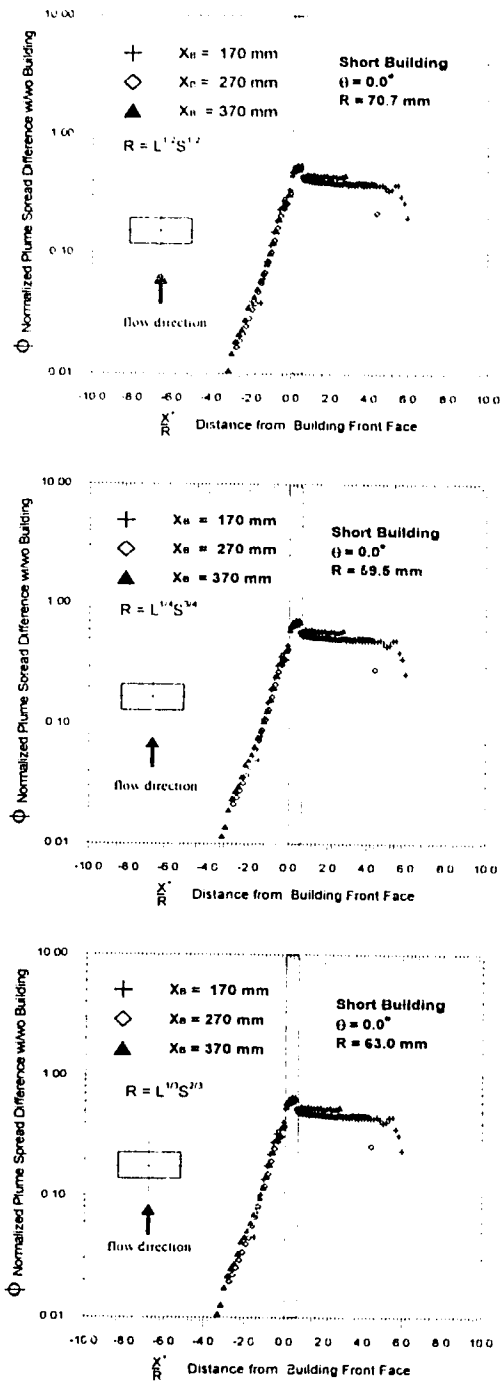


Figure 3.2 Comparison of using different building length scales on building A at 0° yaw angle (building dimensions: 100mm wide \times 50mm high \times 40mm long)

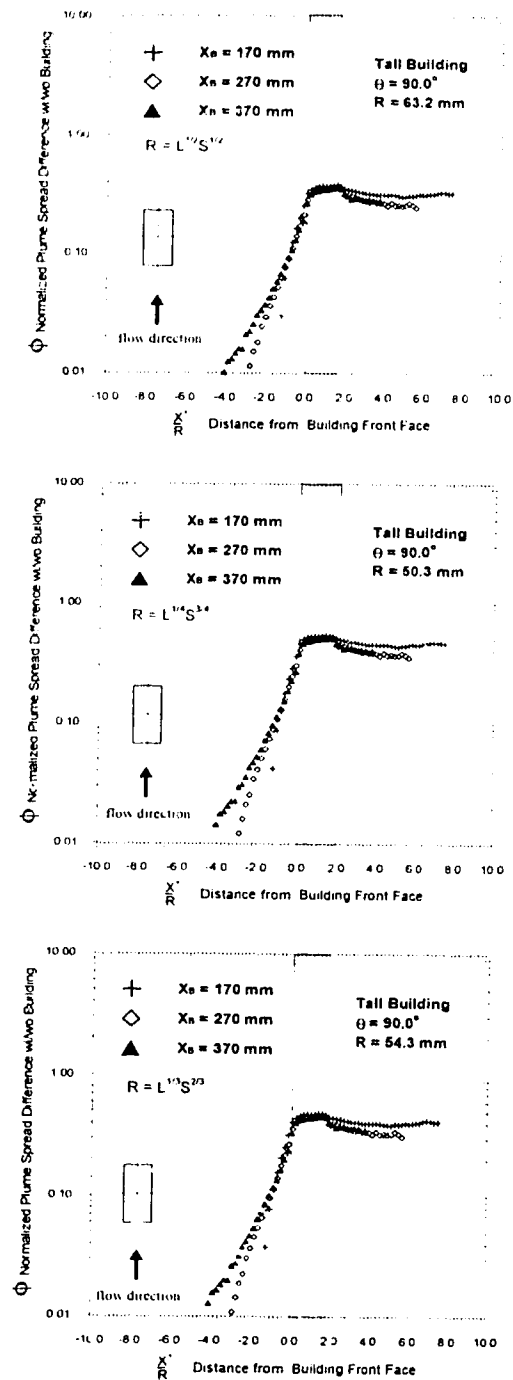
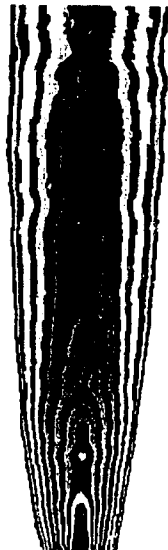


Figure 3.3 Comparison of using different building length scales on building B at 90° yaw angle (building dimensions: 100m wide \times 100mm high \times 40mm long)



(a) Plume image

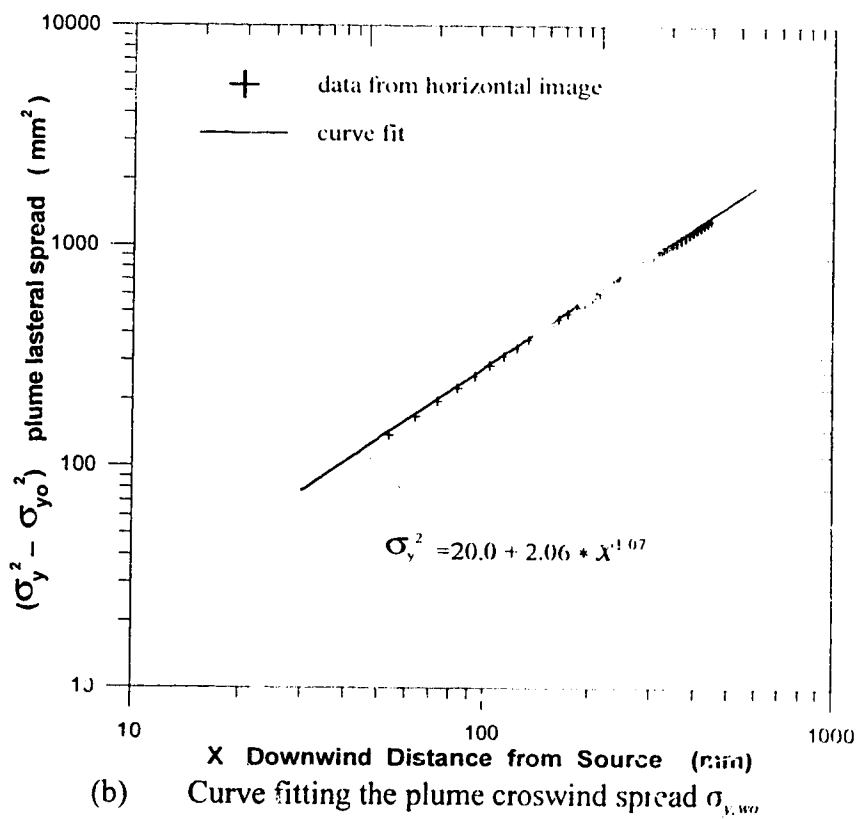


Figure 3.4 Plume concentration image and its crosswind spread obtained from the experimental data

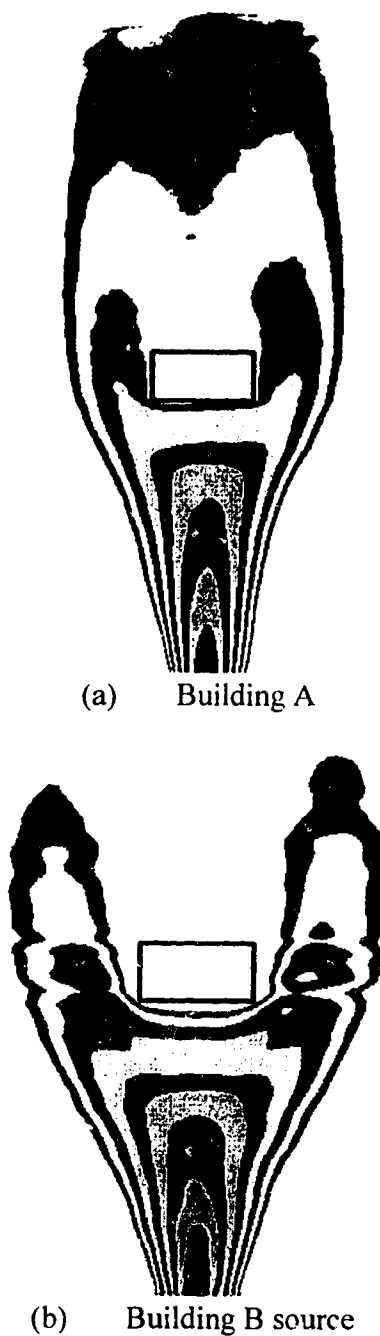


Figure 3.5 Two selected concentration images from present experiment for buildings at 270.0 mm from source and 0° yaw angle (dimensions of buildings: *A*, 100mm wide \times 50mm high \times 40mm long; *B*, 100mm wide \times 100mm high \times 40mm long)

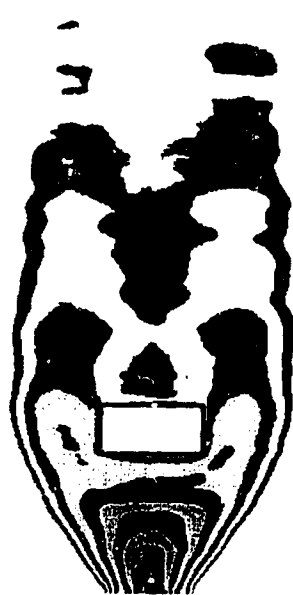
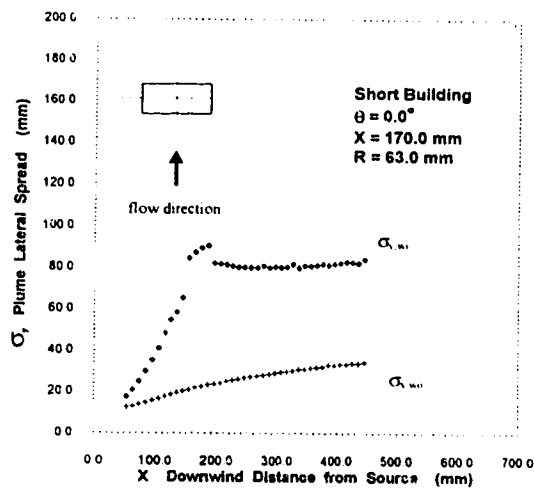
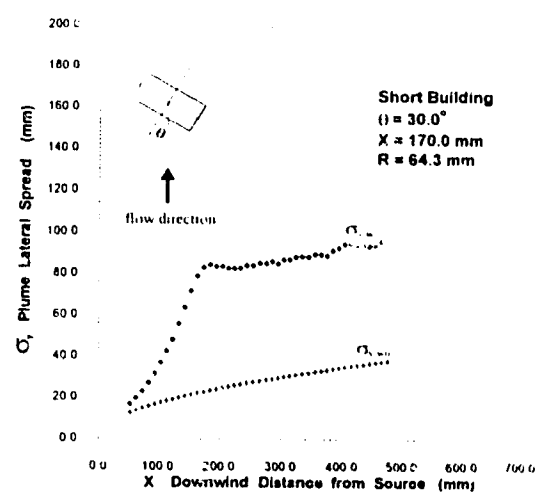
(a) Building *A* at 0°(b) Building *A* at 30°(c) Plume spreads for building *A* at 0°(d) Plume spreads for building *A* at 30°

Figure 3.6 Plume crosswind spreads, $\sigma_{y,w}$ and $\sigma_{y,w,w}$ for building *A* at x 170mm from source with yaw angle 0° and 30° (building *A* dimensions: 100mm wide \times 50mm height \times 40mm long)

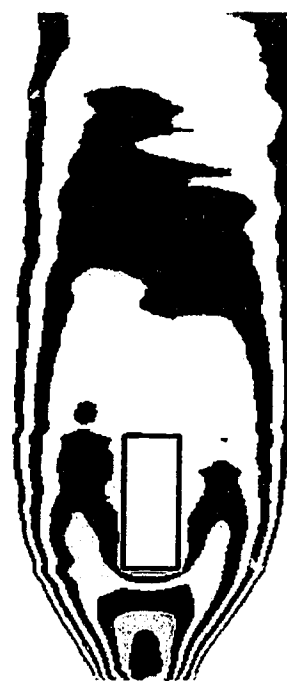
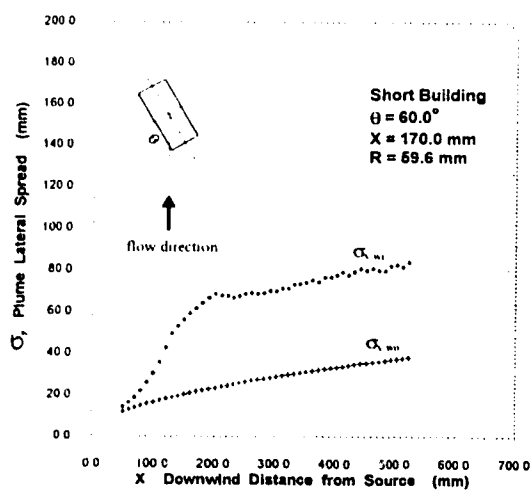
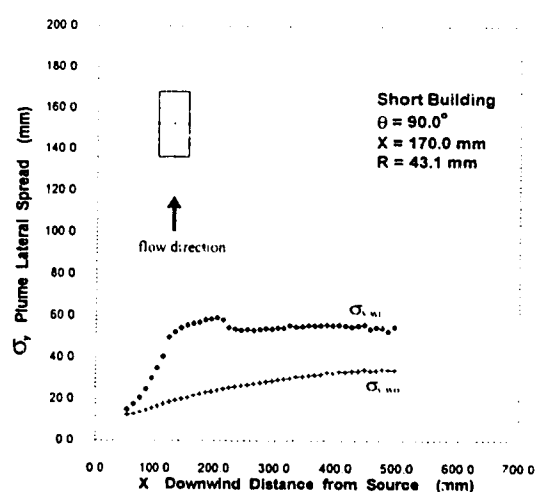
(a) Building *A* at 60°(b) Building *A* at 90°(c) Plume spreads for building *A* at 60°(d) Plume spreads for building *A* at 90°

Figure 3.7 Plume crosswind spreads, $\sigma_{y,w}$ and $\sigma_{y,m}$ for building *A* at $x = 170 \text{ mm}$ from source with yaw angle 60° and 90° (building *A* dimensions: 100mm wide \times 50mm height \times 40mm long)

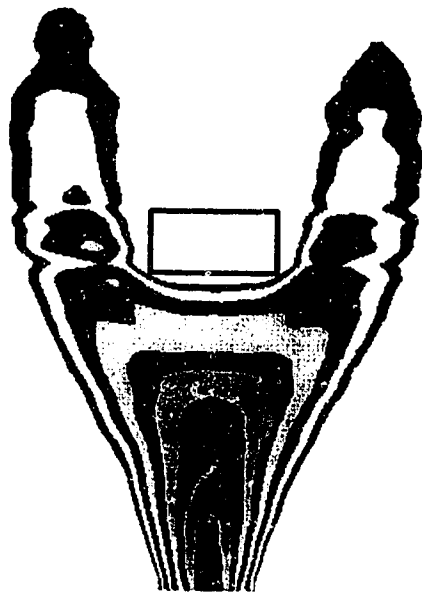
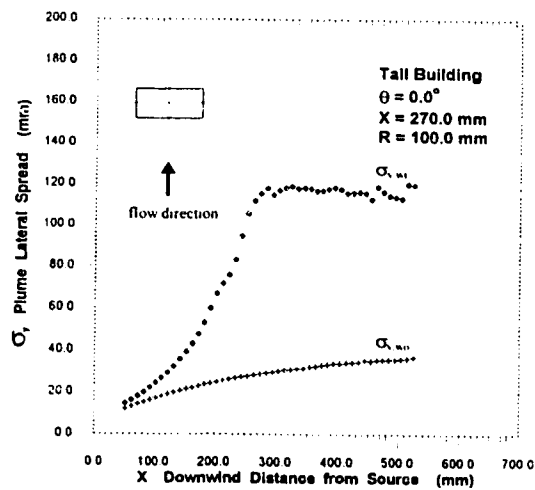
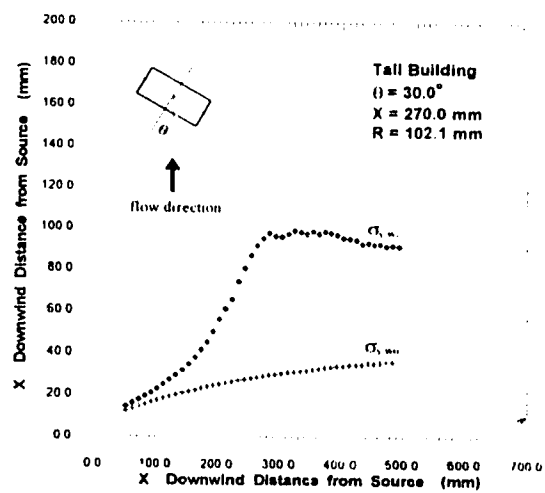
(a) Building *B* at 0°(b) Building *B* at 30°(c) Plume spreads for building *B* at 0°(d) Plume spreads for building *B* at 30°

Figure 3.8 Plume crosswind spreads, $\sigma_{y,w}$ and $\sigma_{y,d}$ for building *B* at $x = 270 \text{ mm}$ from source with yaw angle 0° and 30° (building *B* dimensions: 100mm wide \times 100mm height \times 40mm long)

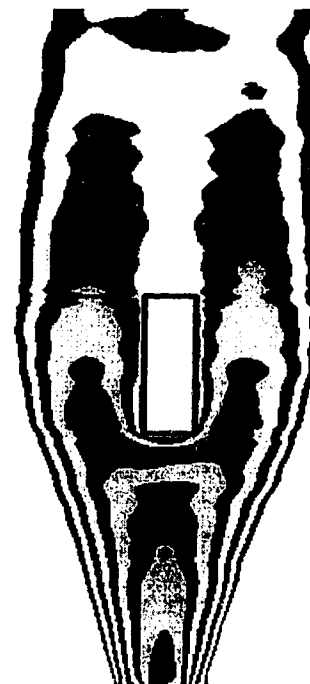
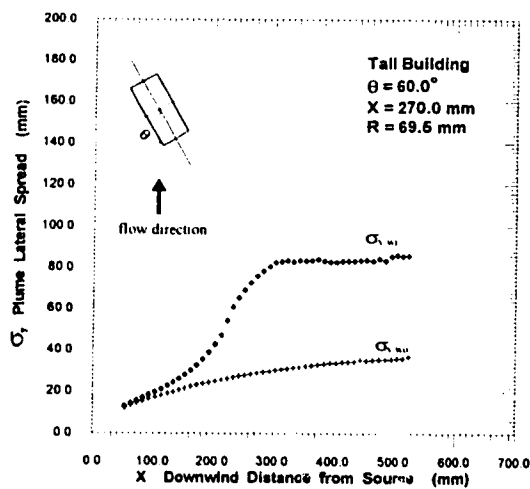
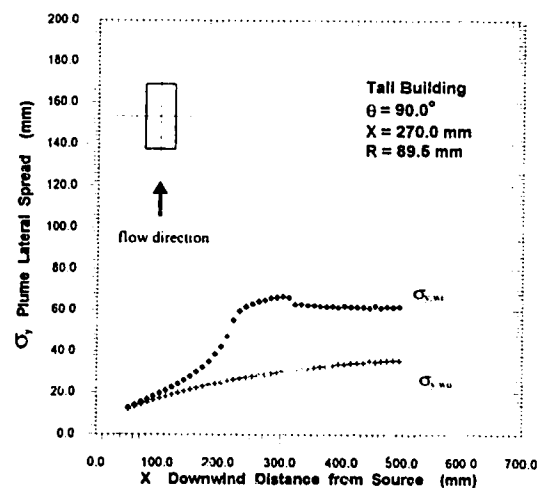
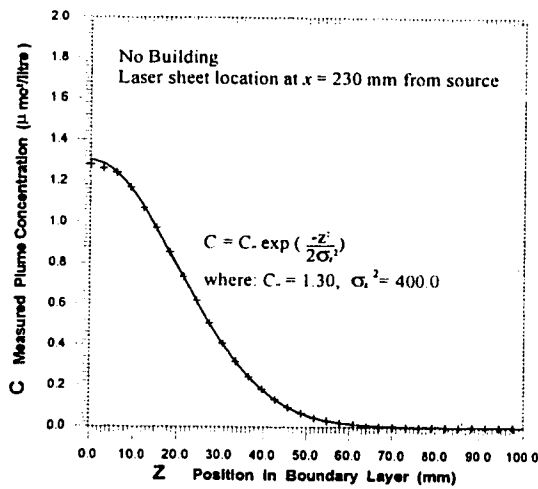
(a) Building *B* at 60°(b) Building *B* at 90°(c) Plume spreads for building *B* at 60°(d) Plume spreads for building *B* at 90°

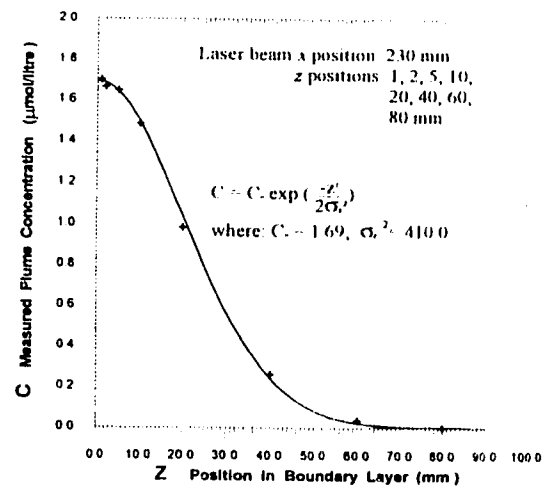
Figure 3.9 Plume crosswind spreads, $\sigma_{y,w}$ and $\sigma_{y,sw}$ for building *B* at $x = 270 \text{ mm}$ from source with yaw angle 60° and 90° (building *B* dimensions: 100mm wide \times 100mm height \times 40mm long)



(a) Looking upstream for plume (no building present) at $x = 170\text{mm}$ from source

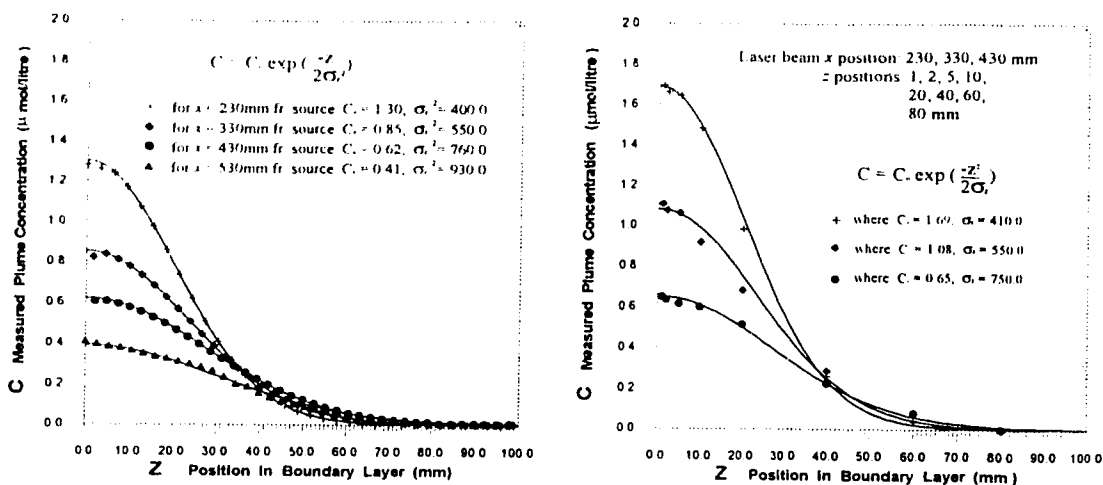


(b) Data from full-field image



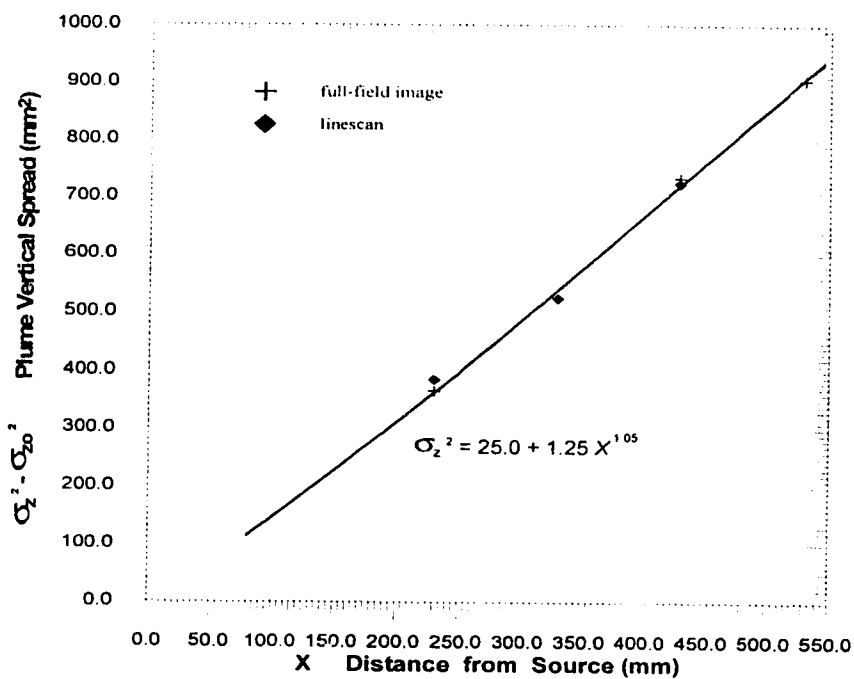
(c) Data from linescan measurement

Figure 3.10 Illustration showing the finding of $\sigma_{z,wr}$ at specified x location downwind from source (laser sheet and laser beam both at $x = 170\text{ mm}$)



(a) Data from full-field images at four x locations

(b) Data from linescan measurement at three x locations



(c) Fitting plume vertical spreads at different x locations from full-field and linescan measurements

Figure 3.11 Illustration showing curve fitting $\sigma_{z,ww}$, obtained from both full-filled and linescan measurement at specified $x = 230, 330, 430, 530$ mm downwind from source

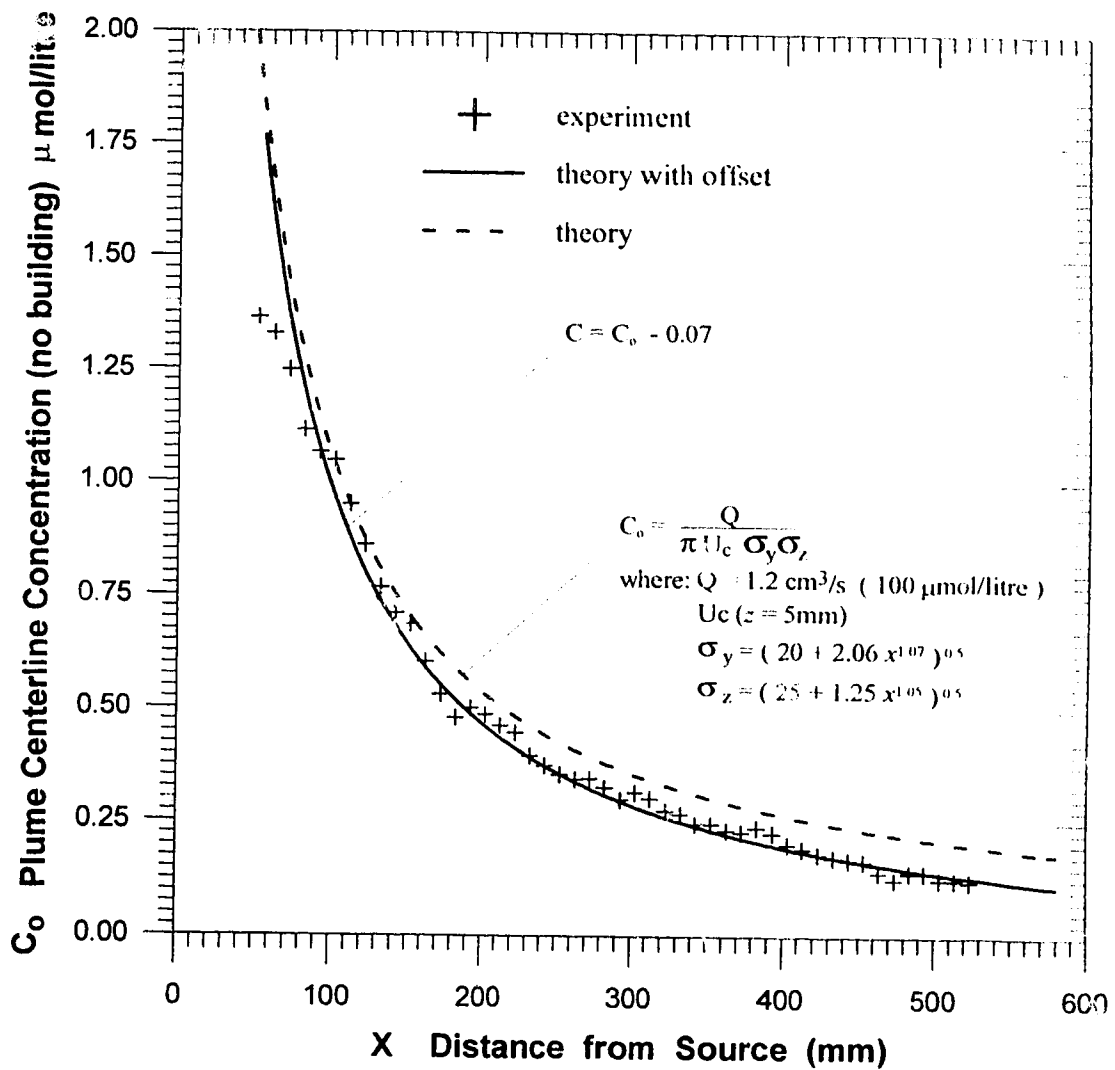


Figure 3.12 Verification of the Gaussian plume model using experimentally determined crosswind, vertical plume spreads and the windspeed at the laser sheet height

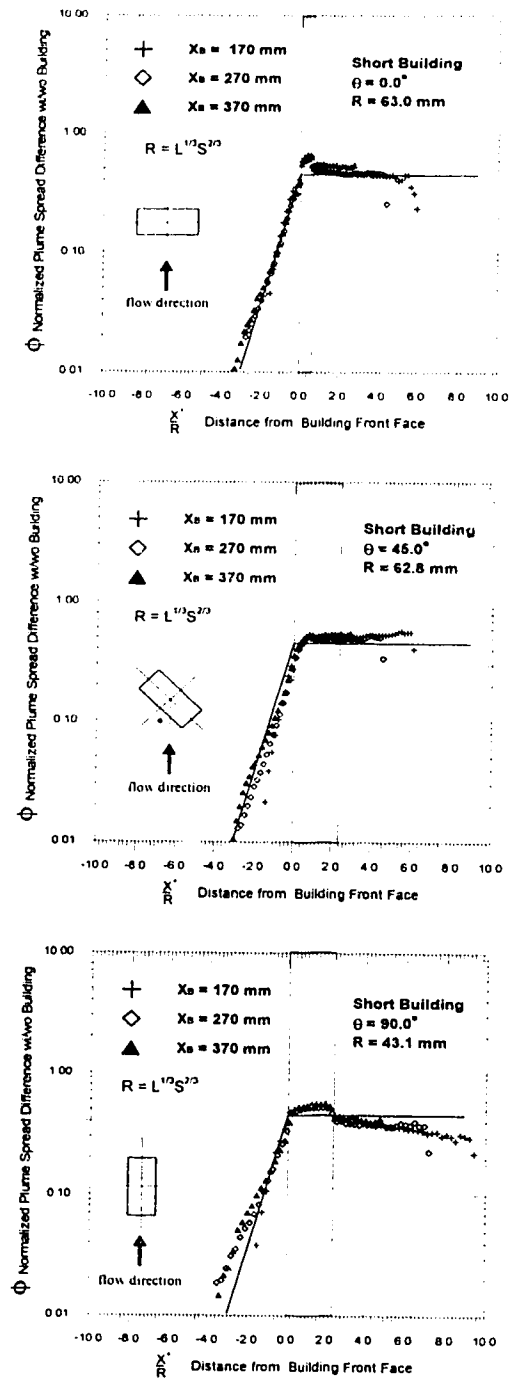


Figure 3.13 Applying $\phi(x^*/R)$ function to plume with building *A* at 0° , 45° and 90° yaw angle (building dimensions: 100mm wide \times 50mm high \times 40mm long)

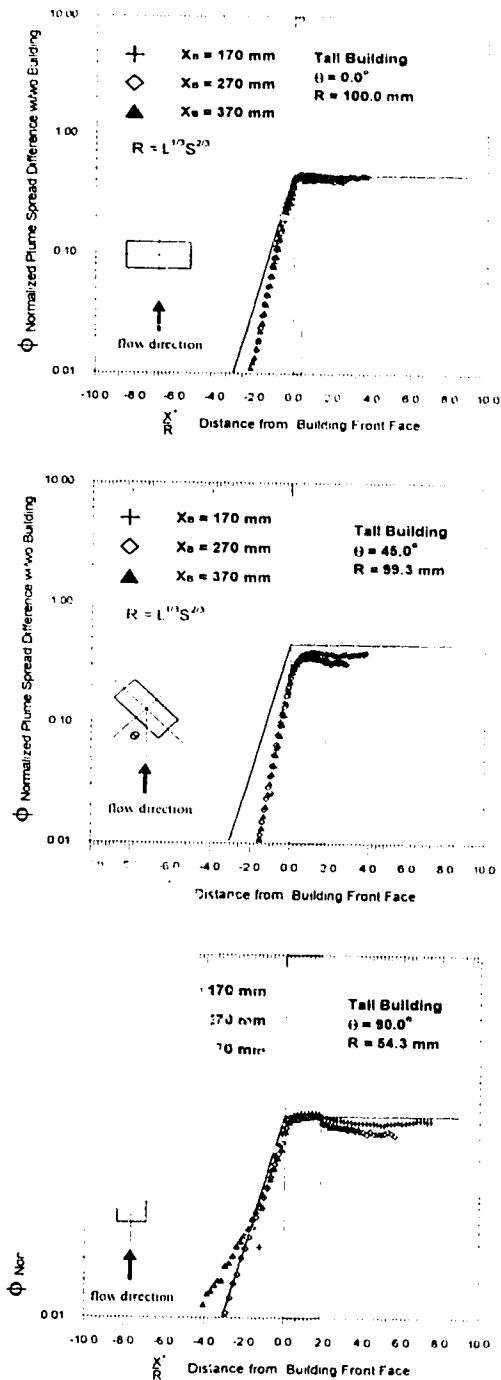


Figure 3.14 Applying $\phi(x'/R)$ function to plume with building B at 0° , 45° and 90° yaw angle (building dimensions: 100mm wide \times 100mm high \times 40mm long)

Chapter 4

Comparison of Plume Model to Experimental Data

4.1 Introduction

In this chapter, the newly developed plume model will be compared to the experimental data taken for this study from PLIF and linescan methods. The ability of this plume model to predict plume dilution from the neutrally buoyant ground level point source will be examined.

4.2 Plume Spread

The plume model is based on the experimental observation that the plume crosswind and vertical spread and dilution increased after encountering buildings. The plume experiences an increase in its size and a decrease of its concentration produced by the change of plume crosswind and vertical spread. As described in Chapter 3, the key assumptions in the development of this model are:

- the plume itself still behaves as the Gaussian single plume even after encountering buildings;
- the plume vertical spread can be related to the plume crosswind spread through a simple power function;
- velocity changes caused by the building presence could be related to the plume crosswind and vertical spreads through an empirical function.

Based on these assumptions, an equation for predicting plume concentration ratio of with to without a building present was derived as Equation (3.28). The value of $(1+a)(1-b) - 1.5$ is determined empirically later in this chapter from data collected using two model buildings at three locations, 170.0 mm, 270.0 mm and 370.0 mm from the source. Equation (3.28) gives,

$$\frac{C_{wi}}{C_{wo}} = \left[\frac{1}{1 + 0.45 \exp\left(\frac{1}{0.8} \frac{x^*}{R}\right) \left(\frac{R}{\sigma_{y,wo}}\right) \left(\frac{R}{(\sigma_{y,wo})_{at x^*=0}}\right)^{0.5}} \right]^{(1+a)(1-b)} \quad \text{for } \frac{x^*}{R} < 0 \quad (4.1)$$

and,

$$\frac{C_{wi}}{C_{wo}} = \left[\frac{1}{1 + 0.45 \left(\frac{R}{\sigma_{y,wo}}\right) \left(\frac{R}{(\sigma_{y,wo})_{at x^*=0}}\right)^{0.5}} \right]^{(1+a)(1-b)} \quad \text{for } \frac{x^*}{R} \geq 0 \quad (4.2)$$

Equations (4.1) and (4.2) are in reasonably good agreement with the experimental data, as it will be shown later with the experimental data that the empirically determined value of $(1+a)(1-b) = 1.5$ fits the data best.

4.3 Determination of the Plume Maximum Concentration from Full-field Images

In order to compare the concentration ratio (C_{wi}/C_{wo}) with the equations above, the experimental data from full-field concentration images were used. When a plume encounters a building the plume splits into two as shown in Figures 3.5 to 3.9. The ratio C_{wi}/C_{wo} in Equation (4.1) and (4.2) is defined as the plume local maximum at each x location, not at the centerline of the building. To determine this maximum concentration in a plume at specified x locations, the local maximum was selected. For a plume at x location the experimental concentration ratio C_{wi}/C_{wo} is calculated from the maximum concentrations with and without the building present. Due to the fact that the two concentration peaks at the sides of a building for building yaw angles of either 0° or 90° differ by less than ten percent the average of the two concentration peaks was used to determine C_{wi} . But for cases with building yaw angles between 0° and 90° , a single

maximum concentration value was used to determine the C_w , because the percentage difference of the concentration peaks at the sides of a building was much larger than ten percent. Therefore, for a plume at any x location the experimental concentration ratio (C_w/C_w) can be found as the division of the selected maximum concentration between plume with and without the building present. The local maxima of a plume will change from one side of a building to the other as the building yaw angle changes from 0° to 90° as Figures 4.2 to 4.6 demonstrate.

4.4 Plumes at Yaw Angles of 0° and 90°

Figures 4.7 to 4.12 show the ratio of concentration with and without a building for two different buildings placed at three locations. Experimental data in these figures were extracted from the full-field concentration images in steps of about 10 mm in the streamwise direction. The model predicts a higher recovery rate in the wake of buildings.

4.5 Plumes at Yaw Angles of Between 0° and 90°

The primary goal of this study was to develop a simple model which could be used to predict the plume concentration ratio (C_w/C_w) when a plume encounters buildings at their usual orientation such as 0° or 90° to the wind direction. When the building yaw angle is not equal to either 0° or 90° to the wind direction, then there is a problem calculating the building length scale (R), one of the key variables in this single plume model.

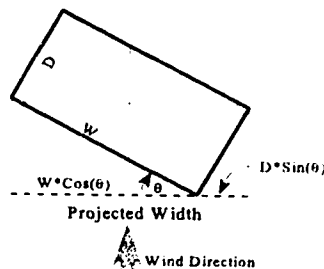


Figure 4.1 Building projected width

4.5.1 Using Projected Building Width to Calculate R

As the Figure 4.1 shows, one way to treat the new width of the building when yaw angle of the building is not at either 0° or 90° is to use the projected width of the building since the plume spread is directly related to this projected width. Then it is reasonable to use the building projected width for calculating the new building length scale (R) in these cases. Figures 4.13 to 4.18 show that the model is still be able to predict the plume concentration ratio. The theory always overpredicts when applied to the taller building used in this study. These results suggest that the building length scale (R) may not depend simply on projected building width.

4.5.2 Linearly Interpolating R Using R_{90} and R_0

Considering how streamlines pass around the building, when the building yaw angle increases from 0° to 90° a building becomes more streamlined. The projected width does not account for this streamlining effect. As an alternative, the building length scale (R) was calculated as a linear interpolation between R at 90° and R at 0° . As Figures 4.19 and 4.20 show, if the new length scale (R) calculated using linear interpolation from the following equation,

$$R = (R_{90} - R_0) \left(\frac{\theta}{90} \right) + R_0 \quad (4.3)$$

the predicted value fits the experimental data a bit better. Even though this method is not used by the current model, it gives a hint that the appropriate building length scale (R) for wind angles that are not at 0° or 90° is not as simple as $R = L^{1/3} S^{2/3}$.

4.6 Comparing the Predicted Concentrations to Linescan Measurements

Another technique used in this study to measure the plume concentration at precise locations was the linescan method. As Figure 4.21 shows the model predicted value and

the linescan measurements agree well with each other. This confirms that this simple single plume model does a good job in predicting the plume concentration ratio (C_w/C_{in}).

4.7 Error in Interpreting the Measured Concentrations as Ground Level Concentrations

Due to surface light reflection errors, the dual laser sheet used in the current studies to illuminate the tracer, the fluorescent dye, could not be lowered to the positions closer than 5mm to the ground. All the horizontal full-field images were taken at 5mm above the ground. The data from the full-field concentration images were used as the ground level concentrations to compare with the model. From Equation (3.19), the plume concentration at 5mm above the ground level will be,

$$C_{5mm} = C_o \exp\left(-\frac{(5.0)^2}{2\sigma_{z,w}^2}\right) \quad (4.4)$$

The percentage error caused by the interpretation of measured concentration at $z = 5mm$ as the ground level concentration at $z = 0mm$ is,

$$error \% = \frac{C_{0mm} - C_{5mm}}{C_{0mm}} \times 100 \quad (4.5)$$

Substituting Equations (4.4) and (3.20) into Equation (4.5),

$$\begin{aligned} error \% &= \frac{C_o - C_o \exp\left(-\frac{(5.0)^2}{2\sigma_{z,w}^2}\right)}{C_o} \\ &= 1 - \exp\left(-\frac{(5.0)^2}{50.0 + 2.5x^{1.05}}\right) \end{aligned} \quad (4.6)$$

The calculated errors from interpreting the measured concentrations as the ground level concentrations at specified x locations for plume are shown in Table 4.1.

Table 4.1 Error from Interpreting Measured Concentration at $z = 5\text{mm}$ as Ground Level Concentration

x , dist. fr. source	error
170 mm	3.05%
230 mm	2.15%
330 mm	1.65%
430 mm	1.33%

From this, using the measured concentrations at $z = 5\text{mm}$ above the ground as the ground level concentrations is reasonable.

4.8 Empiricism in this Plume Model

In deriving the single plume model three fundamental constants were determined using various amounts of empirical manipulation.

- The constants (0.45 and 0.8) used in the $\phi(x^+/R)$ function both have a low level of empiricism since they were determined by comparing the measured data for two different model buildings at three different streamwise locations for buildings at both 0° and 90° yaw angle.
- The constant, $(1+a)(1-b)$ exponent is used in Equation (3.8) and (3.12) to relate the plume crosswind spread to the plume vertical spread and streamwise velocity. The value of this product has a high level of empiricism because it was determined by comparing measured profiles visually to determine a best fit, with an emphasis on getting the correct value at the building front face.

4.9 Comparison to Other Models

One way to test the current model is to compare it with other existing models. Some of the Gaussian models were briefly discussed in Chapter 3 are used here when making concentration predictions at the rear face of a building. The equation used to calculate the plume concentration (C_w) for no building case was Equation (3.6). To calculate (C_w) for the case of a building present, Equation (3.1) was used for Gifford (1960) model, Equation (3.2) was used for Ferra and Cagnetti (1980) model, and Equation (3.3) was used for Huber and Snyder (1982) model. For the no building case, plume crosswind and vertical spreads were calculated using Equations (3.17) and (3.20). Equation (3.28) with its exponent $(1+a)(1+b) = 1.5$ was used for the present model. The results are shown in the following tables. Note that the constant k used in Gifford (1960) model was set at 1.0 as the centre value of his suggested 0.5 to 2.0 range.

Table 4.2 Comparing Predicted and Measured Concentration Ratios (C_w/C_w) at the Building Rear Face for Building *A* at Yaw angle $\theta = 0^\circ$

Distance from Source Models	$x = 190 \text{ mm}$		$x = 290 \text{ mm}$		$x = 390 \text{ mm}$	
	Predicted	Measured	Predicted	Measured	Predicted	Measured
Gifford (1960)	0.07	0.15	0.09	0.20	0.12	0.23
Ferra & Cagnetti (1980)	0.18	0.15	0.23	0.20	0.27	0.23
Huber & Snyder (1982)	0.18	0.15	0.28	0.20	0.38	0.23
Present Study	0.17	0.15	0.25	0.20	0.26	0.23

Table 4.3 Comparing Predicted and Measured Concentration Ratios (C_w/C_w) at the Building Rear Face for Building *B* at Yaw angle $\theta = 0^\circ$

Distance from Source Models	$x = 190 \text{ mm}$		$x = 290 \text{ mm}$		$x = 390 \text{ mm}$	
	Predicted	Measured	Predicted	Measured	Predicted	Measured
Gifford (1960)	0.04	0.10	0.06	0.13	0.07	0.17
Ferra & Cagnetti (1980)	0.12	0.10	0.16	0.13	0.16	0.17

Distance from Source Models	x = 190 mm		x = 290 mm		x = 390 mm	
	Predicted	Measured	Predicted	Measured	Predicted	Measured
Huber & Snyder (1982)	0.09	0.10	0.14	0.13	0.19	0.17
Present Study	0.08	0.10	0.12	0.13	0.16	0.17

Table 4.4 Comparing Predicted and Measured Concentration Ratios (C_w/C_{w0}) at the Building Rear Face for Building A at Yaw angle $\theta = 90^\circ$

Distance from Source Models	x = 190 mm		x = 290 mm		x = 390 mm	
	Predicted	Measured	Predicted	Measured	Predicted	Measured
Gifford (1960)	0.07	0.26	0.09	0.32	0.12	0.35
Ferra & Cagnetti (1980)	0.31	0.26	0.36	0.32	0.40	0.35
Huber & Snyder (1982)	0.09	0.26	0.14	0.32	0.18	0.35
Present Study	0.28	0.26	0.38	0.32	0.38	0.35

Table 4.5 Comparing Predicted and Measured Concentration Ratios (C_w/C_{w0}) at the Building Rear Face for Building B at Yaw angle $\theta = 90^\circ$

Distance from Source Models	x = 190 mm		x = 290 mm		x = 390 mm	
	Predicted	Measured	Predicted	Measured	Predicted	Measured
Gifford (1960)	0.14	0.22	0.17	0.27	0.19	0.34
Ferra & Cagnetti (1980)	0.20	0.22	0.25	0.27	0.28	0.34
Huber & Snyder (1982)	0.23	0.22	0.34	0.27	0.46	0.34
Present Study	0.23	0.22	0.31	0.27	0.37	0.34

Tables 4.2 to 4.5 show that the current model accurately predicts plume concentration ratios at the rear face of a building. The Gifford (1960) model always under-predicts the same concentration ratio. The Ferra and Cagnetti (1980) model predicts the concentration ratios with a quite good agreement with the experimental data. By assuming constant concentration in the building wake recirculation region, the Huber and Snyder (1982)

model has good agreement with the square face building, but not other shape of buildings as the results show.

4.10 Summary

In this chapter the experimental data from the PLIF and linescan method were compared with the predicted values from the newly developed single plume model. The main conclusions that can be made are:

- The plume measured concentration ratios of C_w/C_{w0} were determined by dividing the experimental values C_w by C_{w0} . Only in the cases when building yaw angle was at either 0° or 90° were the average peak concentrations from both sides of a building was used to define C_{w0} . Otherwise, the local maximum C_w was used.
- The theory does a reasonably good job when the building yaw angles were 0° and 90° .
- The theory is not good at predicting the concentration ratio when the building yaw angle is other than 0° or 90° and the projected frontal width is used.
- The theory gives a slightly better estimates if the building length scale is calculated by linearly interpolation between R_{90} and R_0 when building yaw angle was between 0° and 90° .
- The theoretically predicted values are close to the measured data from linescan method.
- The newly developed model is more more accurate than other existing models in predicting the plume maximum ground level concentration ratio in the building near-wake region.

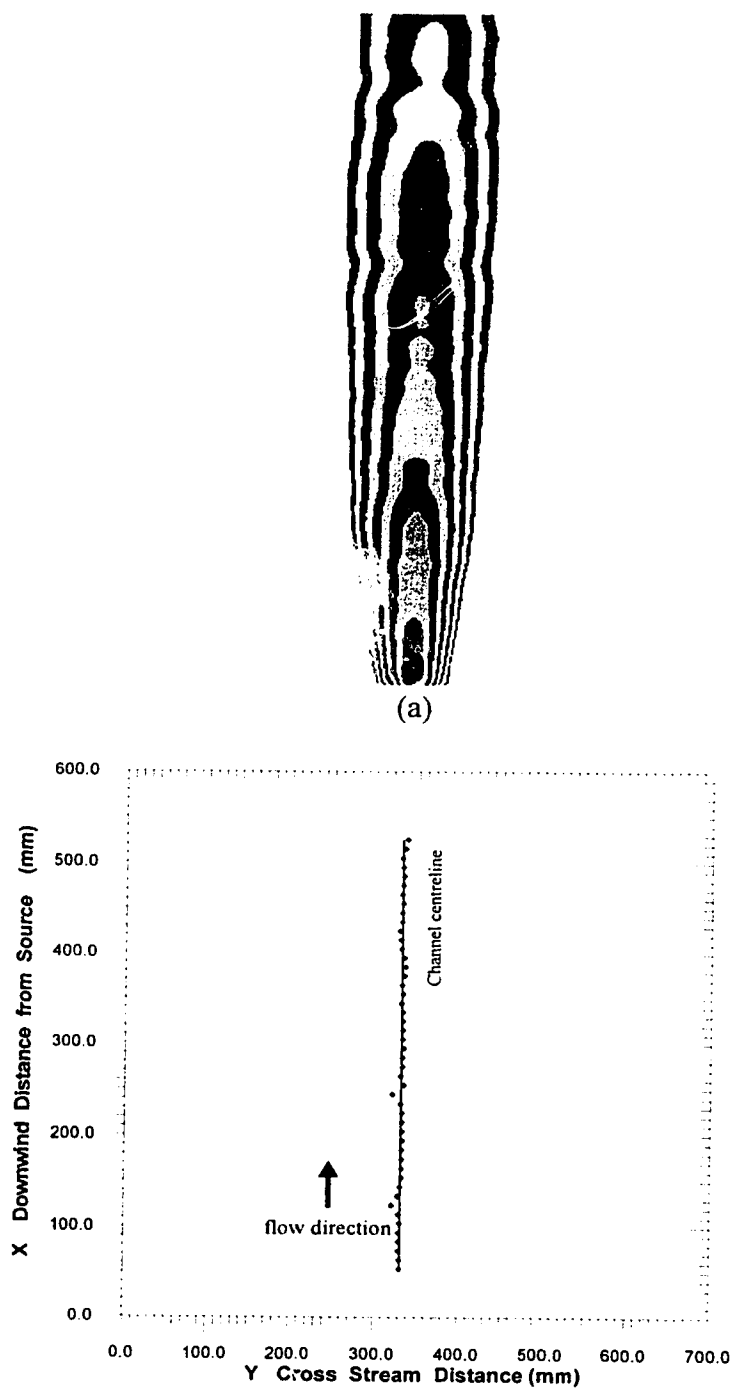


Figure 4.2 Trace of the plume local maximum concentration when no building is present

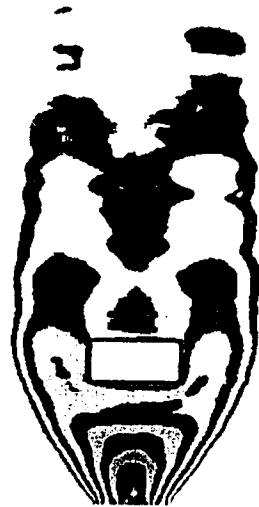
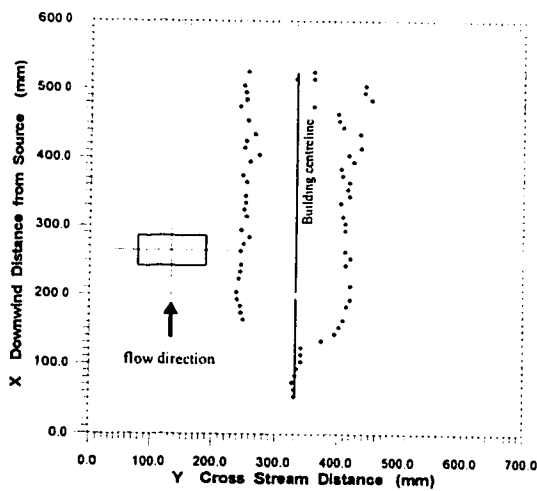
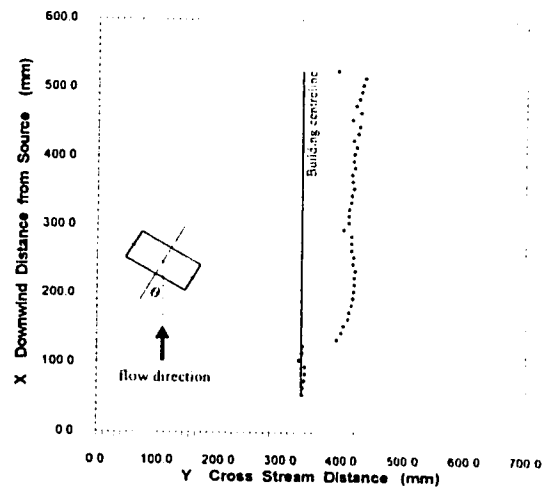
(a) Building *A* at 0°(b) Building *A* at 30°(c) Trace of C_{wi} for building *A* at 0°(d) Trace of C_{wi} for building *A* at 30°

Figure 4.3 Trace of the local maximum concentration for building *A* at $x = 170\text{mm}$ from the source with yaw angle at 0° and 30°. (dimensions of building *A*: 100mm wide \times 50mm height \times 40mm long)

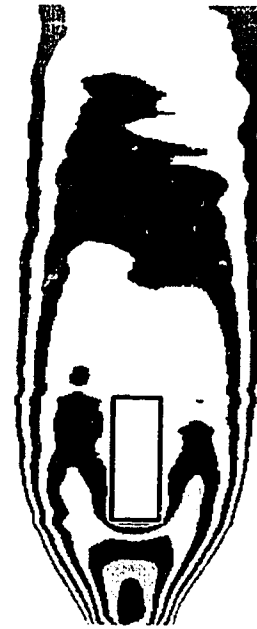
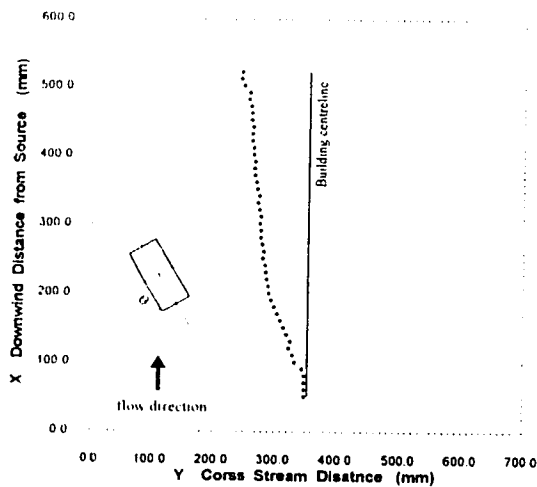
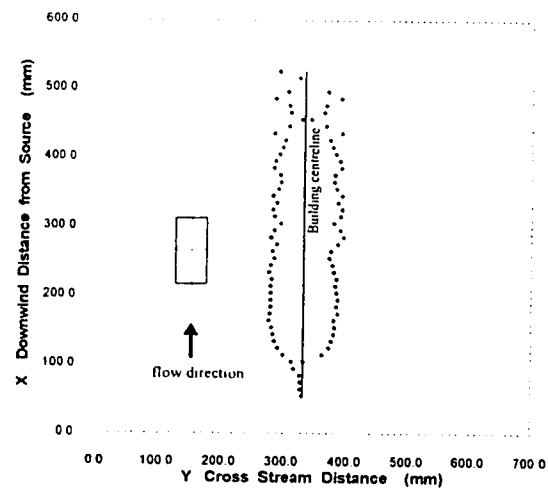
(a) Building *A* at 60°(b) Building *A* at 90°(c) Trace of C_{w1} for building *A* at 60°(d) Trace of C_{w1} for building *A* at 90°

Figure 4.4 Trace of the local maximum concentration for building *A* at $x = 170\text{mm}$ from the source with yaw angle at 60° and 90°. (dimensions of building *A*: 100mm wide \times 50mm height \times 40mm long)

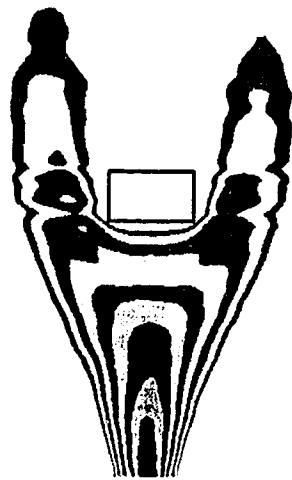
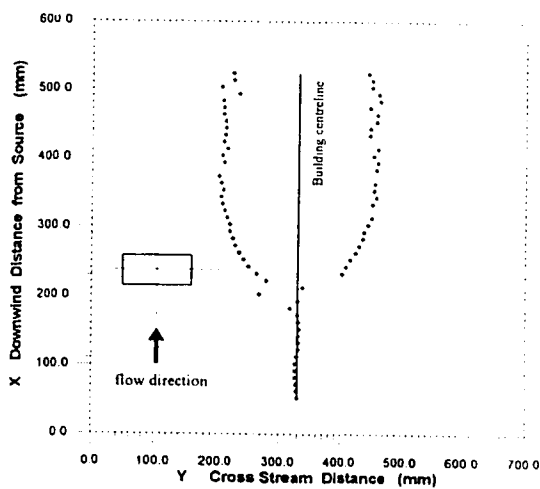
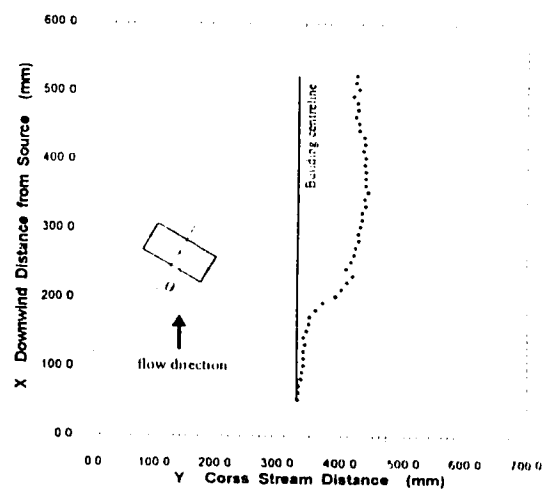
(a) Building *B* at 0°(b) Building *B* at 30°(c) Trace of C_{wi} for building *B* at 0°(d) Trace of C_{wi} for building *B* at 30°

Figure 4.5 Trace of the local maximum concentration for building *B* at $x = 270\text{mm}$ from the source with yaw angle at 0° and 30°. (dimensions of building *B*: 100mm wide \times 100mm height \times 400mm long)

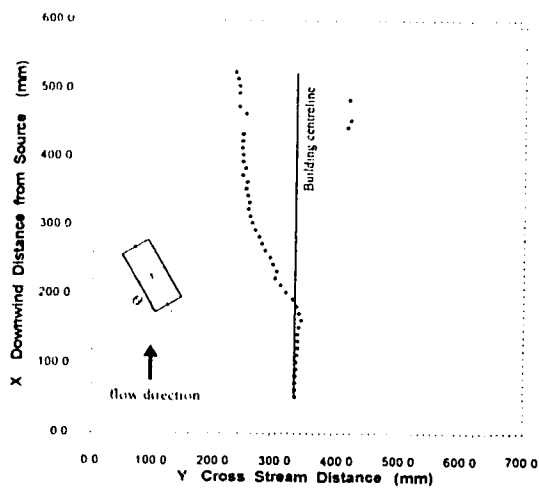
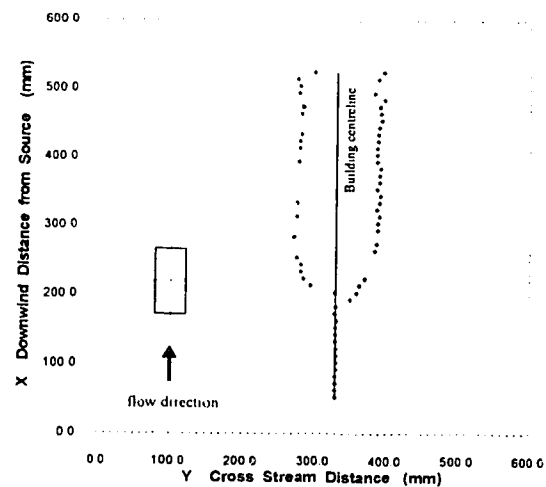
(a) Building *B* at 60°(b) Building *B* at 90°(c) Trace of C_{w_i} for building *B* at 60°(d) Trace of C_{w_i} for building *B* at 90°

Figure 4.6 Trace of the local maximum concentration for building *B* at $x = 270\text{mm}$ from the source with yaw angle at 60° and 90°. (dimensions of building *B*: 100mm wide \times 100mm height \times 40mm long)

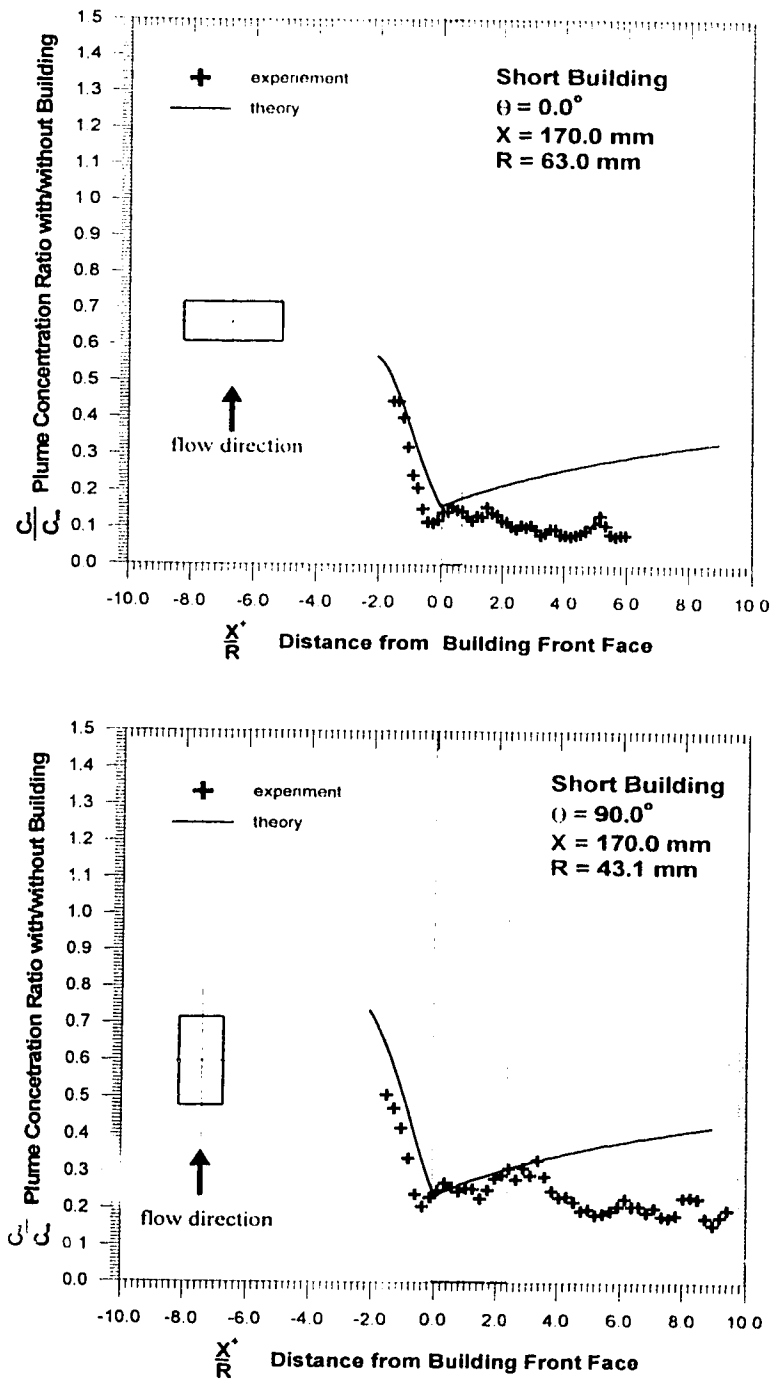


Figure 4.7 Experimental and predicted concentration ratio (C_w/C_{w0}) for short building located at 170mm from source and orientated at 0° and 90°

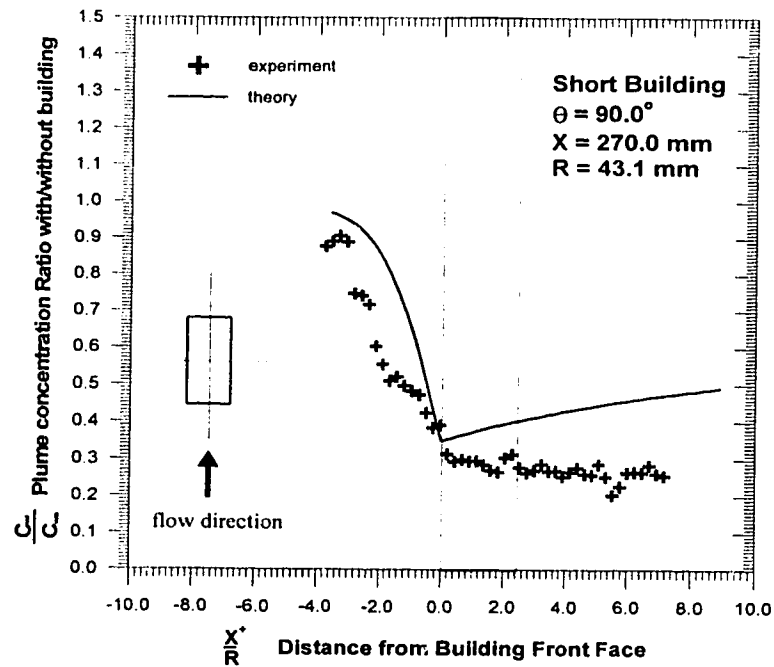
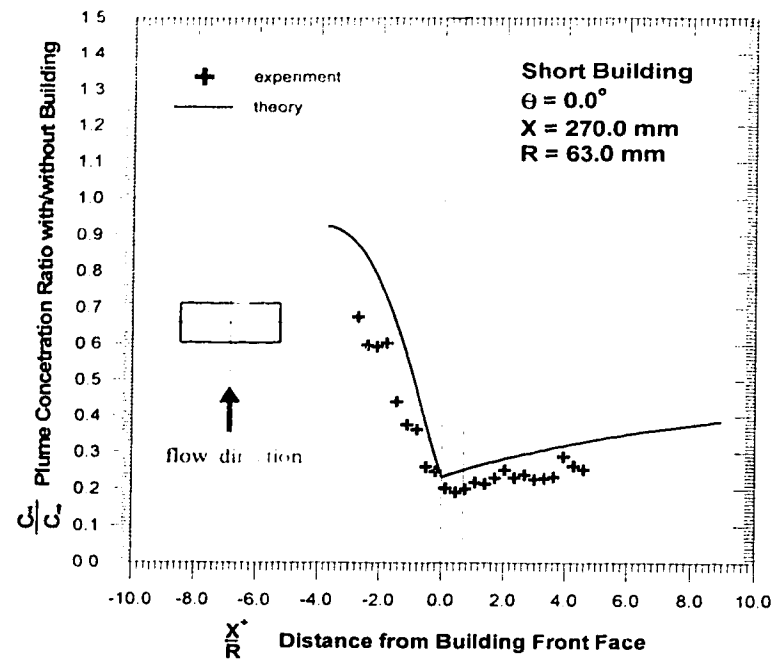


Figure 4.8 Experimental and predicted concentration ratio (C_w/C_{w0}) for short building located at 270mm from source and orientated at 0° and 90°

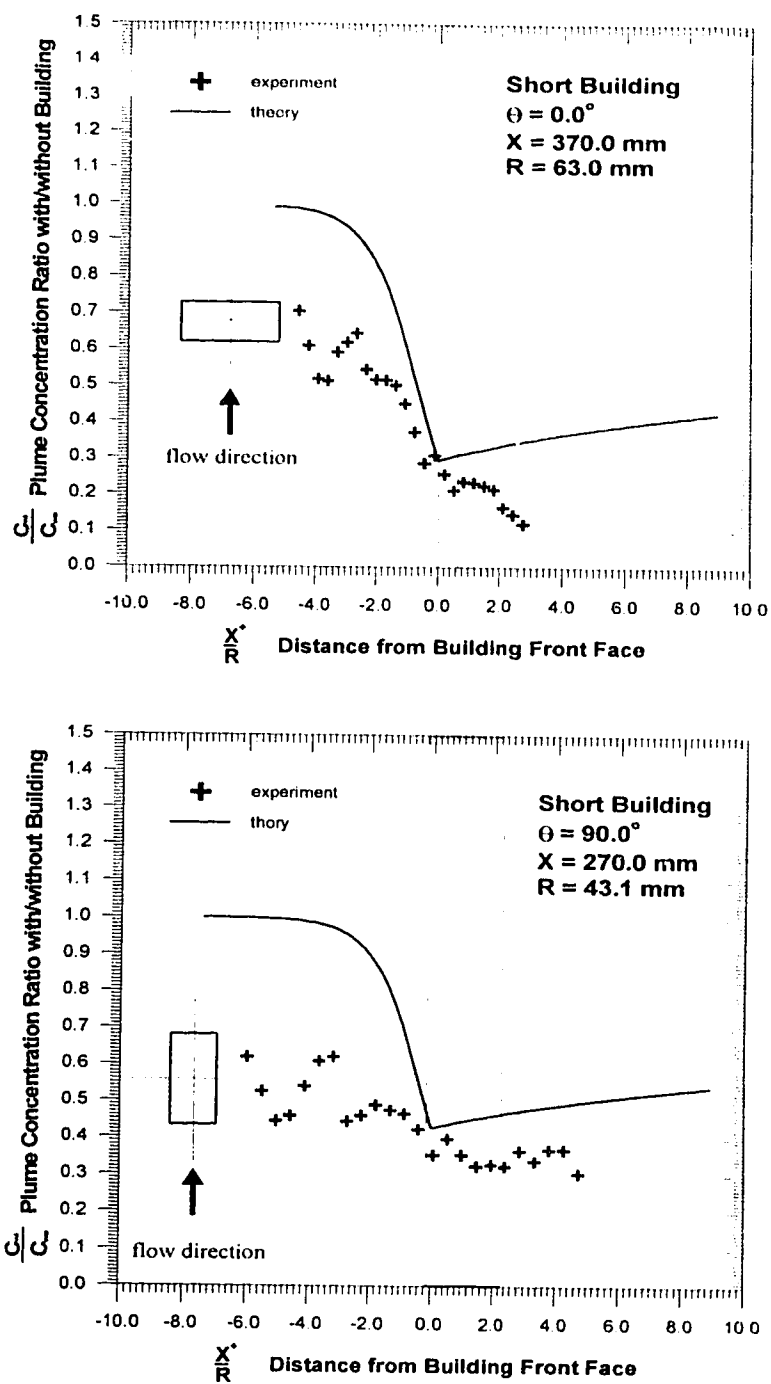


Figure 4.9 Experimental and predicted concentration ratio (C_w/C_w') for short building located at 370mm from source and orientated at 0° and 90°

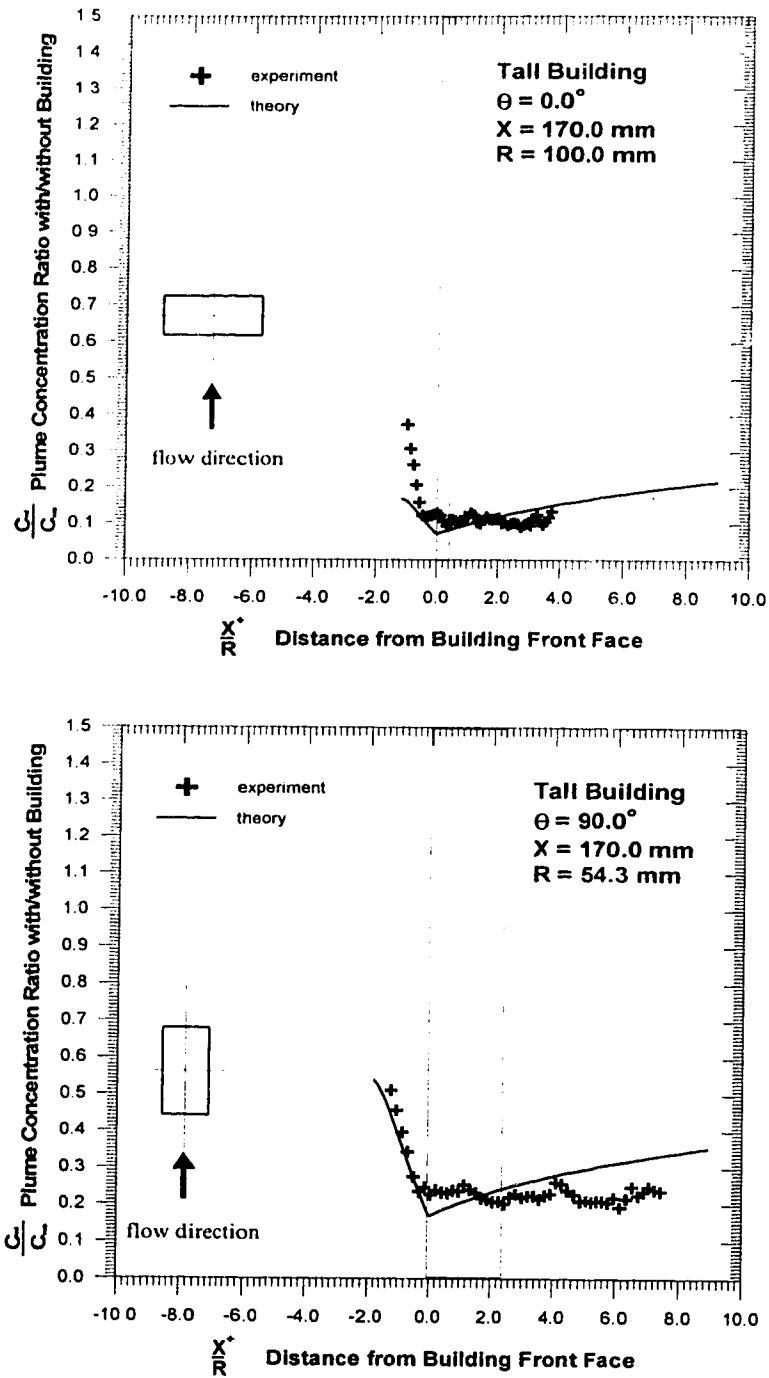


Figure 4.10 Experimental and predicted concentration ratio (C_w/C_{wo}) for tall building located at 170mm from source and orientated at 0° and 90°

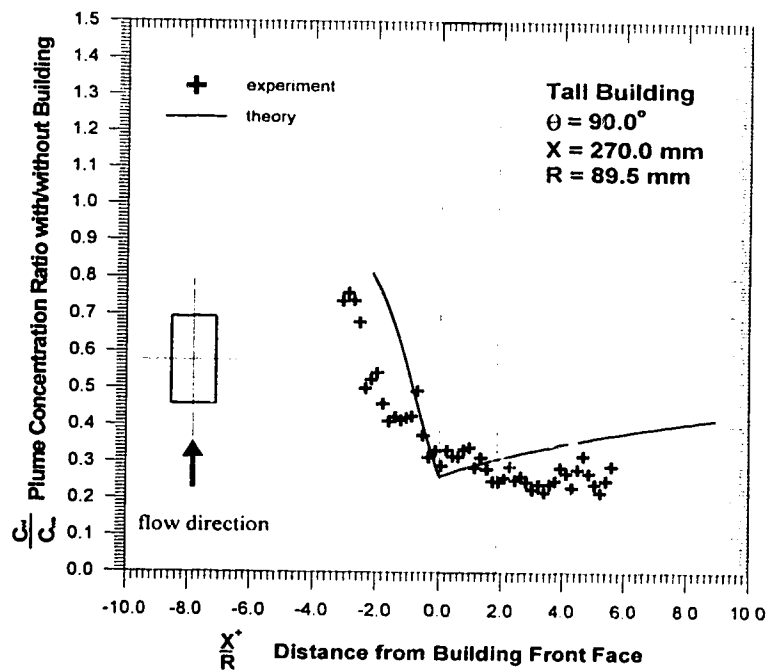
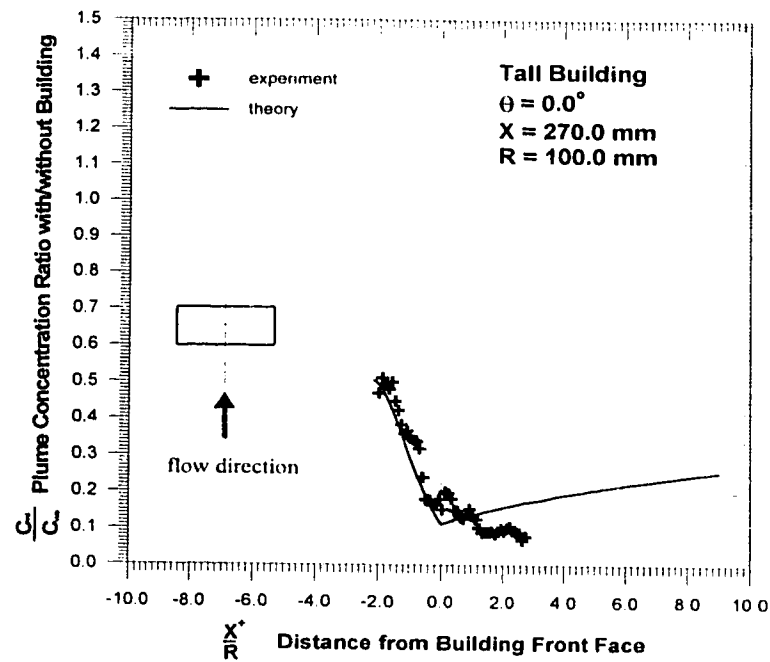


Figure 4.11 Experimental and predicted concentration ratio (C_w/C_w^0) for tall building located at 270mm from source and orientated at 0° and 90°

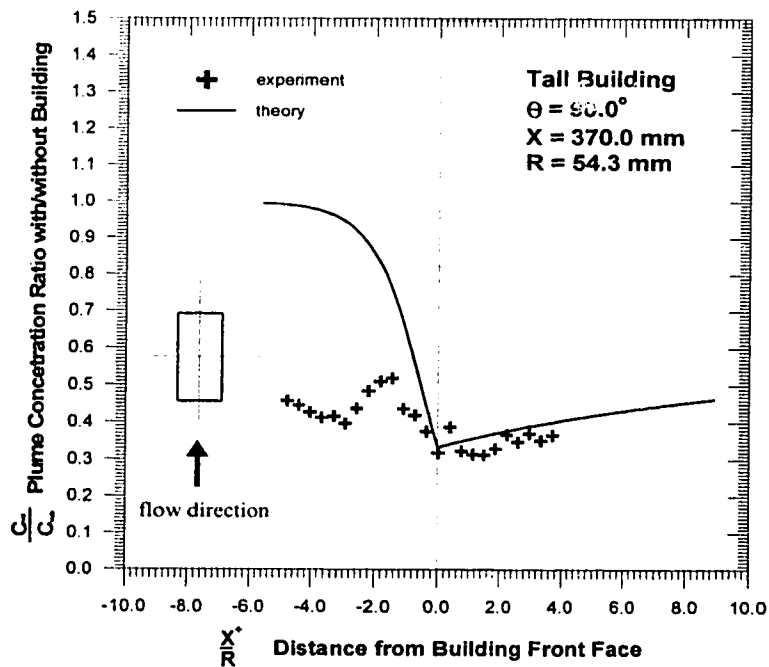
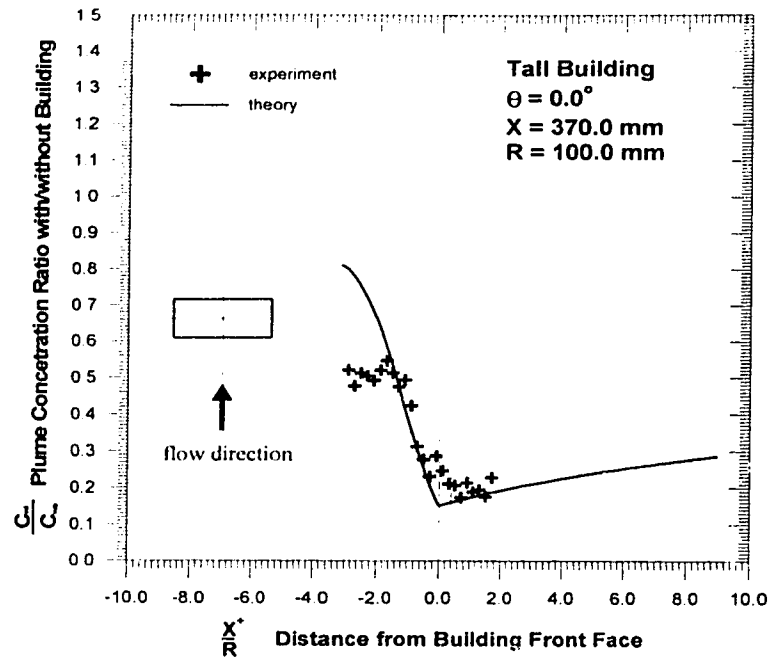


Figure 4.12 Experimental and predicted concentration ratio (C_{wi}/C_{wo}) for tall building located at 370mm from source and orientated at 0° and 90°

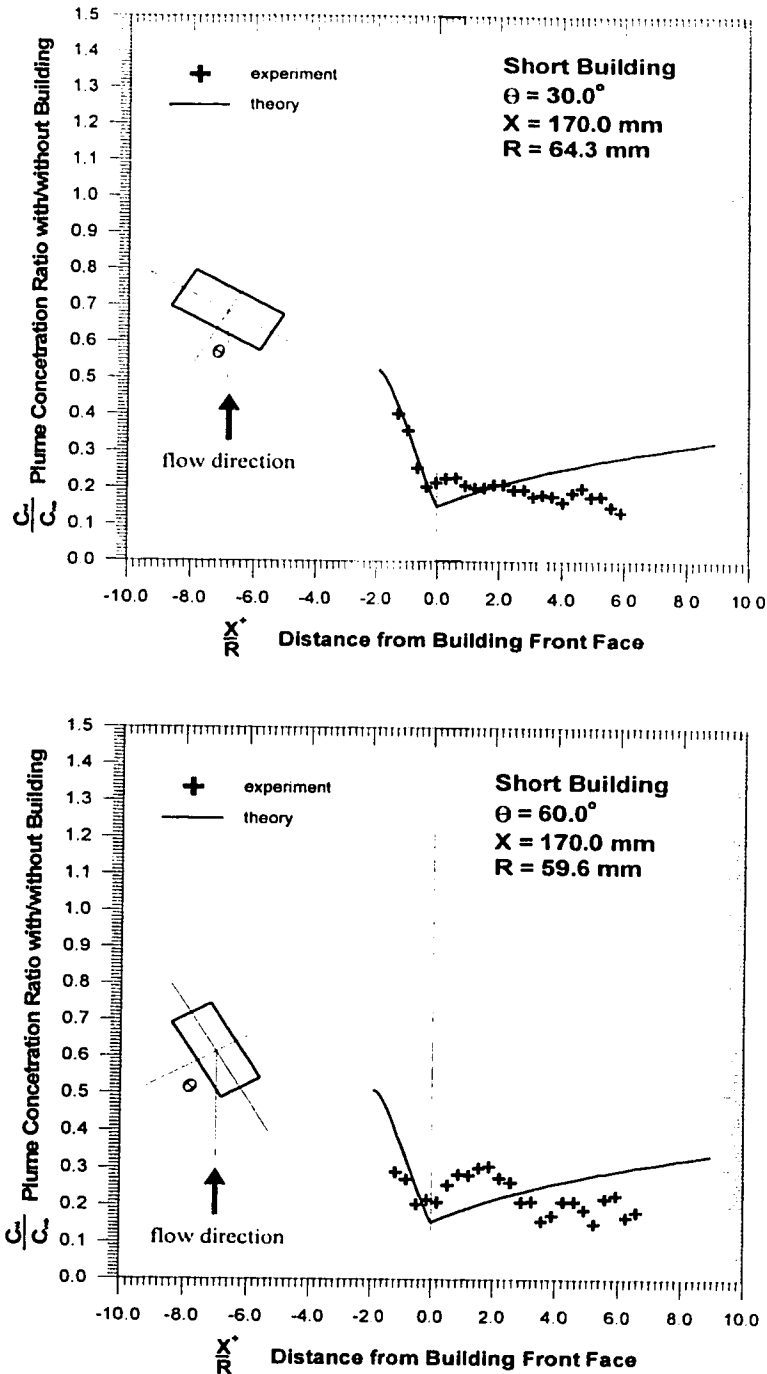


Figure 4.13 Experimental and predicted concentration ratio (C_w/C_{wi}) for short building located at 170mm from source, orientated at 30° and 60° and R calculated using projected width

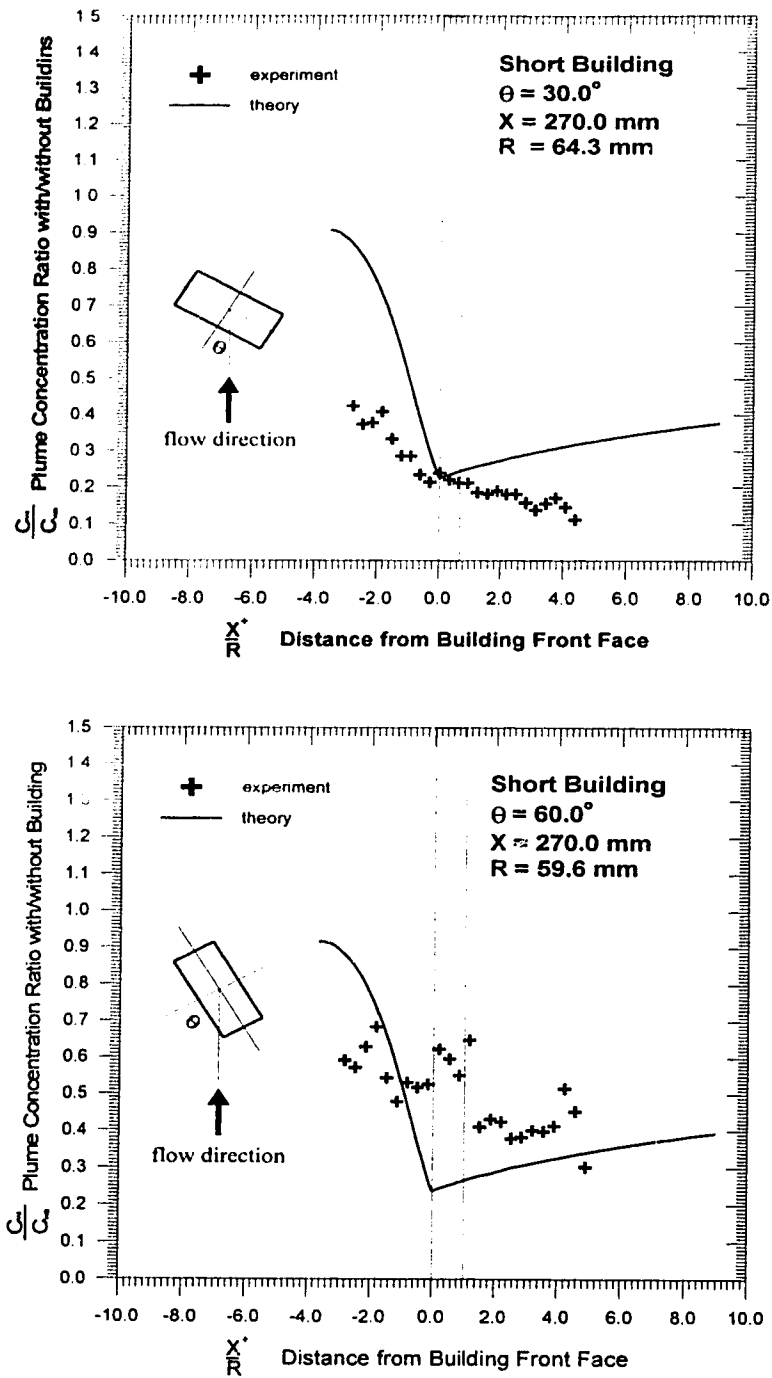


Figure 4.14 Experimental and predicted Concentration ratio (C_w/C_{w0}) for short building located at 270mm from source, orientated at 30° and 60° and R calculated using projected width

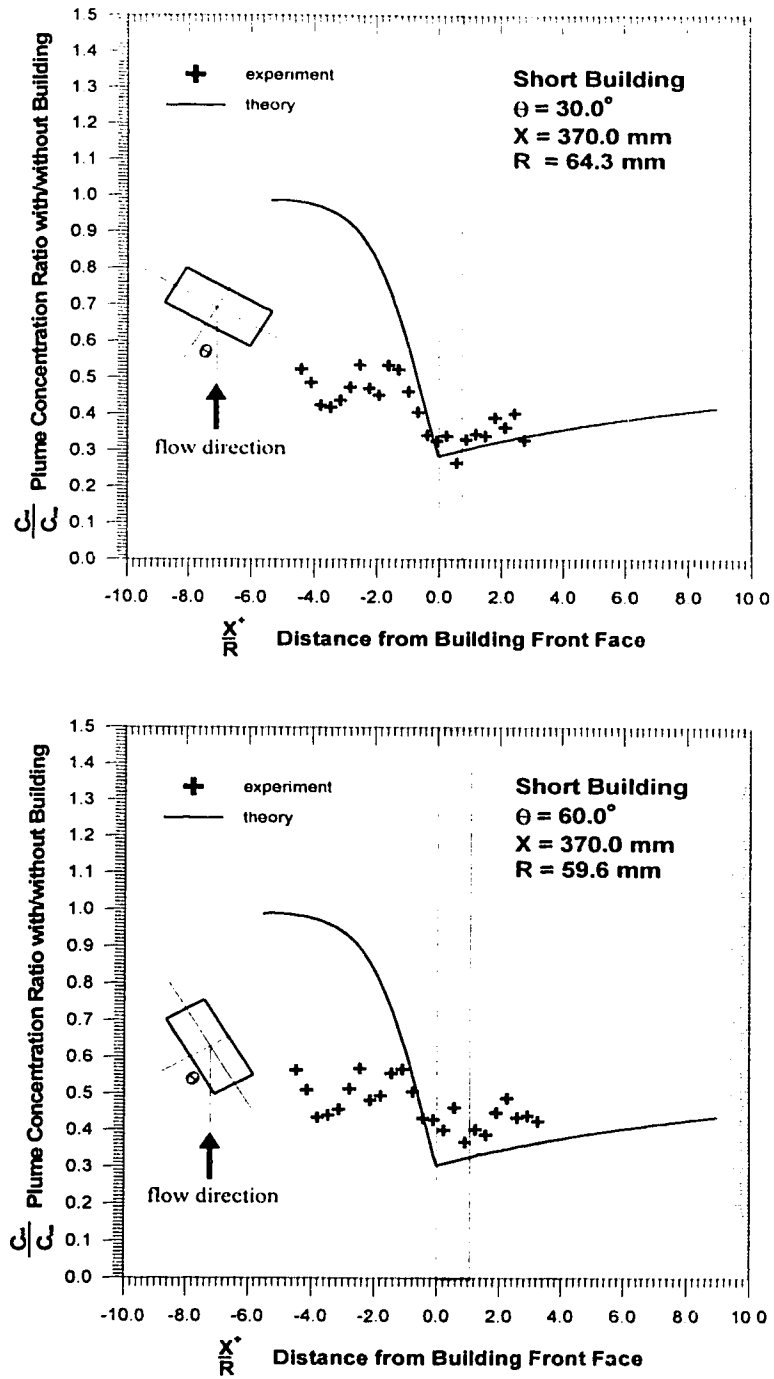


Figure 4.15 Experimental and predicted concentration ratio (C_w/C_w') for short building located at 370mm from source, orientated at 30° and 60° and R calculated using projected width

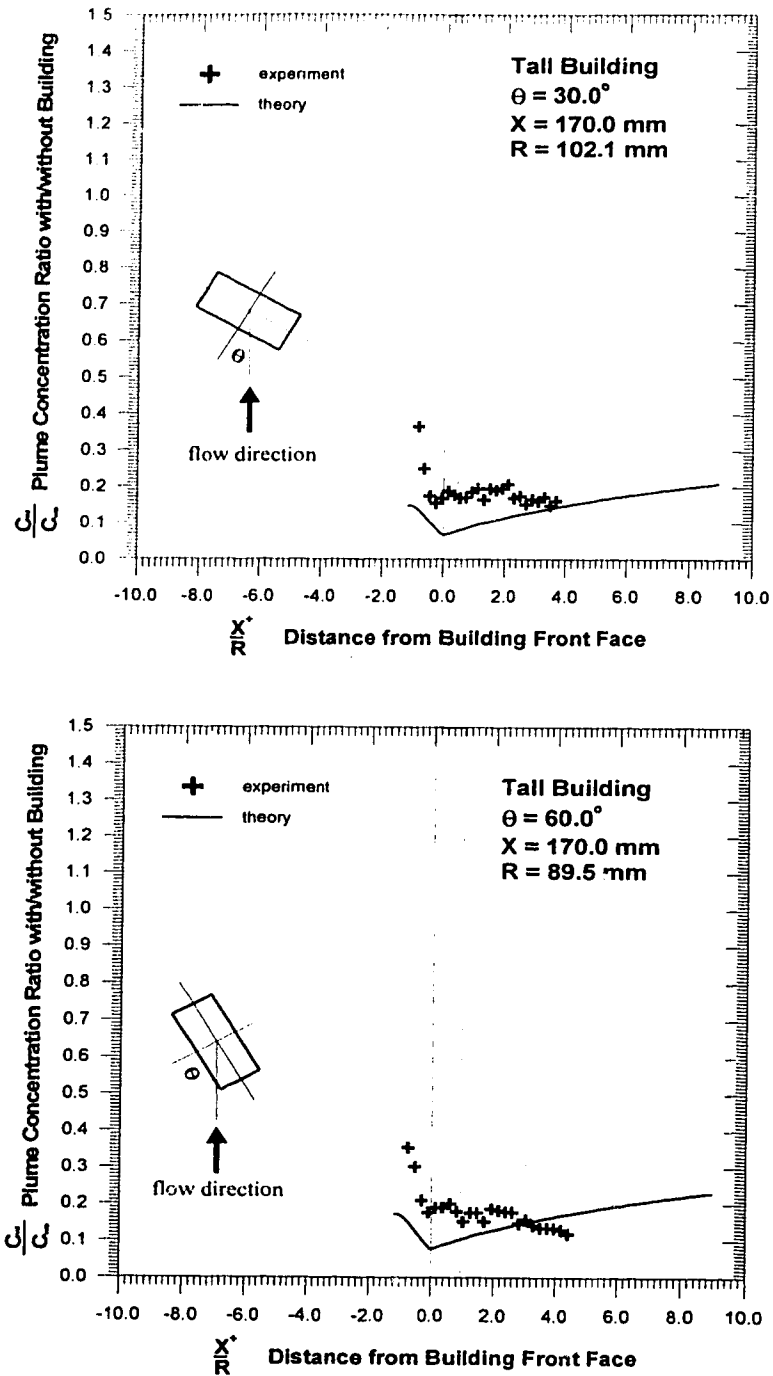


Figure 4.16 Experimental and predicted concentration ratio (C_w/C_{w0}) for tall building located at 170mm from source, orientated at 30° and 60° and R calculated using projected width

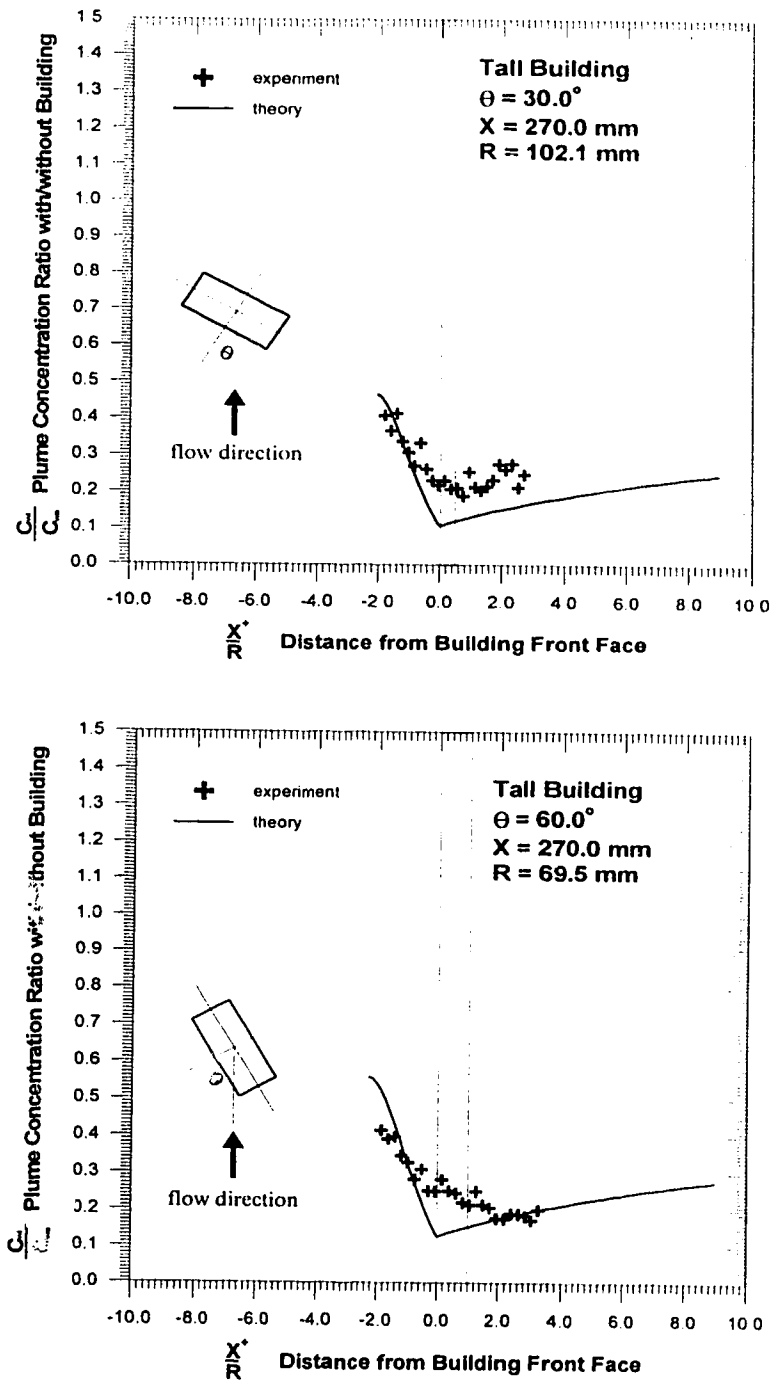


Figure 4.17 Experimental and predicted concentration ratio (C_w/C_{w0}) for tall building located at 270mm from source, orientated at 30° and 60° and R calculated using projected width

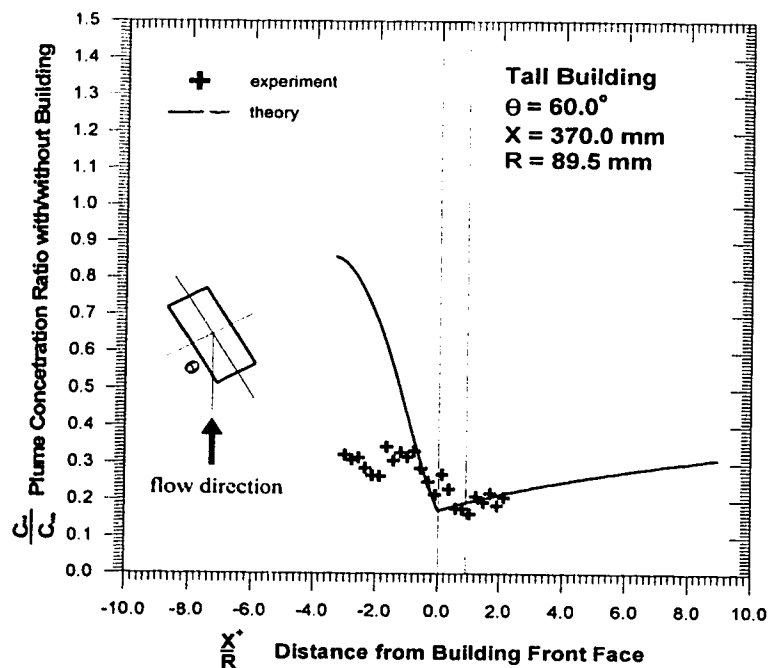
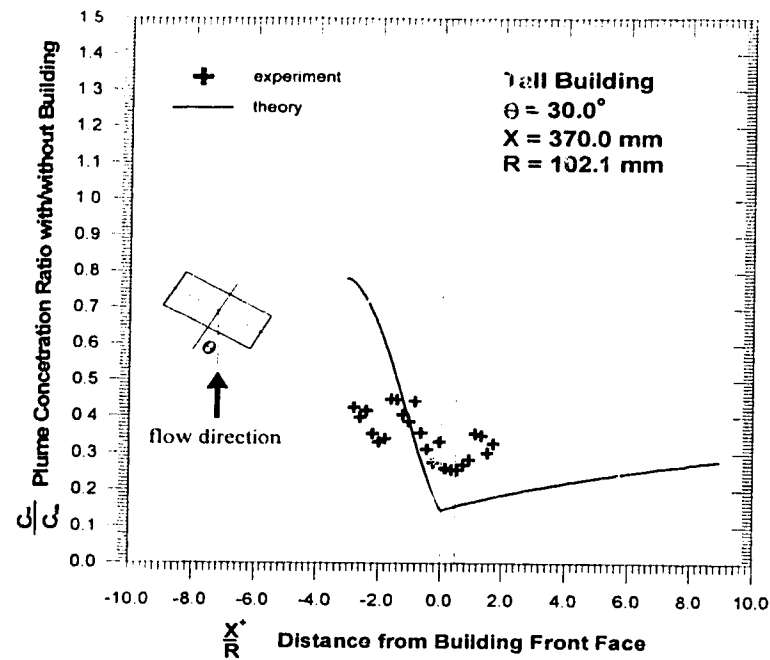
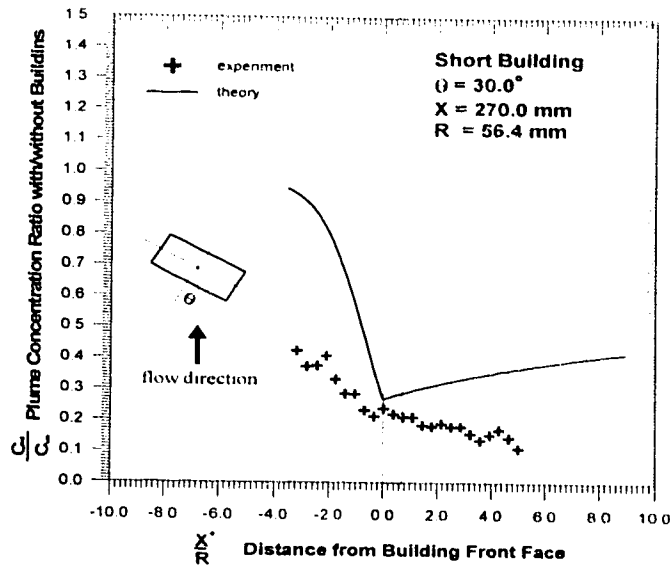
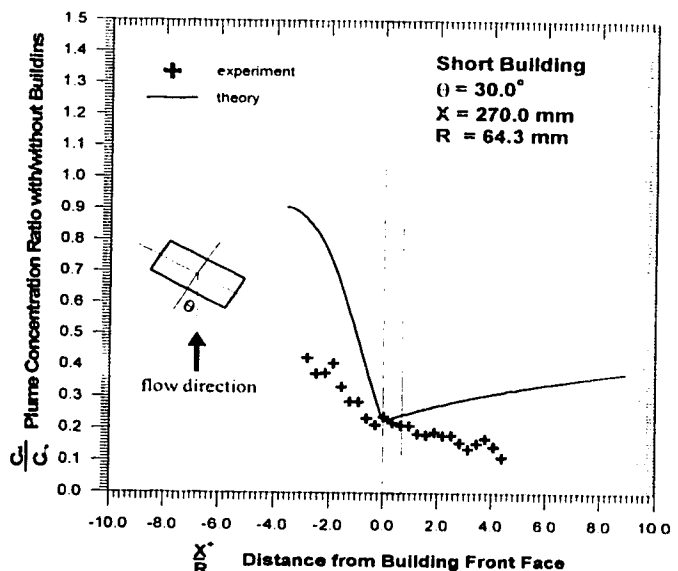


Figure 4.18 Experimental and predicted concentration ratio (C_w/C_w^0) for tall building located at 370mm from source, orientated at 30° and 60° and R calculated using projected width



(a) R calculated using linear interpolation



(b) R calculated using projected width

Figure 4.19 Effects on predicted concentration ratio (C_{wr}/C_{w0}) when using different building length scale (R) for short building at 270mm from source

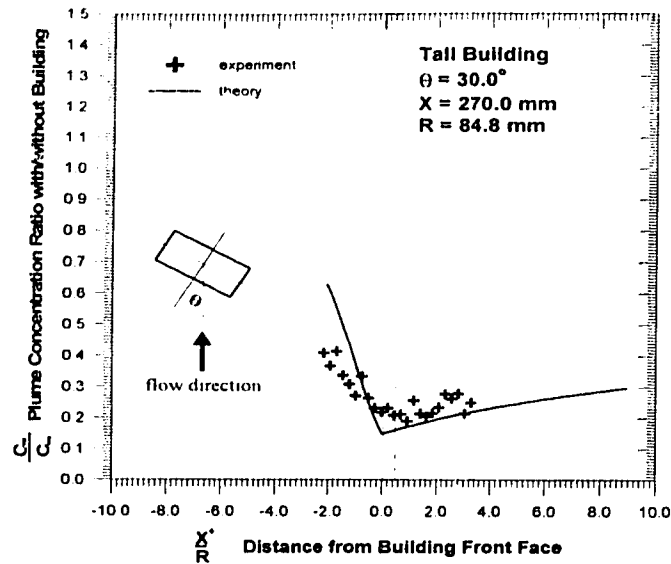
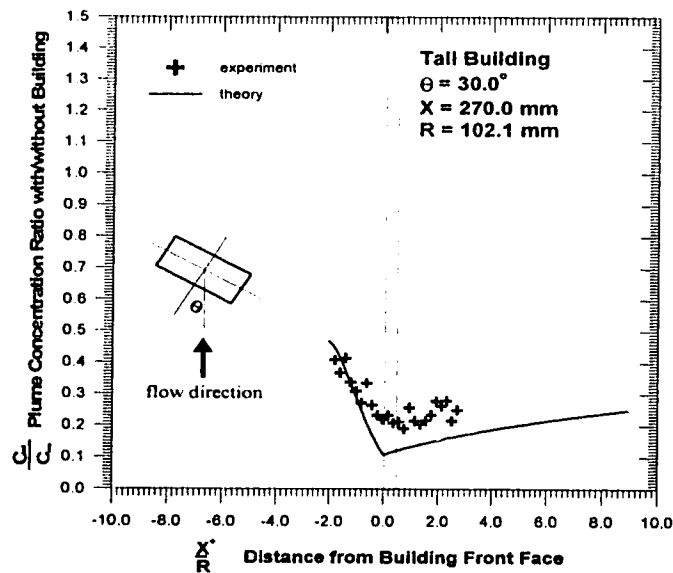
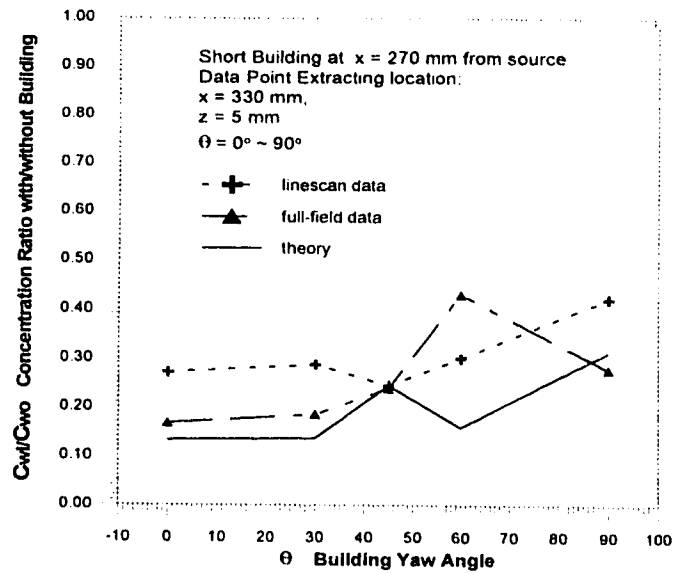
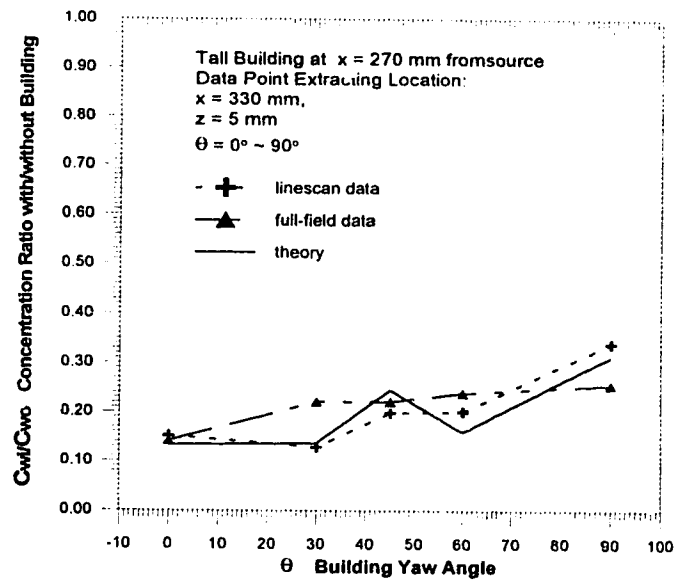
(a) R calculated using linear interpolation(b) R calculated using projected width

Figure 4.20 Effects on predicted concentration ratio (C_w/C_{w0}) when using different building length scale (R) for tall building at 270mm from source



(a) Short building (A)



(b) Tall building (B)

Figure 4.21 Comparison of data from linescan, theory and full-field image at the same x location (buildings at 270mm from source, laser beam at 60mm down wind of the building)

Chapter 5

Summary and Conclusions

5.1 Summary

The primary goal of the present study was to develop a model for plume dispersion on the upwind side, and in the wake region of buildings; and compare it to experiments done with the water channel using both the PLIF and linescan methods. This model incorporates the effects caused by the increase of the crosswind and vertical plume spreads due to the presence of buildings. The crosswind and vertical spreads of a plume are assumed to be directly related to each other through a simple power function. The increase of the plume crosswind and vertical spreads produces the increased dilution of the plume in the vicinity of buildings. The new component of this single plume model is its ability to simulate the gradual and continuous increase in the plume crosswind spread upwind of a building.

In Chapter 2, the experimental apparatus and methods were outlined. First, the development of the required boundary layer, using the newly designed roughness base plates with a turbulence generating screen attached to the flow straightener at the test section entrance, was discussed in detail. The Laser Doppler Velocimetry (LDV) system and the operation principle used to collect velocity data were discussed. Results from LDV measurement for the boundary layer velocity profiles with and without the building were also presented. The mechanisms of laser induced fluorescence were then introduced. Both linescan and full-field images were collected over a 300 second time average and stored in a computer hard disk to permit faster collection rate and allow a maximum number of images to be processed. The collected raw images were corrected and analysed later. A description of the image processing techniques developed to obtain concentration data

from the digital ensemble averaged image was then given. Finally, the image correction process for light attenuation, light scattering, and conversion from fluorescent light intensity to concentration for both the linescan and dual light sheet methods were discussed.

In Chapter 3, the single plume model developed for this thesis was discussed and an equation to predict the plume concentration ratio of (C_{wf}/C_{wo}) was derived. The three key assumptions of this model were the ambient flow was homogeneous, the plume vertical spread could be modelled using an empirical power function to relate it to the crosswind spread, and the velocity ratio at the same x' location could be expressed in terms of crosswind and vertical plume spreads through an empirical power function based on a mass conservation analogy. A new coordinate system was defined and used to coordinate the new model with the new x origin set at the building front face. The building length scale (R) defined by Wilson (1979) was used to normalize the plume travel distance in the streamwise direction and the plume crosswind spread as described in Equation (3.22). To better correlate with the experimental data the normalized plume spread in Equation (3.22) was divided into two regimes that added a constant additional spread to the plume downwind of the building front face, with an exponential increase in the plume spread as the flow approaches the building front face.

Chapter 4 presented the experimental results and demonstrated the effectiveness of the single plume model when predicting the plume concentration ratio (C_{wf}/C_{wo}) . This simple model is able to predict the plume concentration ratio quite accurately if the building yaw angle either at 0° or 90° , but it over predicts the plume recovery rate downwind of buildings. Comparing with other Gaussian models such as Gifford (1960), Ferra and Cagnetti (1980) and Huber and Snyder (1982) model, the present model demonstrated superior capability and accuracy on predicting plume maximum ground level concentration especially in the near wake region. Considering the simplifying assumptions made when deriving the single plume model to predict the plume

concentration ratio, this model appears to be a remarkably accurate estimate for concentration in plumes from a ground-level source encountering a building.

5.2 Conclusions

The single plume model for predicting concentration ratios with the presence of a building represents a new physical modelling approach which has been successfully applied in this thesis. Conclusions that can be made from the current studies are:

- Plume dilution actually starts several building heights upwind and is significantly reduced at the front face of a building. This is not as what was indicated and modelled by earlier research with the plume dilution suddenly occurring at the downwind side of a building.
- Plume spreads (crosswind and vertical) are the key factors in modelling plume dispersion process even with presence of a building. These crosswind and vertical plume spreads were affected by building yaw angles.
- The Planar Laser Induced Fluorescence technique is feasible for both flow visualization and concentration measurements for a plume dispersing around a building from a ground-level source. The linescan technique is also a good, feasible method for its high spatial resolution, fast sample rate and convenience in measuring plume crosswind concentrations in various along-wind and vertical positions.
- The Gaussian plume model is still a good, simple model for predicting the plume ground-level concentrations in the along-stream direction if the plume spreads could be appropriately modelled.

5.3 Recommendations for Future Studies

In future studies a more and thorough investigation of fluid mechanics around buildings should be undertaken to try and determine the actual relations between the lateral and vertical spread of a plume when a building is present. This would permit the comparison

to the assumption made for the current model when determining the plume vertical spread. Also, the strong horse-shoe vortex, that wraps around buildings, should be examined because it must have a great effect on bringing down more fluid from the upper portion of a building to dilute the plume at the upwind face.

As the Figures 5.1 to 5.4 show, a two plume model, with a pair of plumes coming from imaginary locations upstream of a building, should be the next step to predict the plume concentration more accurately. Lin and Hildemann (1996) have done some work on predicting the plume concentrations from dual sources with no obstacle present.

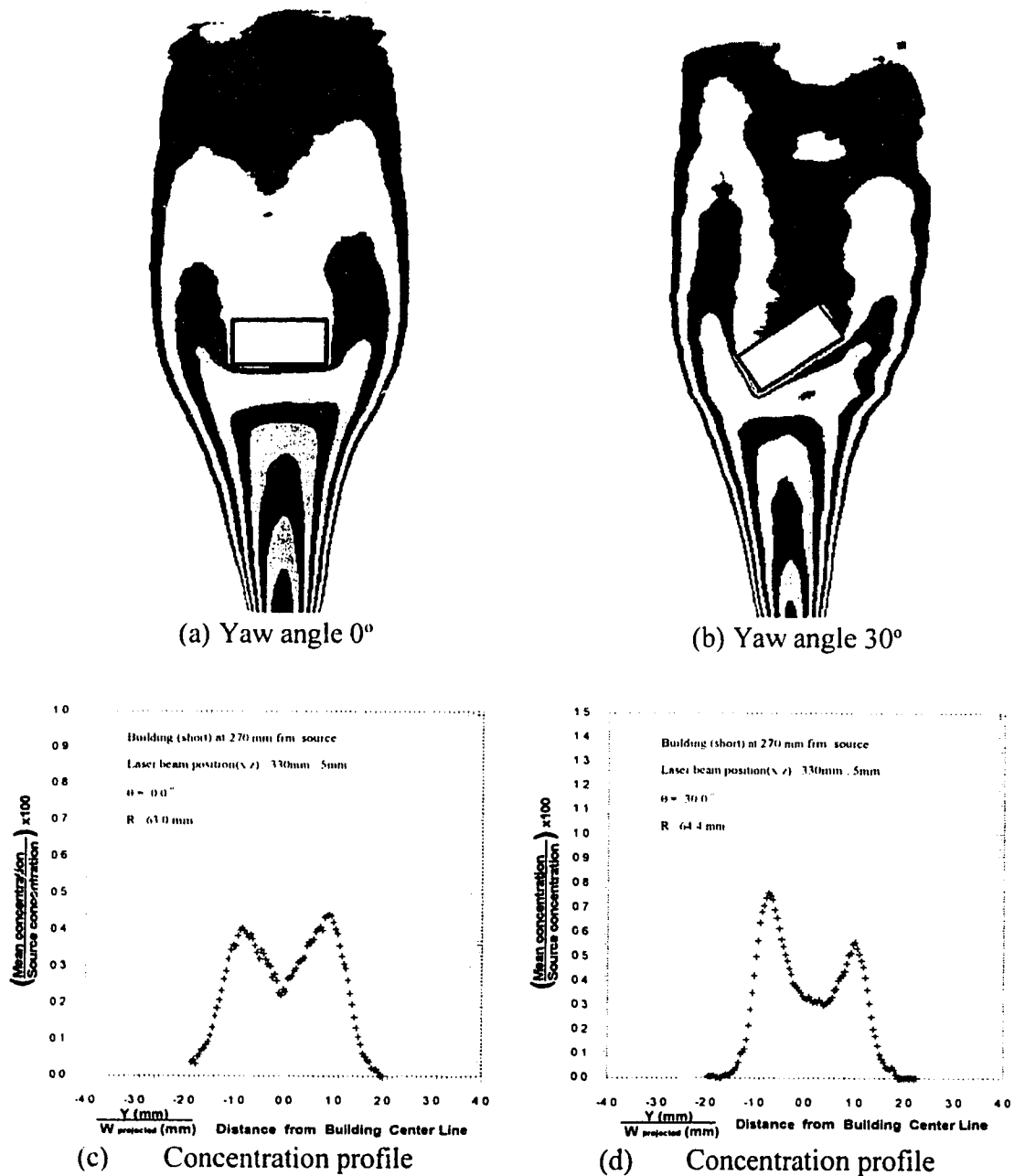
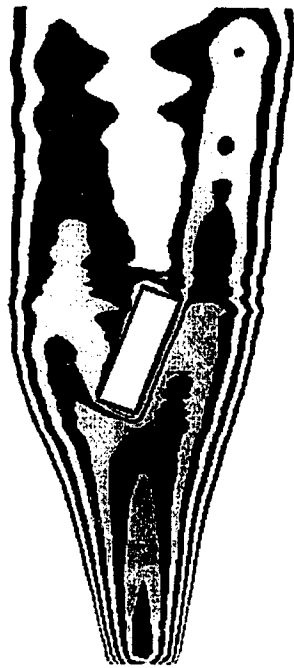
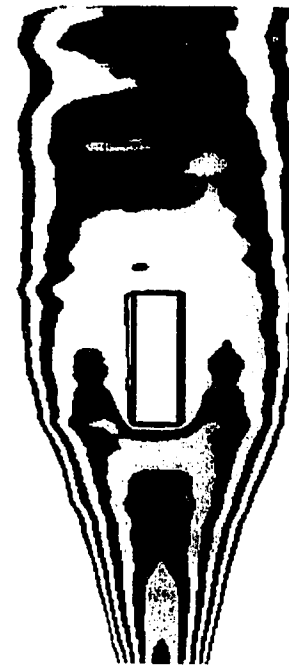
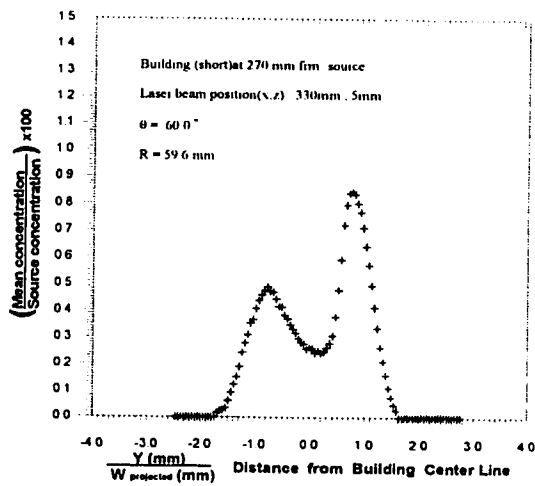
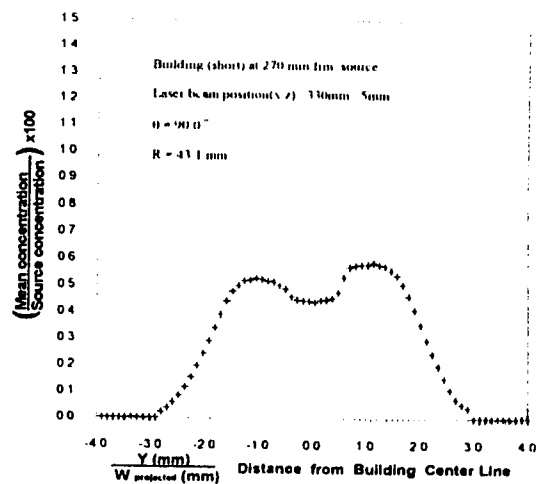


Figure 5.1 Plume concentration contour from full-field image and concentration profiles from linescan data for building *A* at yaw angle 0° and 30° (100mm wide \times 50mm height \times 40 mm long). (a) and (b) building location at $x = 270$ mm from the source; (c) and (d) laser beam position at $x = 330$ mm, $z = 5$ mm

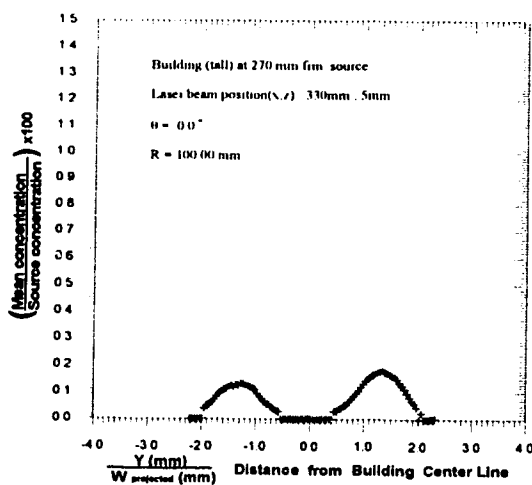
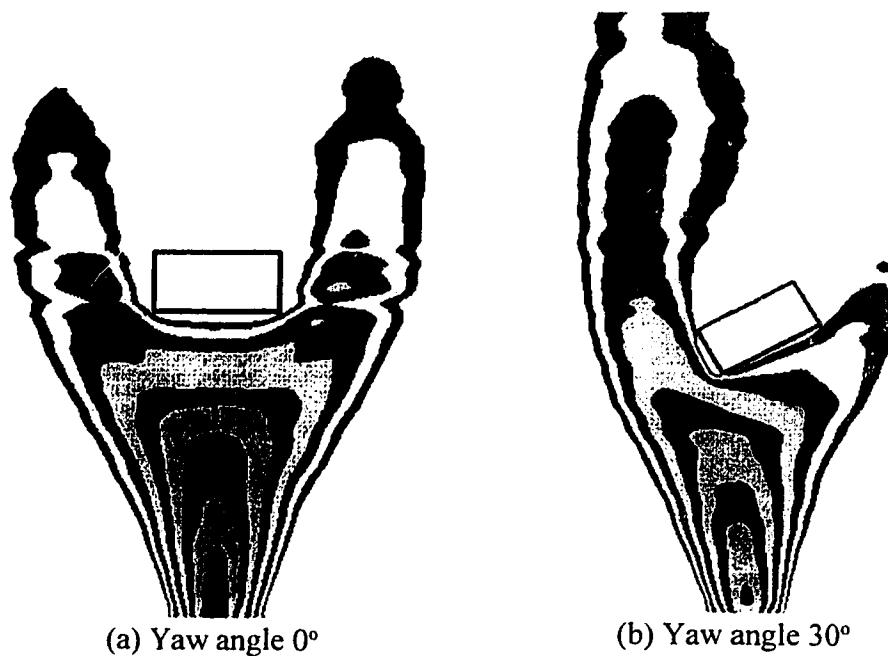
(a) Yaw angle 60° (d) Yaw angle 90° 

(c) Concentration profile

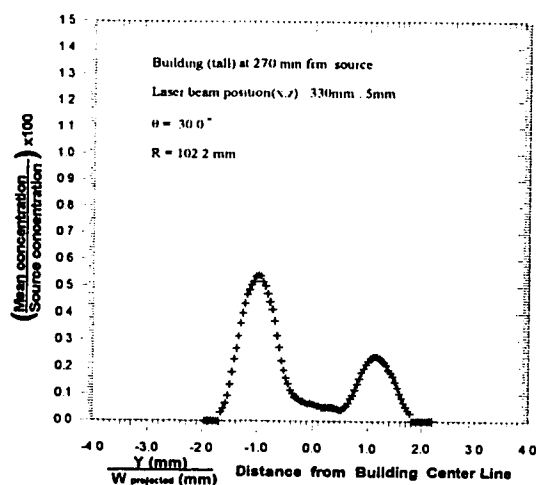


(d) Concentration profile

Figure 5.2 Plume concentration contour from full-field image and concentration profiles from linescan data for building *A* at yaw angle 60° and 90° (100mm wide \times 50mm height \times 40 mm long). (a) and (b) building location at $x = 270$ mm from the source; (c) and (d) laser beam position at $x = 330$ mm, $z = 5$ mm



(c) Concentration Profile



(d) Concentration profile

Figure 5.3 Plume concentration contour from full-field image and concentration profiles from linescan data for building *B* at yaw angle 0° and 30° (100mm wide \times 100mm height \times 40 mm long). (a) and (b) building location at $x = 270$ mm from the source; (c) and (d) laser beam position at $x = 330$ mm, $z = 5$ mm

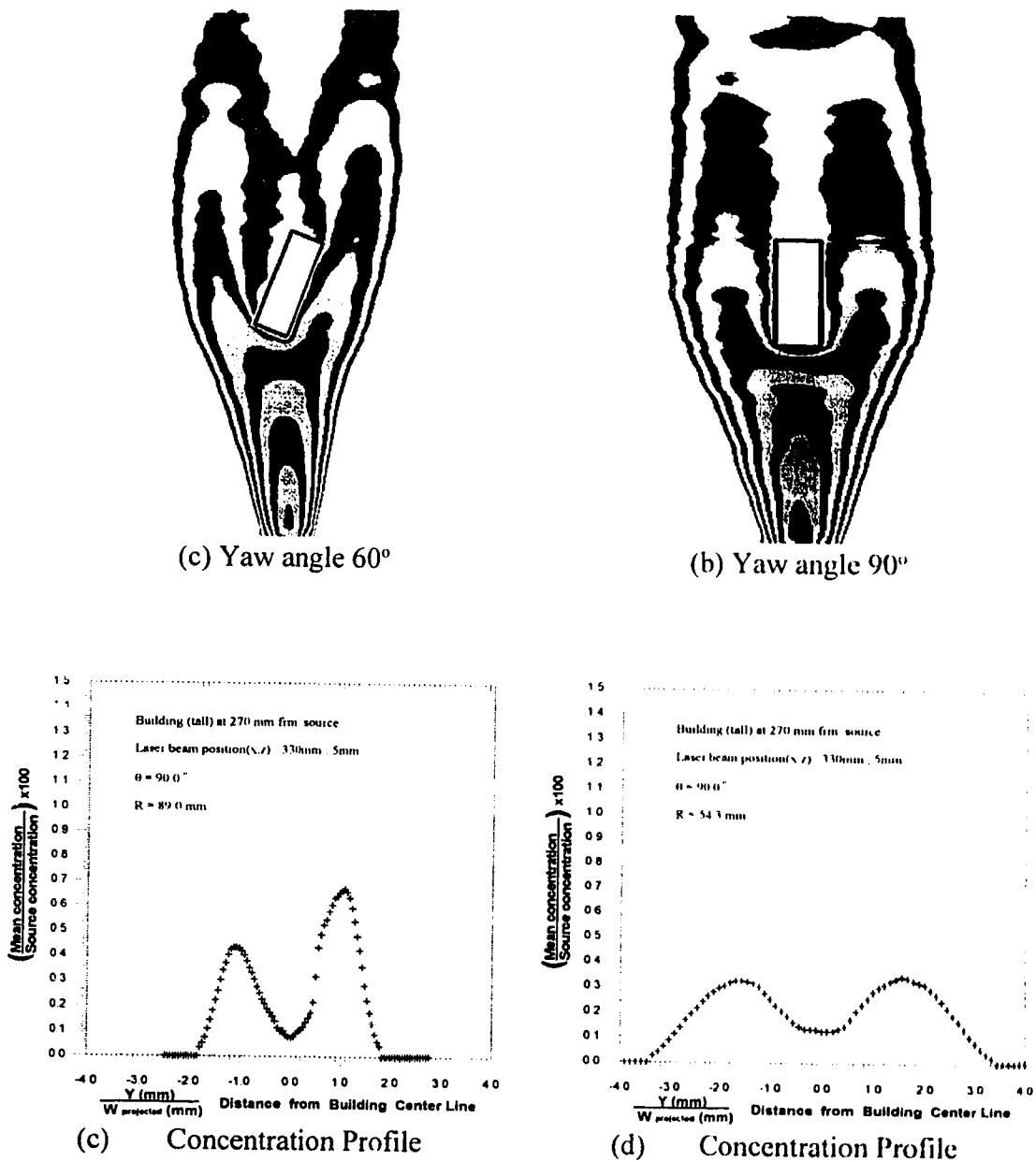


Figure 5.4 Plume concentration contour from full-field image and concentration profiles from linescan data for building *B* at yaw angle 60° and 90° (100mm wide \times 100mm height \times 40 mm long). (a) and (b) building location at $x = 270$ mm from the source; (c) and (d) laser beam position at $x = 330$ mm, $z = 5$ mm

References

- Barker, C.D. (1982) "A virtual source model for building wake dispersion in nuclear safety calculations". Central Electricity Board Report No. TPRD/B/0072/N82.
- Berlyand, M.E., Genikhovich, E.L., Grecheva, I.G., and Tsarev, A.M. (1987b) "Account on building in atmospheric diffusion models". Proc. WMO Conf. Air Poll. Modelling and its Appl. (Leningrad, USSR, 1986) VIII Tech. Doc. WMO/TD No.187, 96-103.
- Brungart, T.A., Petrie, H.L., Harbison, W.L. and Merkle, C.L. (1991) "A fluorescence for measurement of slot injected fluid concentration profiles in a turbulent boundary layer". *Experiments in Fluids*, **11**, 9-16.
- Campell, R.P. (1991) "Image Processing Techniques for Analysis of Full Colour Turbulent Jet Images". M.Sc. Thesis, University of Alberta, Edmonton, Alberta, Canada.
- Counihan, J., Hunt, J.C.R and Jackson, P.S. (1974) "Wakes behind two-dimensional surface obstacles in turbulent boundary layers". *J. Fluid Mech.*, **64**, 529-563.
- Csanady, G.T. (1973) "Turbulent Diffusion in the Environment". D. Reidel Publishing Company, Dordrecht-holland, pp.67.
- Drivas, P.J. and Shair F.H. (1974) "Probing the air flow within the wake downwind of a building by means of a tracer technique". *Atmospheric Environment*, **8**, 1165-1175.

- Ferrel, V. and Cagnetti, P. (1980) "A simple model for estimating airborne concentration downwind of buildings for discharges near ground level". Proceedings of the Commission of the European Communities' Seminar on Radioactive Release and their dispersion in the atmosphere following a hypothetical reactor accident, Risø, Denmark.
- Genikhovich, E.L. and Snyder, W.H. (1994) "A new mathematical model of pollutant dispersion near a building". 8th AMS Conf. on Appl. Air Poll. Meteorol., with AWMA, Jan. 23-28, 1994, Nashvill, TN.
- Genikhovich, E.L., Kulik, A.S., Filatova, E.N. and Tsarev, A.M. (1987) "Experimental substantiation of the method of air pollution calculation for industrial site". Trudy GGO (Trans. Main Geophys. Observatory), **511**, 44-54.
- Gifford, G.A. (1960) "Atmospheric dispersion calculations using the generalized Gaussian plume model". Nuclear Safety, **1**, 56-59.
- Guilbault, G.G. (1973) "Practical fluorescence". New York, Marcel Deker, Inc.
- Halitsky, J. (1977) "Wake and dispersion models for EBR-II building complex". *Atmospheric Environment*, **11**, 577-596.
- Huber, A.H. and Snyder, W.H. (1982) "Wind tunnel investigation of the effects of a rectangular-shaped building on dispersion of effluents from short adjacent stacks". *Atmospheric Environment*, **16**, 2837-2848.
- Huber, A.H. (1989) "The influence of building width and orientation on plume dispersion in the wake of a building". *Atmospheric Environment*, **23**, 2019-2116.

- Huber, A.H. (1991) "Wind tunnel and Gaussian plume modelling of building wake dispersion". *Atmospheric Environment*, **25A**, 1237-1249.
- Huber, A.H., Arya, S.P., Raijala, S.A. and Borek, J.W. (1991) "Preliminary studies of video images of smoke dispersion in the near wake of a model building". *Atmospheric Environment*, **25A**, 1199-1209.
- Hunt, J.C.R. (1971b) "A theory for the laminar wake of a two-dimensional body in a boundary layer". *J. Fluid Mech.*, **49**, 159.
- Hunt, J.C. & Puttock, J.S. and Snyder W.H. (1979) "Turbulent diffusion from a point source in stratified and neutral flows around a three-dimensional hill Part I Diffusion equation analysis". *Atmospheric Environment*, **13**, 1227-1239.
- Ippen, E.P., Shank, C.V. and Dienes, A. (1971) "Rapid photobleaching of organic laser dyes in continuously operated devices". *IEEE, J. Quantum Electronics*, **QE-7**, 178-179.
- Johnston, C.R. (1994) "Downwash of stack gas plume". M.Sc. Thesis, University of Alberta, Edmonton, Canada.
- Koochesfahanni, M.M. (1984) "Experiments on turbulent mixing and chemical reactions in a liquid mixing layer". Ph.D. thesis, California Institute of Technology.
- Lee, J.T., Darrell L., Robert E. Lawson, Jr., William E. Clements and Donald E. Hoard (1991) "A Video image analysis system for concentration measurements and flow visualization in building wakes". *Atmospheric Environment*, **25A**, 1211-1225.

- Li, W.W. and Meoney, R.N. (1983a) "Gas dispersion near a cubical model building. Part I. Mean concentration measurements". *J. Wind Engr. Ind. Aero.*, **12**, 15-33.
- Li, W.W. and Meoney, R.N. (1983b) "Gas dispersion near a cubical model building. Part II. Concentration fluctuation measurements". *J. Wind Engr. Ind. Aero.*, **12**, 35-47.
- Lin, J.S. and Hildemann, L.M. (1996) "Analytical solution of the atmospheric diffusion equation with multiple sources and height-dependent wind speed and eddy diffusivities". *Atmospheric Environment*, **30**, 239-254.
- Martinuzzi, R. and Tropea, C. (1993) "Flow around surface-mounted, three-dimensional obstacles". *ASME Journal of Fluid Engineering*, **115**, 85-92.
- Ogawa, Y., Oikawa, S. and Uehara, K. (1983) "Field and wind tunnel study of the flow and diffusion around a model cube II, near field and cube surface flow and concentration patterns". *Atmospheric Environment*, **17**, 1161-1171.
- Ogawa, Y. And Oikawa, S. (1982) "A field investigation of the flow and diffusion around a model cube". *Atmospheric Environment*, **16**, 207-???
- Parker, C.A. (1968) "Photoluminescence of solutions". New York, Elsevier.
- Poreh, M and Cermak, J.E. (1991) "Wind tunnel measurements of line integrated concentration". *Atmospheric Environment*, **25A**, 1181-1187.
- Puttock, J.S. and Hunt J.C.R (1979) "Turbulent diffusion from sources near obstacles with separated wakes Part I An eddy diffusion model". *Atmospheric Environment*, **13**, 1-13.

- Raupach, M.R., Thom, A.S. and Edwards, I. (1980) "A wind-tunnel study of turbulence close to regularly arrayed rough surface". *Boundary-layer Meteorol.*, 18, 373-397.
- Robins, A.G. and Fackrell, J.E. (1980) "Laboratory studies of dispersion near buildings". Central Elec. Gen. Board, Report MM/MECH/TF 235.
- Robins A.G. and Castro I.P. (1977a) "A wind tunnel investigation of plume dispersion in the vicinity of a surface-mounted cube part I Flow field". *Atmospheric Environment*, 11, 291-298.
- Robins A.G. and Castro I.P. (1977b) "A wind tunnel investigation of plume dispersion in the vicinity of a surface-mounted cube part II The concentration field". *Atmospheric Environment*, 11, 299-311.
- Thompson, R.S. (1993) "Building amplification factor for sources near building: a wind tunnel study". *Atmospheric Environment*, 27A, 2313-2325.
- Turner, D.B. (1969) "Workbook of atmospheric dispersion estimates". US Dept. Of Public Health Publication No. 999-AP-26.
- Vincent, J.H. (1977) "Model experiment on the nature of air pollution transport near buildings". *Atmospheric Environment*, 11, 765-774.
- Vincent, J.H. (1978) "Scalar transport in the near aerodynamic wakes of surface-mounted cubes". *Atmospheric Environment*, 12, 1319-1322.
- Walker, D.A. (1987) "A fluorescence technique for measurement of concentration in mixing liquids". *J. Physics E: Scientific Instruments*, 20, 86-94.

- Wilson, D.J. and Netterville, D.D.J. (1978) "Interaction of roof-level plume with a downwind building". *Atmospheric Environment*, **12**, 1051-1059.
- Wilson, D.J. (1979) "Flow patterns over flat roof buildings and application to exhaust stack design". ASHRAE transactions **85**, 284-295.
- Wilson, D.J. and Netterville, D.J. (1979) "Interaction of roof level plume with a downwind building". *Atmospheric Environment*, **12**, 1051-1059.
- Wilson, D.J. and Britter R.E. (1982) "Estimates of building surface concentrations from nearby point sources". *Atmospheric Environment*, **16**, 2631-2646.
- Zelt, B.W. (1991) "Concentration Fluctuations and their Probability Distributions in Laboratory Plumes". Ph.D. Thesis, University of Alberta, Edmonton, Alberta, Canada.

Appendix A

Laser Light Attenuation Correction for Linescan

I. Analysis

Disodium fluorescein, the dye used in the experiment as tracer, has a number of advantages compared to other type of fluorescent dyes such as Rhodamine 207 and Rhodamine 127. Disodium fluorescein is highly soluble in water, shows no toxicity to humans, permeates other materials at an extremely low rate, and can be used to measure a wider range of concentration. It has a high quantum yield fraction, F_Q , typically 85%. The quantum yield fraction F_Q of the dye is the fraction of absorbed photons resulting in fluorescent emission (Guilbault, 1973).

The dye fluorescence when excited by laser light is affected by four factors, as described in Section 2.5.2 of Chapter 2 in this thesis. Attenuation of laser light by absorption and scattering is an important factor causing the dye fluorescence intensity to change along the beam path if the dye concentration is high.

The attenuation dI of excitation light intensity I , as the beam passes through a fluorescein dye solution with local concentration C , is described by the Lambert Beer Law in Brungart *et al*, (1991), which is

$$\frac{dI_{in}(y)}{dy} = -\epsilon C(y) I_{in}(y) \quad (\text{A.1})$$

where y is the distance (mm) along the beam path from a reference location, and ϵ is the laser beam extinction coefficient. The Lambert Beer law considers only first-order attenuation effects, so the laser beam attenuation is linearly proportional to the local dye

concentration and light intensity. Integrating Equation (A.1), the attenuation of the excitation light intensity of the beam at location y will be:

$$I_{in}(y) = I_{in,0} \exp\left(-\varepsilon \int_0^y C(y) dy\right) \quad (\text{A.2})$$

where $I_{in,0}$ is the excitation beam intensity at $y = 0$. The local fluorescent intensity of a small slice, Δy , can be obtained by combining Equation (A.2), the local dye concentration and the quantum yield fraction F_Q .

$$I_f(y) = F_Q \varepsilon C(y) \Delta y I_{in,0} \exp\left(-\varepsilon \int_0^y C(y) dy\right) \quad (\text{A.3})$$

where F_Q is a dimensionless constant. The exponential term in Equation (A.3) accounts for excitation beam absorption and may be large even though $\varepsilon C(y) \Delta y$ is small ($\varepsilon C(y) \Delta y \ll 1$) everywhere because attenuation is cumulative along the beam path. Since the dye fluorescent radiation is randomly polarized and emitted uniformly in all directions in space, there is no need to correct for the directional effects of the fluorescent light itself.

The signal strength from an element captured by the image system, Δy , of dye in the laser beam, (ie. the i -th pixel element), depends on a number of factors such as light collection angle, lens reflections and imperfections, pixel sensitivity, device gain, magnification, excitation beam, and local dye concentration. Effects caused by these factors can be combined and accounted for through a calibration function $f(C_i)$ and calibration constants β_i . Here, $f(C_i)$ is the amplitude gain factor for the i -th pixel element when it responds to the local dye concentration C under the excitation beam intensity $I_{in,(i-1)}$, and β_i is the dark noise (or clear water response) of the image system on each pixel for the photodiode array in the camera.

The digital output signal from the frame grabber for the i -th pixel is a number of counts, $I_{cam, i}$, which is proportional to input excitation light intensity and a function of the local dye concentration C_i , and the local laser beam excitation intensity $I_{in, (i-1)}$. Here, it is assumed that the output (fluorescence) intensity captured by the imaging system is, $I_{cam, i}$, linearly proportional to the input light intensity $I_{in, (i-1)}$ and non-linearly related to the concentration C_i through $f(C_i)$. From this we have,

$$I_{cam, i} = f(C_i) I_{in, (i-1)} + \beta_i \quad (\text{A.4})$$

Equation (A.4) can be rewritten using a finite approximation method. First write Equation (A.1) as:

$$I_{in, i} - I_{in, (i-1)} = -\epsilon C(i) I_{in, (i-1)} \Delta y \quad (\text{A.5})$$

Equation (A.5) can be expressed in an explicit form:
for pixel #1:

$$I_{in, 1} = I_{in, 0} (1 - \epsilon C_0 \Delta y) \quad (\text{A.6})$$

then for pixel #2:

$$I_{in, 2} = I_{in, 1} (1 - \epsilon C_1 \Delta y) \quad (\text{A.7})$$

and for pixel #3:

$$I_{in, 3} = I_{in, 2} (1 - \epsilon C_2 \Delta y) \quad (\text{A.8})$$

so,

$$I_{in, 3} = I_{in, 0} (1 - \epsilon C_0 \Delta y) (1 - \epsilon C_1 \Delta y) (1 - \epsilon C_2 \Delta y) \quad (\text{A.9})$$

which leads the general form:

$$I_{in, i} = I_{in, 0} \prod_{j=0}^{i-1} (1 - \epsilon C_j \Delta y) \quad (\text{A.10})$$

From experiment it was found that the camera responded to the input light intensity in a non-linear fashion as it is shown in Figure 2.19, so a general function was proposed to deal with this camera intensity non-linear response,

$$I_{cam} = (I_{in})^\alpha \quad (\text{A.11})$$

where,

$$\alpha = (1.0 - \frac{I_{cam}}{255.0})$$

Therefore, combining Equations (A.4), (A.10) and (A.11),

$$I_{cam,i} = f(C_i) I_{in,0} \prod_{j=0}^{i-1} (1 - \epsilon \alpha C_j \Delta y) + \beta_i \quad (\text{A.12})$$

From this, the local fluorescent dye concentration at each pixel location can be calculated by the inverse function, g , of the calibration function $f(C_i)$:

$$C_i = g(I_{cam,i}) \quad (\text{A.13})$$

where the product term in (A.11) accounts for absorption of the excitation beam over its path. Both $I_{cam,i}$, β_i and $f(C_i)$ have the units of digital counts, while ϵ has the unit of $(\text{mm}\cdot\text{mol}/\text{litre})^{-1}$. The parameters $I_{in,0}$, $f(C_i)$ and ϵ are determined experimentally and will be explained in the next section. From the experiment it was found that β_i 's were spatially random distributed constants.

Except at fairly low dye concentration, this attenuation was significant. For example, for a 500:1 dilution of source concentration ($C_s = 100 \times 10^{-6}$ mol/litre) which is $C = 2 \times 10^{-7}$ mol/litre, $\Delta y \approx 0.8$ mm and $\epsilon = 1.20 \times 10^3$ $(\text{cm}\cdot\text{mol}/\text{litre})^{-1}$ and the cross-stream width of a plume typically occupied about 300 pixels on the video image. From Equation (A.10) the

excitation beam attenuation along its path, assuming the laser power output is a constant, is:

$$\begin{aligned}
 I_{in,300} &= I_{in,0} \prod_{j=0}^{299} [1 - 1.2 \times 10^2 (2.0 \times 10^{-7}) \times 0.8] \\
 &= I_{in,0} (1 - 1.92 \times 10^{-5})^{299} \\
 &\approx I_{in,0} [1 - (299)(1.92 \times 10^{-4})] \\
 &= 0.9943 I_{in,0}
 \end{aligned}$$

which is negligible. But if there is only a 20:1 dilution of source concentration, then $C = 5 \times 10^{-6}$ mol/litre, so the attenuation over 300 pixels becomes $I_{in,300} \approx 0.8565 I_{in,0}$ that is a significant change. Therefore, the beam attenuation along its path is negligible only when the concentration of the fluorescent dye in the water is sufficiently low.

II. Response of the Imaging Optics and Determination of $f(C_i)$, ϵ and β_i

In order to use Equations (A.11) and (A.12) to correct for the attenuation of the laser beam, bottles of well mixed dye solutions with varying known concentrations C were used to determine the response of the image system. Each rectangular plastic bottle containing a known dye concentration, was placed in the test section at the measurement location and set up so that the sides of the bottle were normal to the laser beam in order to minimize the light reflection losses. When collecting data to determine the quantities of β_i , $f(C_i)$ and ϵ , a 60 second average was used.

Tests using sheets of plastic cut from the sides and top of the bottles showed that surface reflections of the laser beam from sides of these bottles, and the fluorescent light from the top produced negligible errors. The laser beam was then passed through the bottles and the fluorescent light intensities were captured by a video camera system, saved and analysed. To prevent saturation of the photodiode array inside the video camera and

extend the range of dye concentrations that can be measured, different camera apertures ($f_{\text{stop}} = 1.4$ and 5.6) were used.

Calibration bottles were prepared by successively diluting the mixture used in the previous bottle by a factor of two. The initial (highest concentration) solution was made by weighing fluorescein dye powder which has a molecular weight of 376.28 g/mole and dissolving it into distilled water. Two sets of dye concentration bottles, the first set consisting of 12 bottles from 100.0 mol/litre to 0.05 mol/litre , and the second set consisting of 10 bottles from 70.0 mol/litre to 0.14 mol/litre , were made up and used to find out how the system responded in different camera modes. Dye concentrations ranging from $10.0 \times 10^{-6} \text{ mol/litre}$ to $0.05 \times 10^{-6} \text{ mol/litre}$ were used when the camera aperture was set at $f1.4$. When the camera aperture was at $f5.6$, bottles with dye concentration ranging from $70 \times 10^{-6} \text{ mol/litre}$ to $0.1 \times 10^{-6} \text{ mol/litre}$ were tested.

The measured intensity was extrapolated to the edge of the bottle to minimize the light reflection and attenuation error by fitting the data through a modified Lambert Beer's law with an empirical exponent to account for the camera output non-linearity with varying input intensity. It is,

$$I_{cam} = I_{cam, cen} \left(\exp [\epsilon C (y - y_{cen})] \right)^\alpha \quad (\text{A.14})$$

where,

$I_{cam, cen}$ is the light intensity at the centre, y_{cen} of a calibration bottle;

$\alpha = (1.0 - I_{cam, cen}/255.0)$ is the empirical camera non-linearity factor.

Equation (A.14) was also used to determine the intensity of the dye solution at the edge of the calibration bottle, where light attenuation was neglected. This formula can be expressed in a form more useful for finite difference, it is

$$I_{cam} = I_{cam,0} \exp(\epsilon \alpha C (y - y_0)) \quad (\text{A.15})$$

See Figure 2.20 for details how to define $I_{cam,0}$. Figures A-1 to A-6 show how the extrapolation was done for the bottles tested. Figure A-7 shows how the imaging system responded to different dye concentrations ($\mu\text{mol/litre}$) at different camera aperture settings. An exponential function was used to fit the data using either camera f_{stop} at 1.4 or 5.6. For $f_{\text{stop}} = 1.4$, the function has the form:

$$C = 0.93963 \exp(0.0064950 I) - 0.89384 \quad (\text{A.16})$$

While for $f_{\text{stop}} = 5.6$:

$$C = 44.38149 \exp(0.001625 I) - 43.86201 \quad (\text{A.17})$$

In Figure A-7, $I_{m,0}$ was defined for convenience to be unity. For details on how to deal with the day-to-day variation of laser output see section 2.5.3 of Chapter 2.

Constant β_i , as shown in the Figure A-8, was determined by measuring the digital outputs along the laser beam path while the laser beam passed through clear water at the test section. It was found that β_i acted as a spatially distributed random variable with mostly at zero counts and some 1 counts. β_i 's were used as a pixel-by-pixel digital offset when correcting the laser beam attenuation.

The laser beam extinction coefficient ϵ was determined by fitting the intensity data using exponential fit, as shown in Figures A-1 to A-6 for every known concentration calibration bottle tested, using Equation (A.13). It was found that ϵ was a constant for camera f_{stop} at both 1.4 and 5.6:

$$\epsilon = 120.0 \text{ (mm}\cdot\text{mollitre)}^{-1} \quad (\text{A.18})$$

III. Numerical Correction for Dye Attenuation

A computer program was written to correct the laser light attenuation caused by the high

concentration plume clouds. The correction subroutine of the program is based on Equation (A.12) and the aim is to find the $C_{cor, i}$. After rearranging Equation (A.12),

$$f(C_{cor, i}) = \frac{I_{cam, i} - \beta_i}{I_{in, 0} \prod_{j=0}^{i-1} (1 - \epsilon \alpha C_j \Delta y)} \quad (A.19)$$

where $C_{cor, i}$ is calculated from the formulae obtained from fitting the calibration results presented in the Figure A-7(a) or B-7(b) depending on the camera f_{stop} . When the camera aperture was set at 1.4, the fitting equation (A.16) was used and equation (A.17) was used when the camera aperture was set at 5.6. The attenuation was not taken into account until the occurrence of $I_{cam, i} > \beta_i$.

$C_{cor, i}$ can be calculated pixel by pixel after the attenuation correction for each run of experiment using adjusted Equation (A.16) or (A.17) depending on the camera aperture setting. The correction scheme was tested against the known dye concentration by using the dye bottles and performed well, as shown in Figure A-9.

IV. Time-Dependent Dye Bleaching

Another factor that can have effects on the dye fluorescent intensity is bleaching. When fluorescein dye is continuously exposed to laser excitation radiation it undergoes a photo bleaching reaction to a non-fluorescing state. Even though the bleaching effects did not cause any problem in the present studies, it is worth mentioning.

When fluorescent dye is continuously exposed to excitation radiation, it undergoes a photo bleaching reaction and reaches a non-fluorescing state. The fraction of photo bleached molecules per photon absorbed is defined as the bleaching quantum efficiency, F_Q , a very small number. It was determined by Ippen *et al* (1971) that $F_Q = 4 \times 10^{-6}$ for fluorescein dye exposed to light at 514.5nm wavelength. As suggested by Koochesfahani

(1984), the number of dye molecules available for fluorescence decreases exponentially with a time constant given by the following formula:

$$t_{absorb} = \frac{1}{F \Phi \sigma} \quad (\text{A.20})$$

where Φ is the photon flux, and σ is the molecular cross section of the dye in cm^2 . The molecular cross section is determined from the extinction coefficient ϵ , using $\sigma = 2,300\epsilon/N_{av}$ from Parder(1968), where N_{av} is Avogadro's number which is equal to 6.023×10^{23} molecules/mol. For the present experiment, Φ and σ can be found as the following.

$$\Phi = \frac{P}{E_{photon} A_l} \quad (\text{A.21})$$

where:

P = the power of the laser beam (w);

E_{photon} = energy per photon (J/photon)

= $h\nu$ (where h is the Plank constant and ν is the laser light frequency);

A_l = the cross-sectional area of the laser beam(mm^2);

with,

$P=75$ mW;

$E_{photon}=3.86356 \times 10^{-19}$ J/photon;

$A_l=0.78540$ mm^2

then, $\Phi=2.47163 \times 10^{17}$ photons/ mm^2/s , and $\sigma=4.58243 \times 10^{-16}$ $\text{mm}^2/\text{photon}$ and this leads to $t_{absorb} = 36.8$ minutes. An experiment was done to test Koochesfahani's (1984) dye exponential decay hypothesis. It was found that the measured time constant was about 42 minutes (as shown in the Figure A-10).

The test results indicate that the photo-bleaching of the dye solution exposed to laser light

could be controlled by the initial number of available fluorescing dye molecules, the sensitivity of the image system if the laser output power is kept as a constant. Both the dye photo-bleaching test result and theoretical prediction ensure that for the current study this photo-bleaching effects can be neglected because on average the time required for a fluid element to travel across the laser beam or the laser sheet is, from 0.01 to 0.3 second, as shown in Figure A-11, far less than the bleaching constant.

The longtime bleaching reduced the measured light intensity by about 10%, with the data fitted by,

$$I = 216.6 \times (1 - 0.123 \exp(-\frac{t}{\tau})) \quad (\text{A.22})$$

From this it was concluded that photo-bleaching effects do not cause any problems when collecting the fluorescent intensity data since the fluid is moving all the time. However, while doing calibrations using the known concentration bottles, the laser light was blocked before taking any intensity data as a precaution. It was found that for very long time exposures to the laser light the intensity readings for the same known dye concentration solution could drop to as low as 90% of their original values (shown as in the Figure A-10). But over the few minutes during which a calibration bottle was exposed, bleaching errors were negligible.

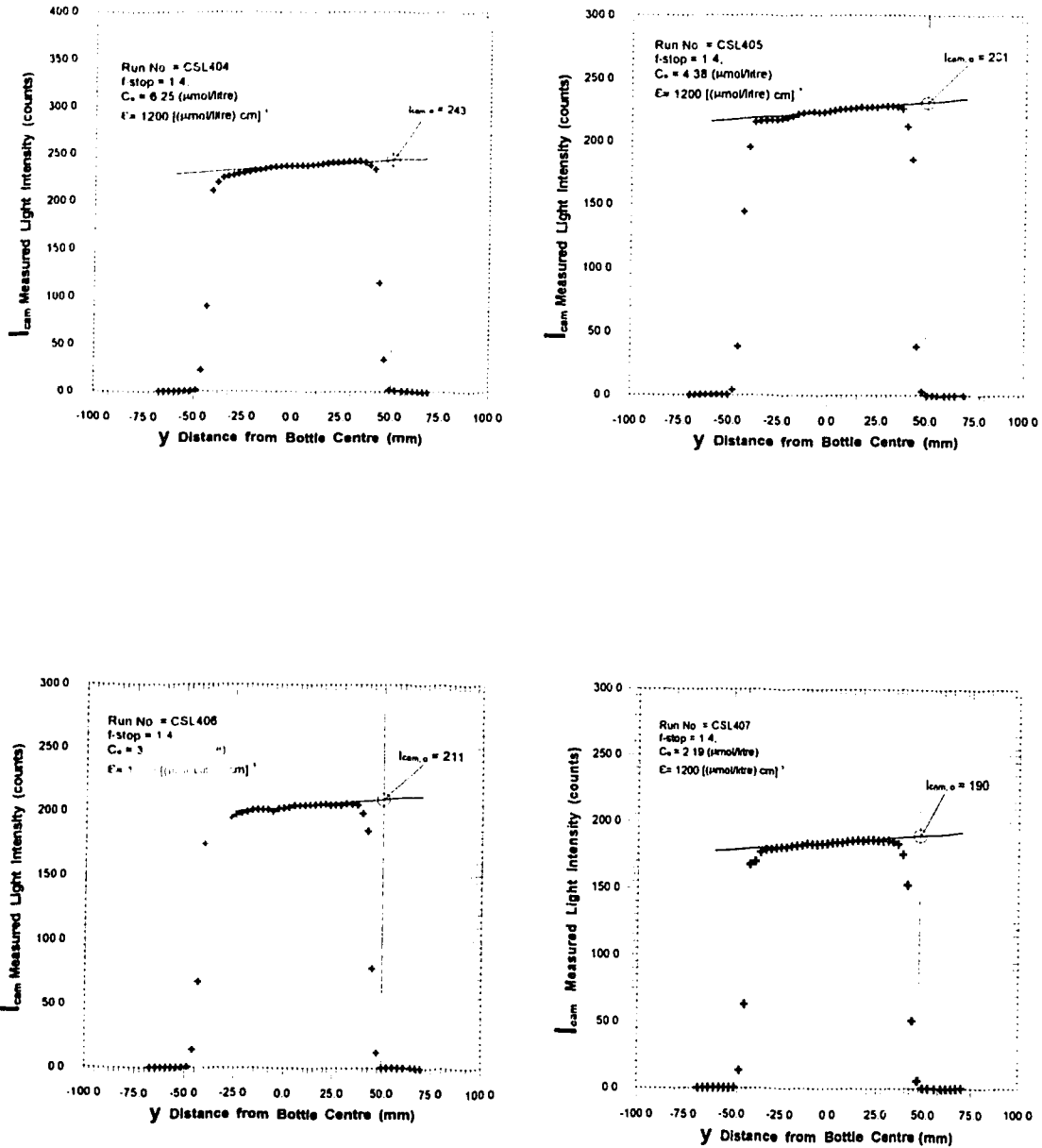


Figure A-1 Determination of extinction coefficient ϵ with varying concentration when $f_{stop} = 1.4$, shutter speed = 1/250 sec and tested concentration at $C = 6.25, 4.38, 3.13$ and $2.19 \mu\text{mol/litre}$.

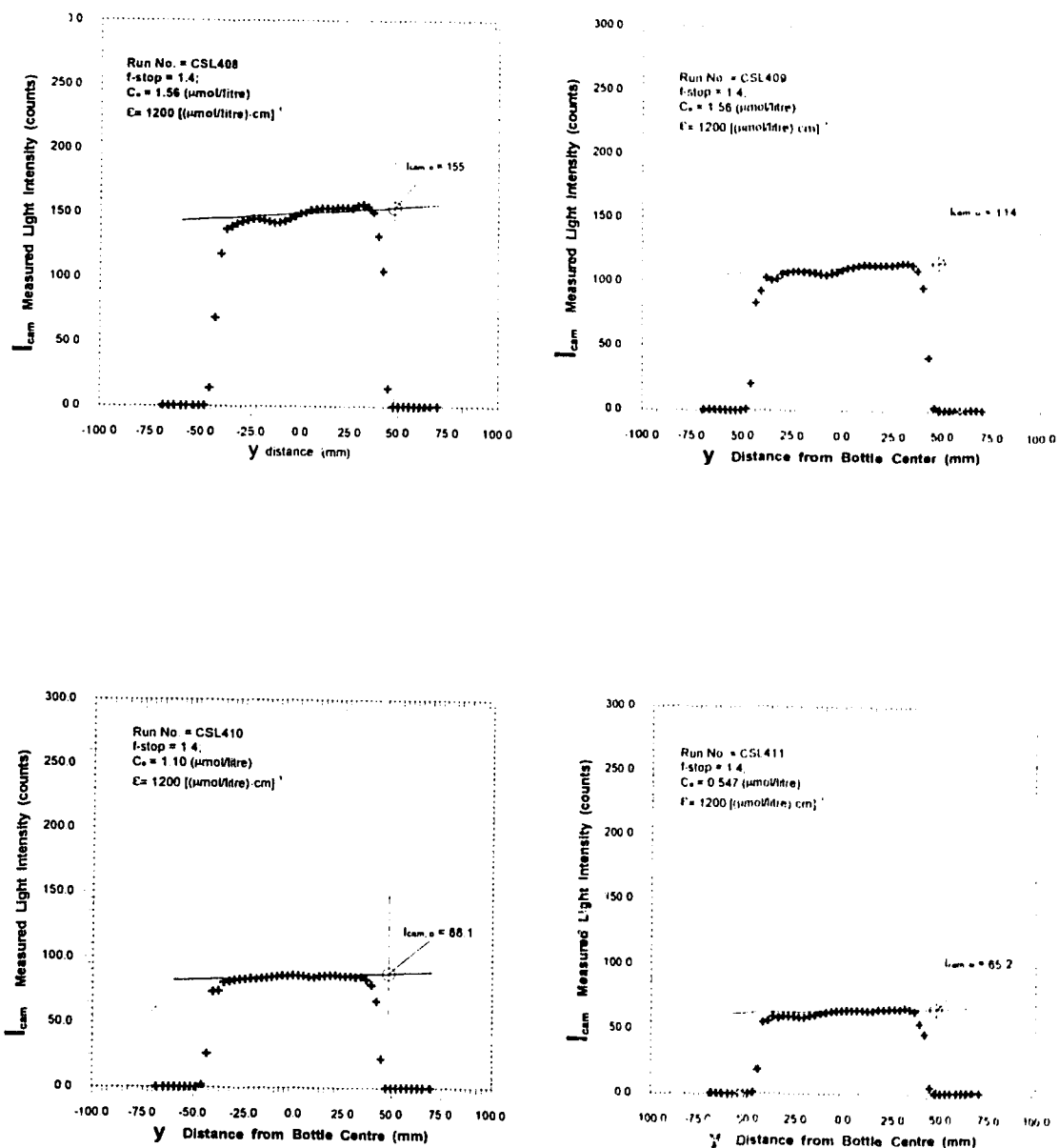


Figure A-2 Determination of extinction coefficient ϵ with varying concentration when $f_{\text{stop}} = 1.4$, shutter speed = $1/250$ sec and tested concentration at $C = 1.56, 1.09, 0.78$ and $0.55 \mu\text{mol/litre}$.

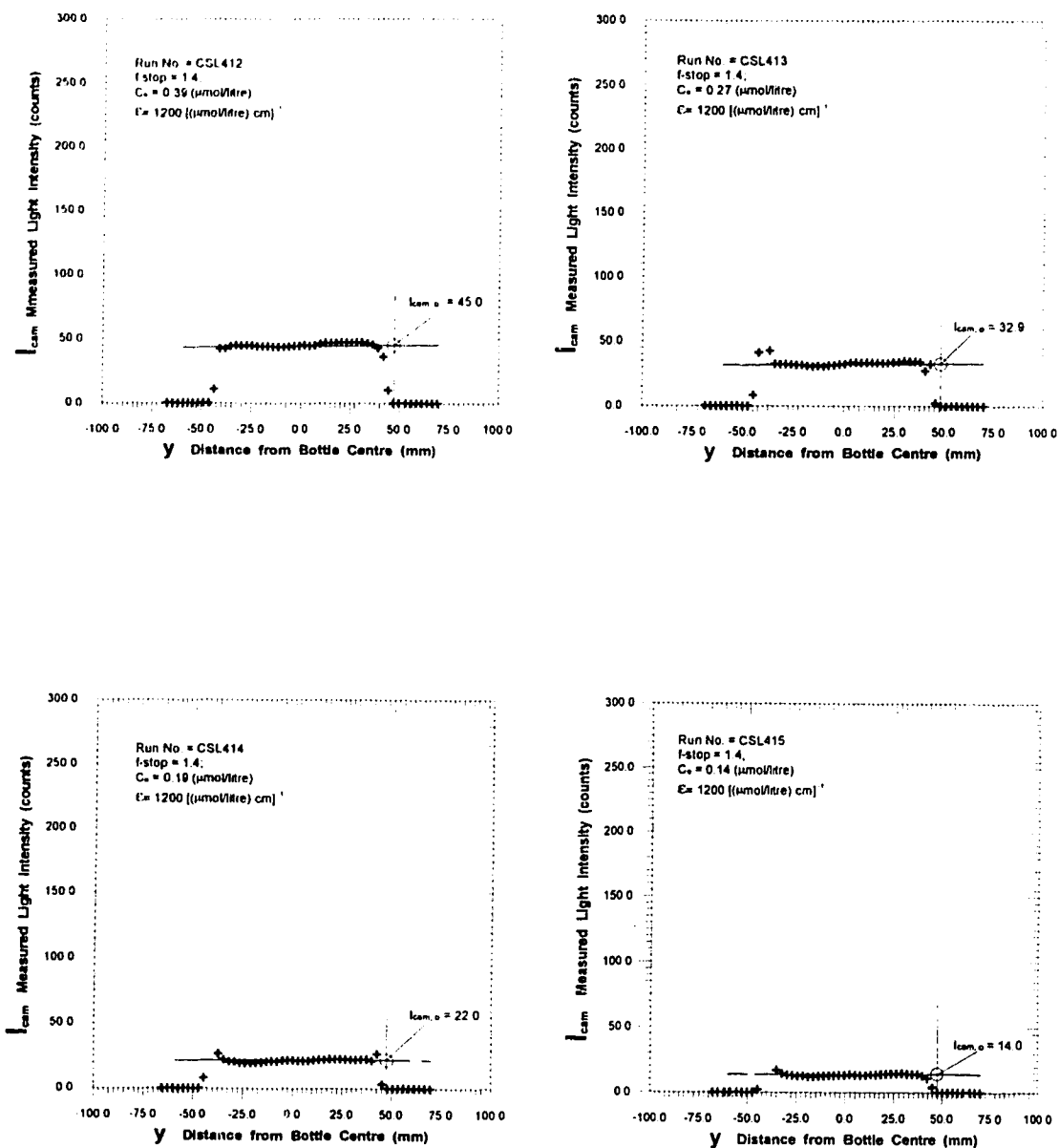


Figure A-3 Determination of extinction coefficient ϵ with varying concentration when $f_{\text{stop}} = 1.4$, shutter speed = 1/250 sec and tested concentration at $C = 0.39, 0.27, 0.19$ and $0.14 \mu\text{mol/litre}$.

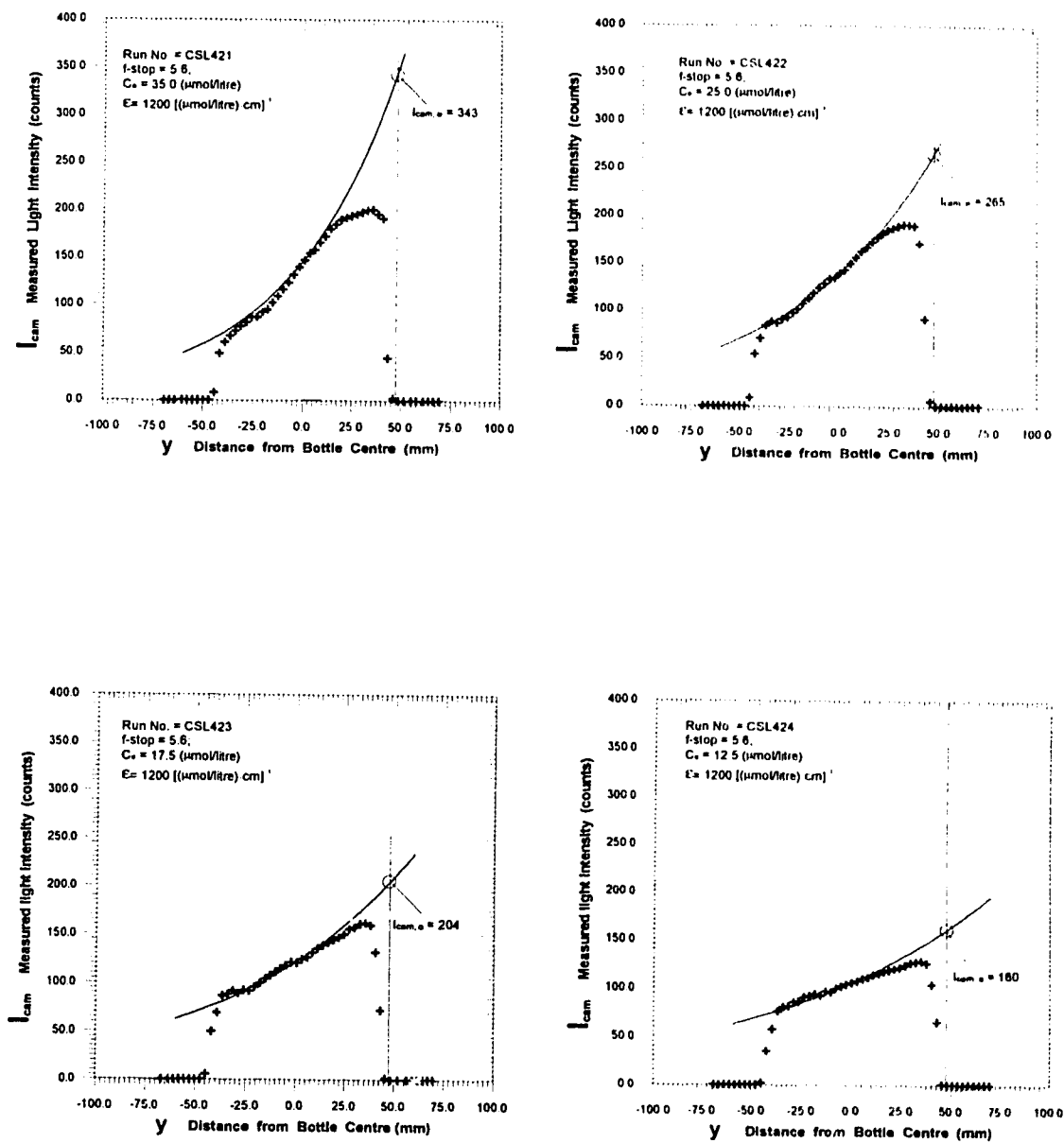


Figure A-4 Determination of extinction coefficient ϵ with varying concentration when $f_{\text{stop}} = 5.6$, shutter speed = $1/250$ sec and tested concentration at $C = 35.0, 25.0, 17.5$ and $12.5 \mu\text{mol/litre}$.

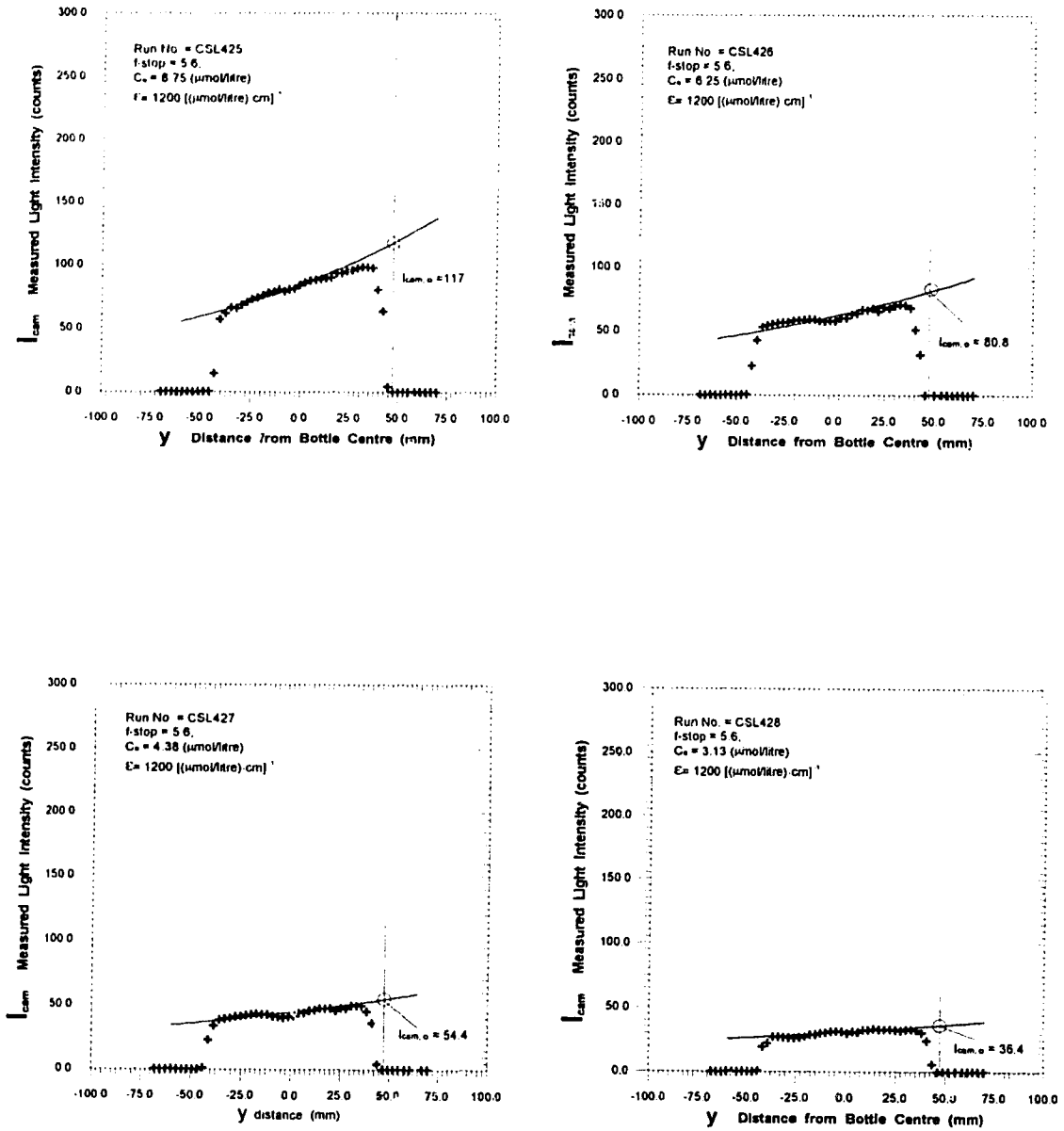


Figure A-5 Determination of extinction coefficient ϵ with varying concentration when $f_{stop} = 5.6$, shutter speed = 1/250 sec and tested concentration at $C = 8.75, 6.25, 4.38$ and $3.13 \mu\text{mol/litre}$.

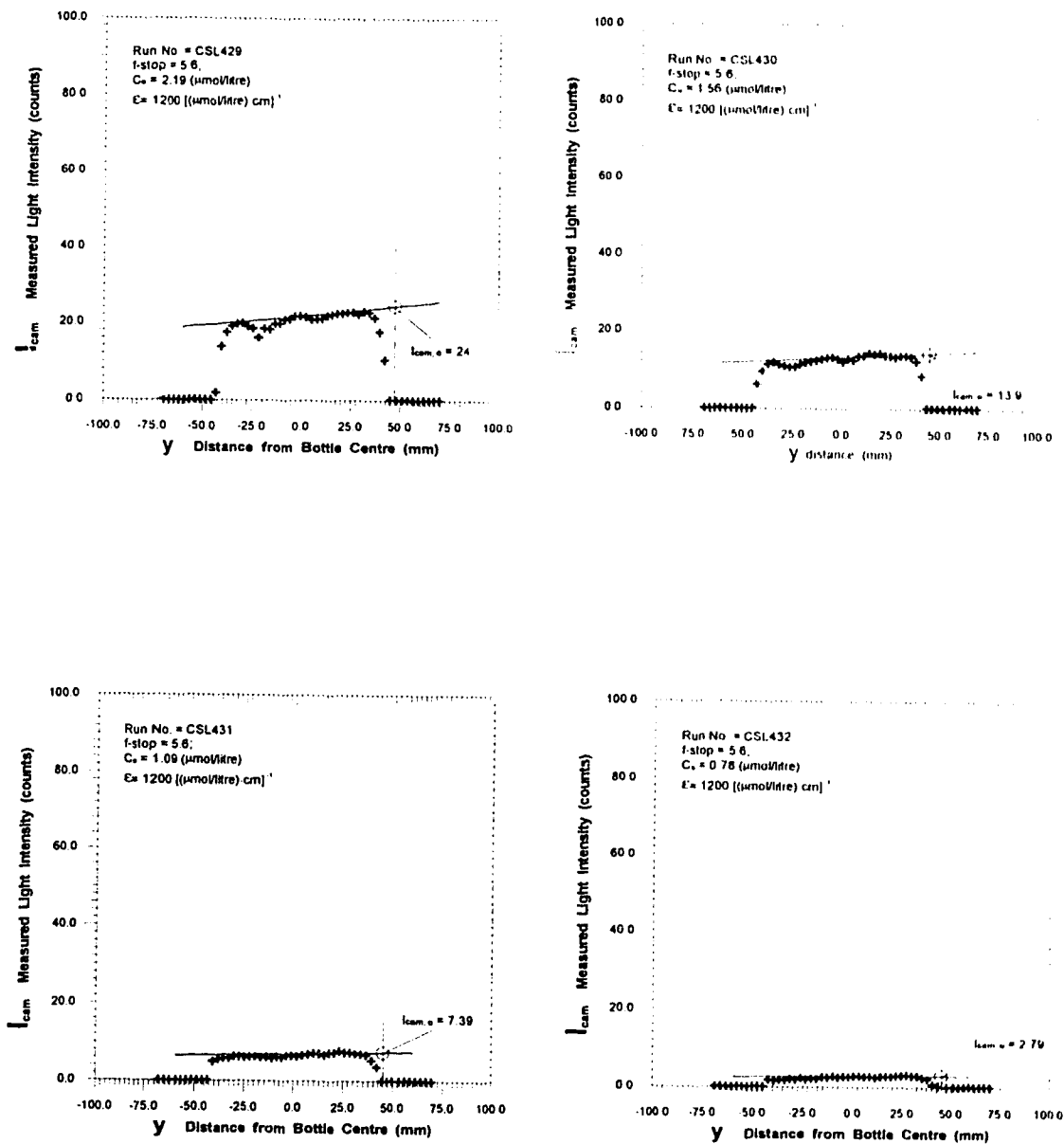


Figure A-6 Determination of extinction coefficient ϵ with varying concentration when $f_{stop} = 5.6$, shutter speed = 1/250 sec and tested concentration at $C = 2.19, 1.56, 1.09$ and $0.78 \mu\text{mol/litre}$.

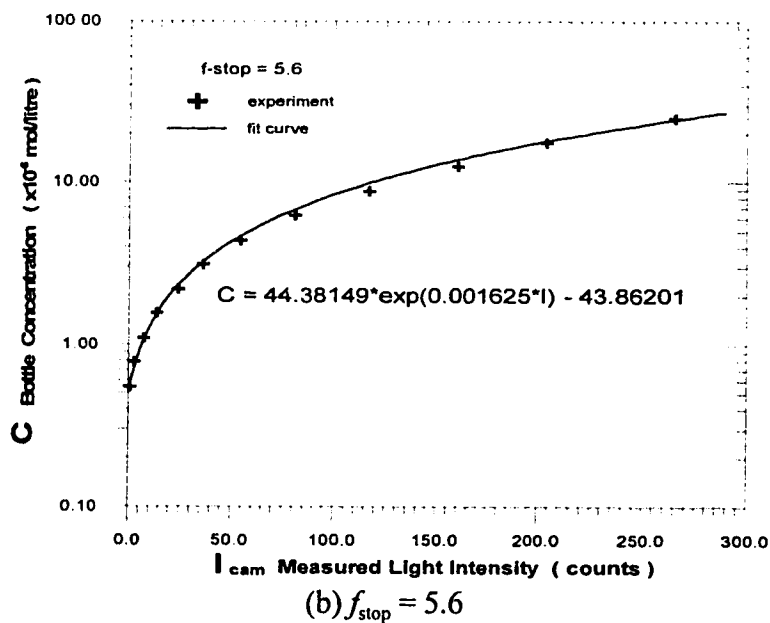
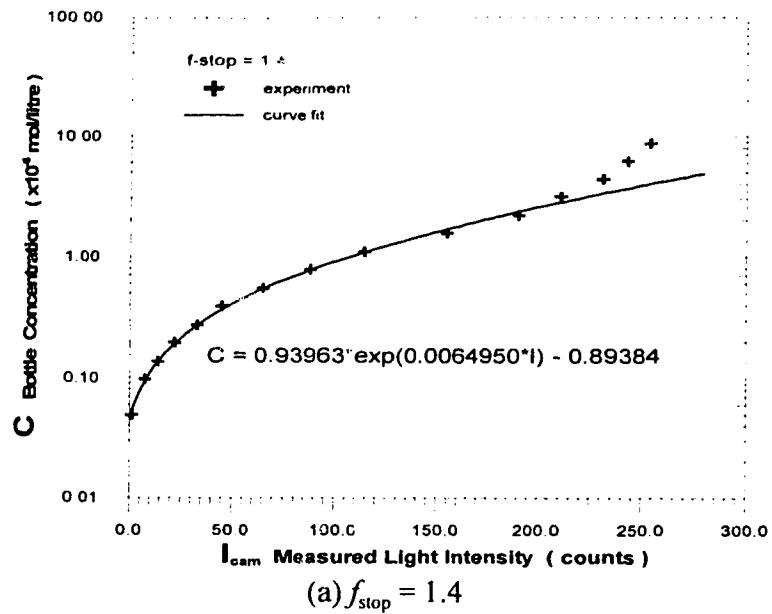


Figure A-7 Image system response to dye solutions at camera f_{stop} set at 1.4 or 5.6 when other camera settings were: shutter speed = 1/250 sec, camera gain = 6, camera white balance = 3200 and filter used = Kodak Wratten No.21 gelatin filter.

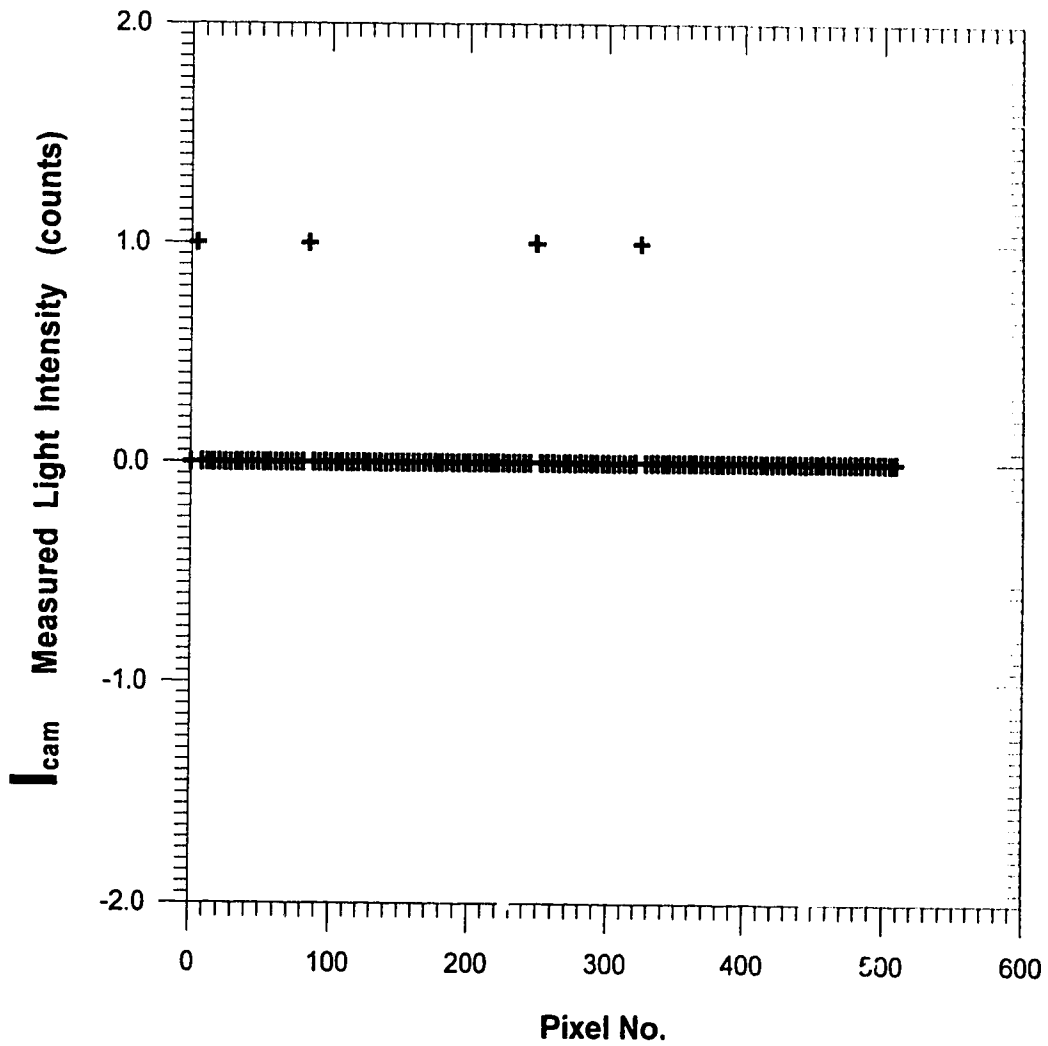


Figure A-8 Pixel-by-pixel dark response of the image system along a single line (100 frame average)

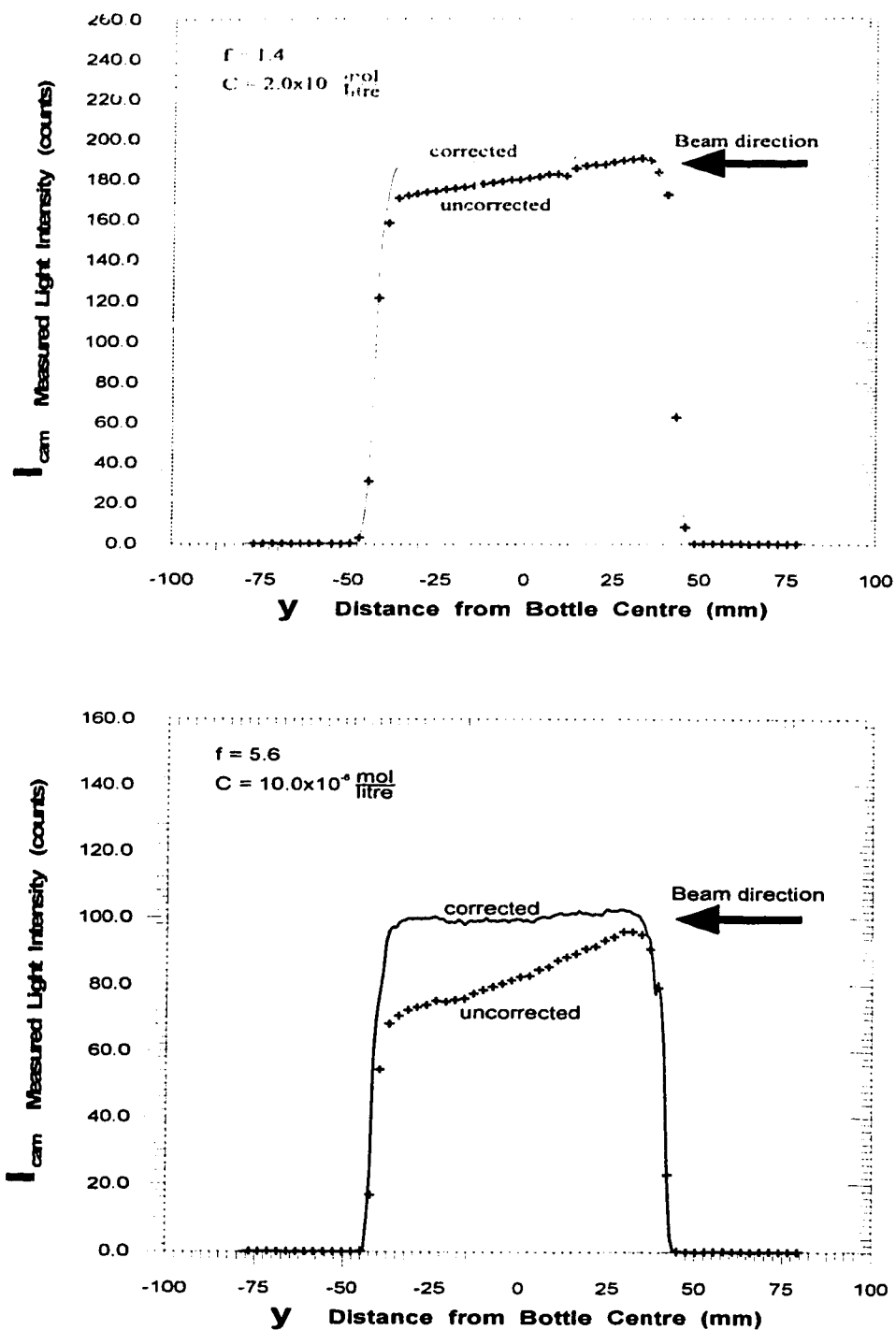


Figure A-9 Illustration of measured light intensity before and after attenuation correction

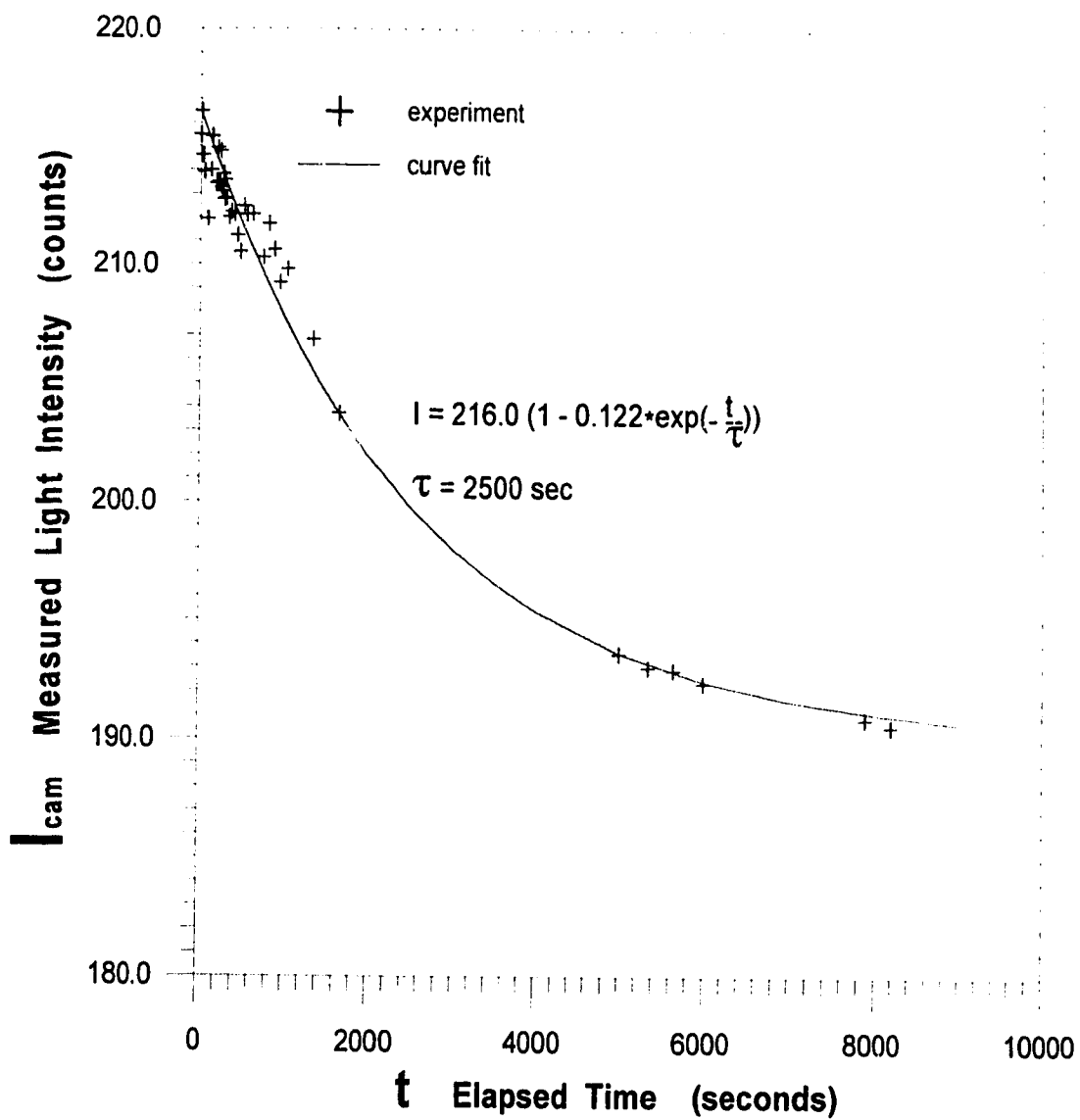
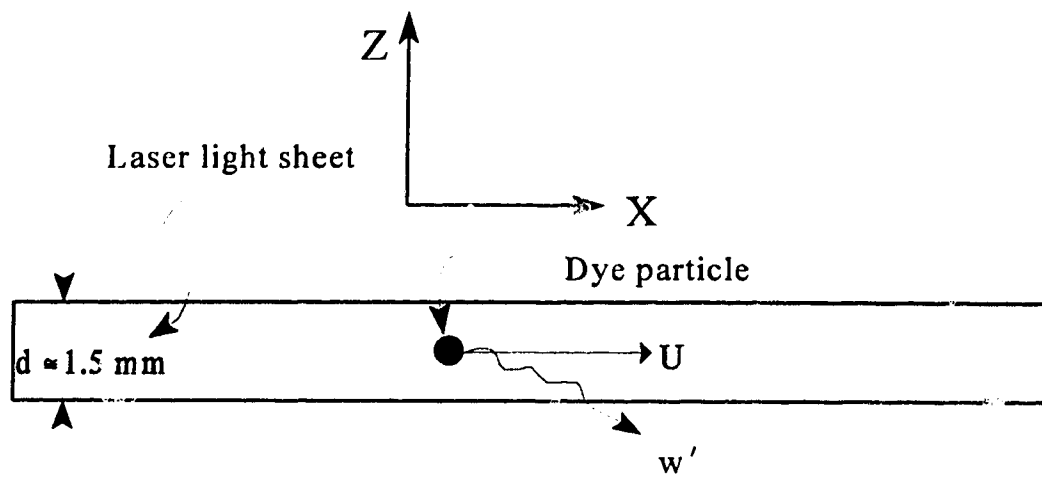


Figure A-10 Laser light bleaching test on fluorescent dye solution with Concentration of $5 \mu\text{mol/litre}$.



$U \sim 100 \text{ mm/sec}$, and $w' \sim 0.05U$, then

$$\Gamma_{\text{resident}} \propto d/w' \sim 1.5/5 \sim 0.3 \text{ sec}$$

Figure A-11 Illustration of dye particle path across the laser sheet

Appendix B

Image Processing for Sheet Lighting

Flow patterns around the model buildings were visualized using the Planar Laser Induced Fluorescence (PLIF) system. In the present experiment, disodium fluorescein dye was released into the water channel from a ground level source and illuminated by a laser sheet. A video image was then taken, so the dye concentration could be determined from its fluorescent intensity.

I. Generating a Pair of Laser Light Sheets

The PLIF system used was similar to the one developed by Campbell (1991) and used by Johnston (1993). A Coherent Innova 70, 4W argon-ion continuous wave laser was operated in multi wavelength mode, producing light at 488 nm and 514.5 nm (blue-green). To increase the laser operational life, the laser was run at 3W instead of at its maximum output 4W. The single beam from the laser was split into two beams using a 50/50 dielectric mirror beam splitter shown in Figure B-1 to generate the two opposite laser sheets.

The two split beams were then passed through 20× microscope objectives to reduce their diameters smaller than the 50 μm of the core diameter of the fibre optic cable to improve the coupling efficiency. Fibre optic cable was used to transfer the laser light emerging from the 20× microscope objective to the receiving optics to produce a laser light sheet, as shown in Figure B-2.

The light emerging from the fibre optic cables was refocused into a narrow beam using

a 20× microscope objective, followed by 100 mm and 300 mm focal length spherical lenses to refocus the beam at a point about 2000 mm away, in the centre of the water channel. The 20× microscope objective was positioned directly in front of the optic fibre cable such that the maximum laser power was transferred. The 100 mm and 300 mm focal length spherical lenses were placed 5 mm and 400 mm away from the microscope objective. Following the 300 mm lens each beam passed through a 10 mm focal length cylindrical lens. The 10 mm focal length cylindrical lens was placed 415 mm in front of the 20× microscope objective. The laser light sheet had an approximate 1.5 mm minimum thickness at 2000 mm from the 10 mm focal length cylindrical lens increasing to about 3 mm at ±500 mm from this minimum thickness location.

The Gaussian light intensity profile makes a laser sheet brighter at the centre and dimmer at the edges. Therefore, to produce a more uniform light sheet at the test section and avoid problems of light sheet attenuation the test section was lit from both sides of the water channel. As shown in Figure B-2, the optics assemblies used to refocus and expand the laser beams into sheets were mounted on two optic stands placed at opposite sides of the channel. The overall power transmission efficiency from the laser beam splitter to the laser sheet was approximately 60%.

II. Viewing Plume Cross Sections

Two different views of the plume around a model building are shown in Figure 2.25 as sections x - y and y - z . With the laser sheets orientated horizontally, section x - y was lit. To view the horizontal section x - y , the video camera was horizontally mounted to look at the reflection mirror. The reflection mirror, which is 400 mm wide × 1000 mm long, was mounted to a frame angled at 45° towards the camera, shown in Figure 2.25.

The other plume viewing section y - z is also shown in Figure 2.25. To view this vertical cross stream section of the plume, a periscope was positioned downstream of the model

building. The lower portion of the periscope is a 90° PVC pipe elbow with 12" nominal diameter. A mirror was mounted inside at 45° and the opening facing upstream was covered by a piece of clear glass and silicone sealant. The upper portion was a piece of straight tubing with mounting brackets and the camera holding frame. The periscope then was fastened to a frame secured to the water channel railing. The camera was clamped on the camera holding bracket at the top of the periscope to capture the plume cross section images looking upstream.

III. Correcting the Raw Images

The full-field images were stored directly on the computer hard disk. Each pixel in an image was an 8 bit integer representing the fluorescence intensity level for that pixel. The intensity information then had to be converted into concentration to determine the concentration distribution across the plume. To reduce the shadows caused by the edges of the model building and the camera amplifier noise, the raw images were corrected using a square 9×9 pixel average (lowpass) filter to spatially filter the image.

a). Intensity and Concentration Conversion

To convert the fluorescent intensities to their corresponding concentrations for each pixel, the intensity response of the imaging system needed to be known. As the Figure B-3 shows, the problem is that $I_{in,ref}$ for the group of pixels where the bottle calibration is carried out is unknown. Some assumptions were made to make analysis possible:

- i. For dual light sheets the laser light attenuation can be neglected, so $I_{m,j}$ at j^{th} pixel is independent of concentration along laser light path;
- ii. $I_{m,j}$ varies only due to nonuniform intensity in space, but is steady in time;
- iii. I_j is linearly proportional to $I_{m,j}$ for a given C_j .

A square of 10×10 pixels located at the centre of the bottle was set as the reference location, and based on assumption (iii) above, a set of known concentration bottles

ranging from 0.25×10^{-6} to 100×10^{-6} mol/litre were used to determine the output response, $I_{j,out}$, of the image system at different dye concentrations while keeping the laser sheet intensity constant. The empirical concentration calculation function $g(c_j)$ for pixel j is defined by,

$$I_{j,out} = I_{in,j} g(c_j) \quad (\text{B.1})$$

Then, invert this function to produce the usual calibration curve,

$$C_j = f\left(\frac{I_j}{I_{in,j}}\right) \quad (\text{B.2})$$

when this is applied to an average over the 10×10 square of reference pixels “ref”,

$$C_{ref} = f\left(\frac{I_{ref}}{I_{in,ref}}\right) \quad (\text{B.3})$$

In general the value of $I_{in,ref}$ is unknown. Here, it was set arbitrarily to unity in all calibration curve fits as shown in the Figure B-4. The curve fit function then was used to convert the known fluorescent intensity into its corresponding concentration or vice versa. Data with measured intensity values close to the camera saturation point of 255 counts were discarded because the attenuation effects induced by the high calibration concentration lead to problems, and the intensity data were clipped.

b). Intensity Correction

Since the light sheet intensity varies in space, it is necessary to correct this intensity variation for each pixel. To do so, the input light intensity must be known, $I_{in,j}$. The first step is to use the inverse function of Equation (B.1),

$$I_{ref} = I_{in,ref} g(c_{ref}) \quad (\text{B.4})$$

The second step is to fill the water channel with dilute dye concentration C_{sheet} , measure the intensity $I_{j,sheet}$ for each pixel in the image and also the average sheet intensity at the

same location where the bottle calibrations used. The $I_{in,j}$ can be found from:

$$I_{in,j} = \frac{I_{j,sheet}}{g(C_{sheet})} \quad (B.5)$$

substituting Equation (B.4) into (B.5),

$$I_{in,j} = I_{in,ref} \frac{I_{j,sheet}}{I_{ref,sheet}} \quad (B.6)$$

However, later in the actual experiment it was found that the Equation (B.6) overcorrected the pixel intensity at the centre of the sheet and under corrected the pixel intensity at the edges of the sheet. To solve this problem, an empirical constant A_1 was added to the Equation (B.6). A_1 was determined by comparing concentration images for known concentration calibration bottles measured at different locations using the same light sheet. In the present study, the value for this empirical constant, A_1 , is 0.3. So, Equation (B.6) is modified as,

$$I_{in,j} = I_{in,ref} \frac{I_{j,sheet} + A_1}{I_{ref,sheet} + A_1} \quad (B.7)$$

Then, using Equation (B.2) and (B.6), the concentration at each pixel of the image of the plume will be:

$$C_j = f \left(\frac{I_j}{I_{in,ref} \left(\frac{I_{j,sheet} + A_1}{I_{ref,sheet} + A_1} \right)} \right) \quad (B.8)$$

The value $I_{in,ref}$ is set arbitrarily to $I_{in,ref} = 1.00$, so,

$$C_j = f \left(\frac{I_j}{\left(\frac{I_{j, sheet} + A_1}{I_{ref, sheet} + A_1} \right)} \right) \quad (B.9)$$

The corrected pixel intensity for an image will be:

$$I_{j, cor} = \frac{I_j}{\left(\frac{I_{j, sheet} + A_1}{I_{ref, sheet} + A_1} \right)} \quad (C.9)$$

This equation will be the backbone of the methods that correct the background, building shadows and other light sheet irregularities.

c). Background Level Correction

When the amount of fluorescent dye released into the water increased during the experiment, the background intensity increased. To deal with this problem, a 50 frame average intensity image at the beginning and the end of each data collection run was recorded separately. The background intensity was filtered using the 9×9 pixel spatial average filter first, and normalized by the corrected corresponding sheet image using the same size lowpass filter. Then the corrected background images were converted into concentration and subtracted from the corrected full-field concentration image pixel by pixel.

d). Corrections for Building Shadows and Light Sheet Irregularities

Because of the different refraction index between water and the plexiglass used to make the two model buildings, shadows were generated by the edges of buildings. A spatial average filter was used to smooth the building shadows. It was found that a 9×9 average (lowpass) filter was the best among other choices such median, edge enhancing and

blurring filters. Some samples are shown in the Figures B-5 and B-6. These pictures were taken with the camera looking down from above of the water channel. The maximum dilution from the source concentration to the outermost contour of these pictures is 2000:1. The source concentration used was 100×10^{-6} mol/litre, and the minimum concentration showed on these pictures is 0.05×10^{-6} mol/litre. Each contour layer from these pictures has a dilution factor of 1.50.

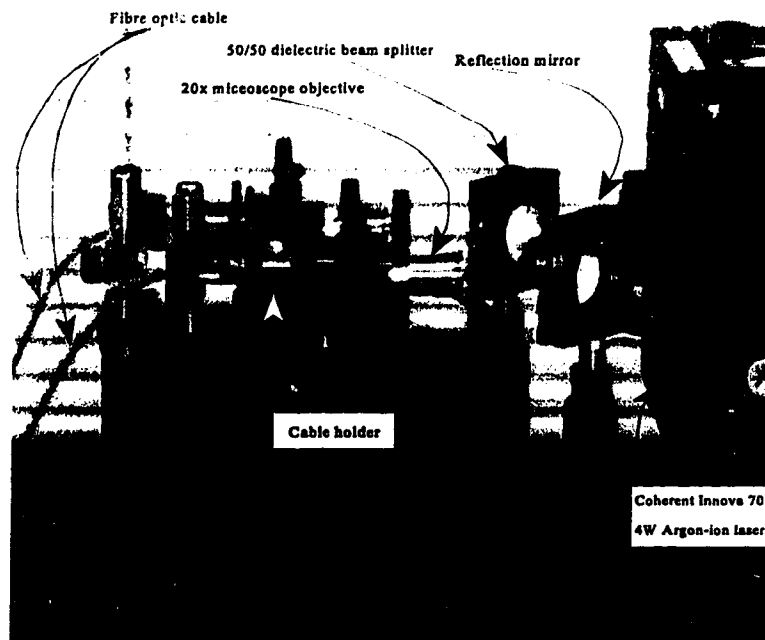


Figure B-1 Laser and splitting optics (used in PLIF)



Figure B-2 Laser beam expanding optics assemblies and sheet optics used to produce a light sheet

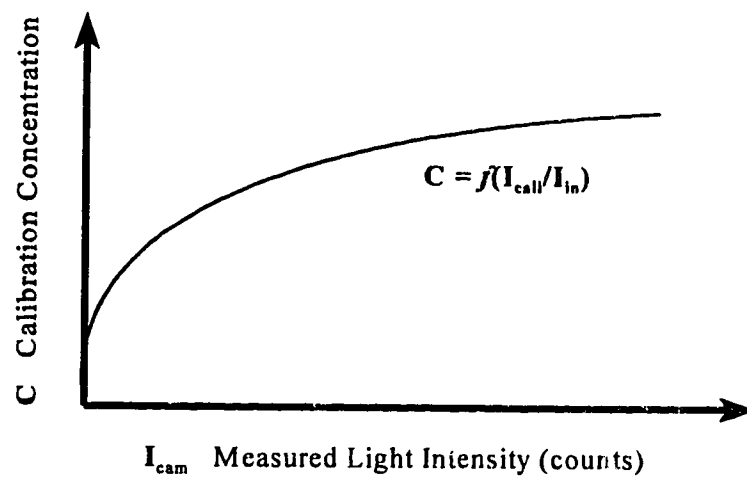
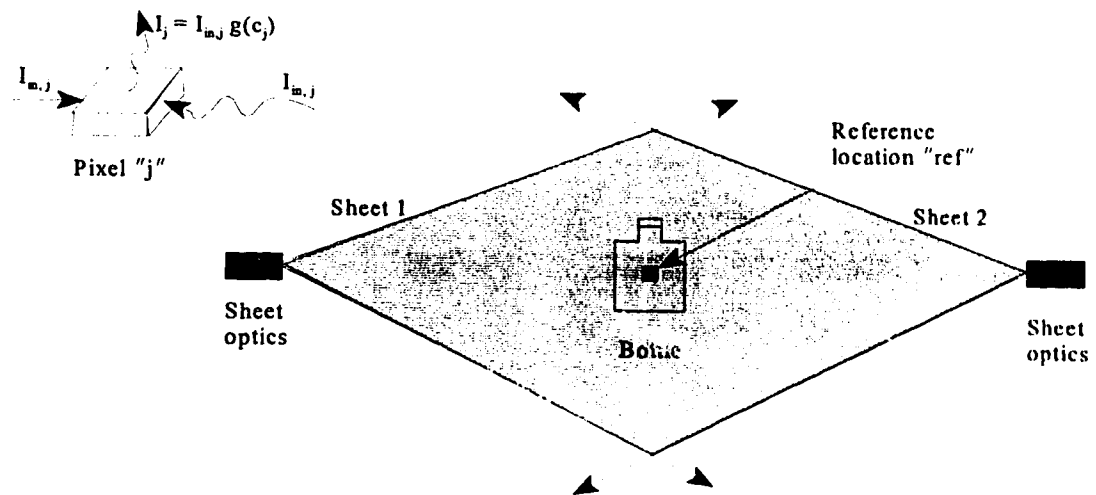


Figure B.3 Schematic diagram of dual laser sheet concentration calibration

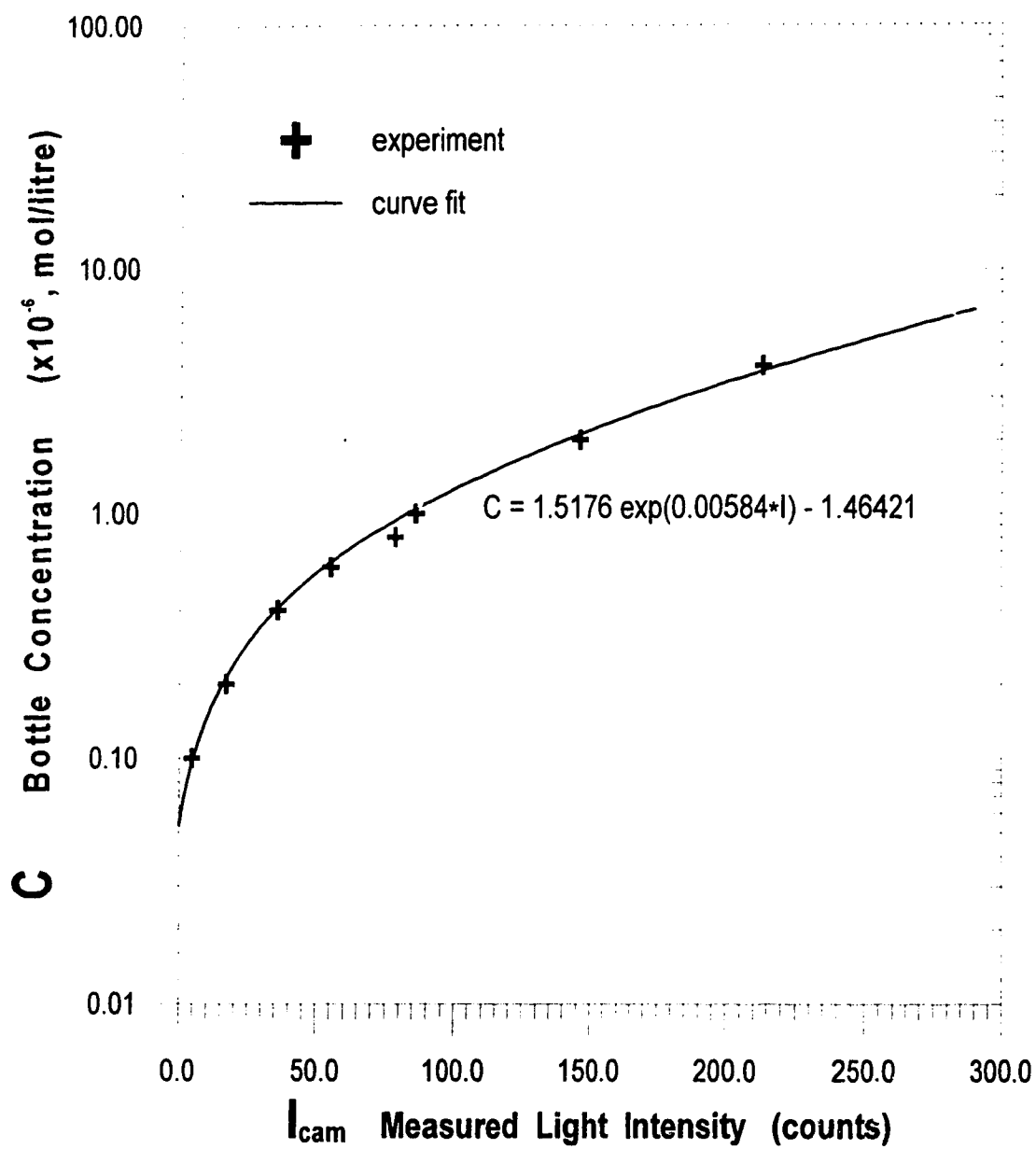
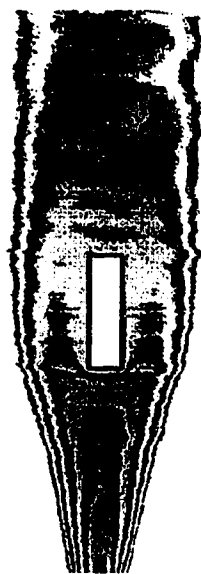
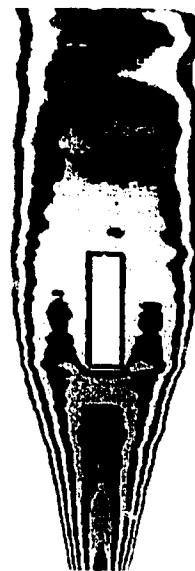


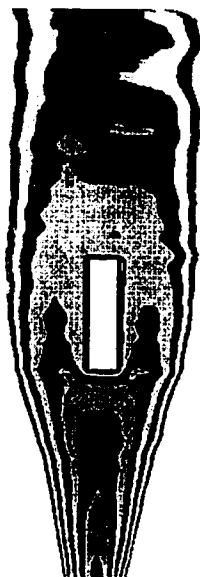
Figure B-4 Calibration curve for the dual laser light sheet with the camera settings as: $f_{\text{stop}}=2$, speed=1/60 s and laser power=3.0 W



(a) No filter



(b) 5×5 lowpass filter

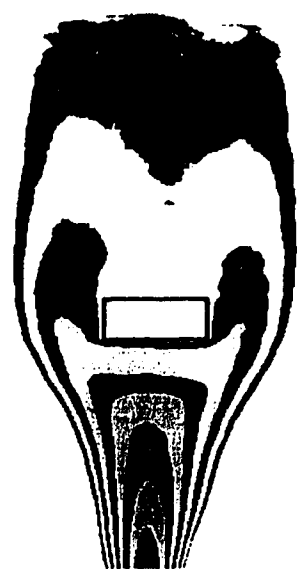


(c) 9×9 lowpass filter

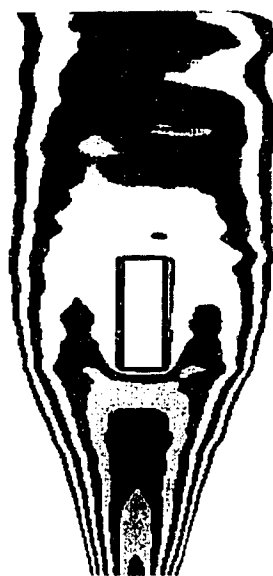


(d) 13×13 lowpass filter

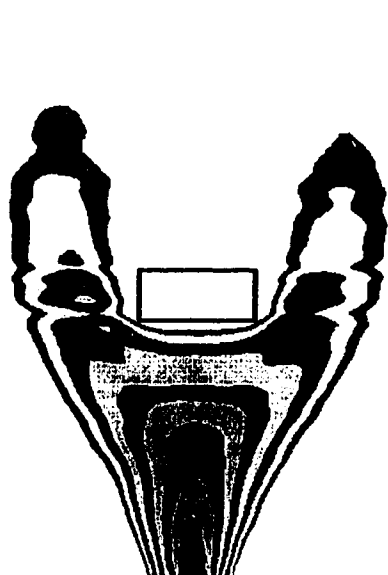
Figure B-5 Effect of using different size lowpass filter on a selected plume image



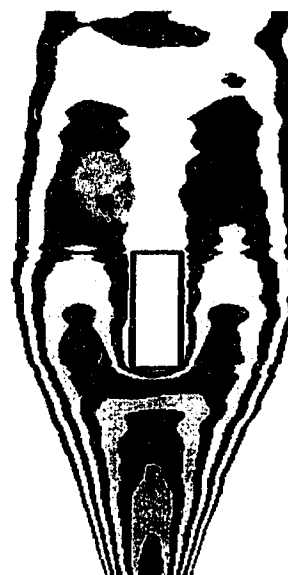
(a) Model building
A at 0°



(b) Model building
A at 90°



(c) Model building *B*
at 0°



(d) Model building *B*
at 90°

Figure B-6 Examples of selected images corrected by using 9×9 lowpass filter (Building location: $x = 270\text{mm}$ from the source. Building size: building *A*, 100mm wide × 50mm height × 40mm long; building *B*, 100mm wide × 100mm height × 40mm long)